Ryanodine Receptor 2 (RyR2) underlies maintenance and remodeling of dendritic spines

---

Dissertation

zur

Erlangung des Doktorgrades (Dr. rer. nat)

der

Mathematisch-Naturwissenschaftlichen Fakultät

der

Rheinischen Friedrich-Wilhelms-Universität Bonn

vorgelegt von

Fabio Bertan

aus Meran/o

Bonn, Oktober 2019

Angefertigt mit Genehmigung der Mathematisch-Naturwissenschaftlichen Fakultät der
Rheinischen Friedrich-Wilhelms-Universität Bonn

1. Gutachter: Prof. Dr. Pierluigi Nicotera
2. Gutachter: Prof. Dr. Michael Pankratz
Tag der Promotion: 29/01/2020
Erscheinungsjahr: 2020

1. Summary

The human brain comprises 10^{12} neurons that receive, integrate and transmit electrochemical signals. This complex network constantly re-adapts during an animal's lifetime. All sensed experiences refine neurons via activity-evoked processes that critically affect cognition and behavior. The most dynamic neuronal structure is the synapse, a microdomain that controls the transmission of electrochemical signals from cell to cell. Upon neuronal activation, post-synaptic dendritic spines change in number, morphology and strength. In adult excitatory neurons, structural and functional maturation of local spines mostly rely on Ca^{2+} influx from the extracellular space through glutamate ionotropic receptors. The subsequent release of Ca^{2+} from the endoplasmic reticulum (ER) occurs through Ryanodine Receptors (RyRs) and Inositol (1,4,5)-triphosphate Receptors (IP3Rs) via a mechanism known as Ca^{2+}-induced calcium release (CICR). Despite the overwhelming research conducted over the past decades, the degree of involvement of CICR in synaptic plasticity is not completely understood.

We previously highlighted that the endoplasmic reticulum Ca^{2+} channel ryanodine receptor 2 (RyR2) undergoes activity-dependent genetic re-programming, which alters the abundance of the channel in particular regions of the brain. The submitted thesis describes the contribution of RyR2, and its up-regulation, in dendritic spine homeostasis using different knockout models. *Ryr2* deletion in adult neurons results in cell shrinkage and disturbs spine maintenance. Strikingly, the absence of RyR2 impairs spine biogenesis and remodeling in different paradigms of neuronal plasticity, as in the case of spatial training and administration of psychoactive drugs. Overall, these findings elucidate an underestimated mechanism of intrinsic plasticity, which controls neuronal morphology and has an impact on hippocampal memory acquisition.

2. Table of Contents

3. Introduction

3.1 Brain plasticity.

The human brain is formed by hundreds of billions of neurons highly interconnected with trillions of synapses that receive, integrate and transmit signals, which forms the foundation of cognition and behavior (Ho et al., 2011; Pozo and Goda, 2010). This extensive network has the ability to change and re-adapt architecture continuously throughout an individual's life. Brain connectivity evolves during morphogenesis in developmental stages as a result of a large array of extrinsic (*e.g.*, secreted molecules, membrane-bound ligands) and intrinsic cues (*e.g.*, cytoskeletal remodeling, gene transcription, local protein synthesis) (Ledda and Paratcha, 2017). In adulthood, this process is reduced and optimized to modify neuronal shape and connectivity based on experiences (Grutzendler et al., 2002). This fine-tuned phenomenon is commonly referred as brain plasticity. Neuronal plasticity is visible at multiple levels, from microscopic changes of synapses to remapping of entire circuits. Environments, behaviors, feelings and thoughts contribute to neuronal modifications through activity-dependent mechanisms (Colgan and Yasuda, 2014; Moser et al., 1994; Sando et al., 2017). Brain plasticity is important in physiological processes such as learning and memory, as well as in pathological conditions like brain injuries and neurodegenerative diseases (Bourgeois and Rakic, 1993; Duan et al., 2003; Dumitriu et al., 2010). The neuronal compartment that mainly undergoes activity-evoked re-shaping is the synapse. Synapses are connecting spots of neurons that have the ability to strengthen or weaken over time and depending on the increase or decrease firing patterns of cells (Lee et al., 2016; Lo and Poo, 1991; Oh et al., 2015). Pre-synaptic action potential leads to post-synaptic cascades that can cause the enrichment of neurotransmitter receptors and other intracellular signaling modulating their structure and function. The nature and duration of the stimuli can induce different forms of synaptic plasticity. Numerous forms of short-term plasticity have been described for transient changes of the behavioral state (Colgan and Yasuda, 2014). For example, short-term plasticity is visible upon neuronal burst activity in the range of seconds and results in the pre-synaptic accumulation of Ca^{2+}, thus leading to an increased probability of

neurotransmitter release. On the other hand, long-lasting modifications occur within hours or even days, and require gene transcription and *de novo* protein synthesis. Long-lasting activation affects the number and strength of synapses. As a consequence, groups of firing neurons synchronize, deeply affecting high cognitive processes as shown in different behavioral paradigms (Awasthi et al., 2019; Citri and Malenka, 2008). Despite decades of intense research, the specific ultrastructural events and molecular cascades leading to the experience-driven reshaping of neurons is an open topic in neuroscience. Central to this study is the theory that memory is encoded in the neuronal network. Thus, activity-dependent modification of neurons has been proposed to play a central role for the conversion of transient experiences into persistent memory traces (Hebb, 1949).

3.2 The hippocampus and its role in cognitive function.

The human brain has the outstanding capacity to perform different high cognitive functions. Among them, the most enigmatic ones are learning and memory. Learning is defined as the capacity to acquire and encode information to memory, while memory is defined as the capability to store and retrieve information to guide behaviors (Bays et al., 2011). There are different forms of memory. Declarative and spatial memory are two of the most complex subtypes (Eichenbaum, 2001). Declarative memory, also known as explicit memory, refers to the capacity to consciously recollect experiences and concepts. Part of declarative memory is episodic memory, which consists of the storage of personal experiences, and semantic memory, which is the storage of factual information. Spatial memory instead records information about environment and spatial orientation (Shrager et al., 2007). Multiple memory systems exist and are explicated by specific brain areas. Both declarative and spatial memory are encoded by the medial temporal lobes (MTLs) of the brain. MTLs are comprised of the hippocampus, subiculum and cortical areas, such as entorhinal cortex (Amaral and Witter, 1989).

The hippocampus is one of the most studied and well-described regions of the brain. Although the unique anatomy of these neuronal circuits were described centuries ago, their function remained poorly described until the mid 50s. In those years, the cognitive involvement of the hippocampus started to come to light thanks to the study of a patient,

Mr. Henry Molaison (1926-2008), who was affected by tonic-clonic seizures. Despite taking high doses of anti-convulsant medications, Mr. Molaison could not work nor have a normal life. In 1953, Mr. Molaison had a bilateral medial temporal lobectomy to surgically resect most of the hippocampi (Scoville and Milner, 1957). Surprisingly, after the surgery Mr. Molaison developed severe anterograde amnesia, demonstrating the importance of the hippocampal region in episodic and semantic memory for the first time. Since then, other studies in humans and rodents have confirmed the centrality of the hippocampus in learning (Bird and Burgess, 2008; Neves et al., 2008; Strange and Dolan, 1999) and spatial memory (O'Keefe and Dostrovsky, 1971; O'Keefe and Speakman, 1987). In fact, the hippocampus is involved in the formation of spatial maps of the environment. Moreover, the hippocampus is important for the storage of allocentric spatial information (objects from a stationary point of view), linking memories to the environmental context. Consistently, amnesic patients with hippocampal damage cannot learn, recall spatial layouts and present impaired spatial navigation. In rodents, spatial memory deficits linked to the hippocampus have been found to also affect spatial discrimination tasks, thereby disrupting working memory. The involvement of the hippocampus in the cognitive representation of spatial location has been explained by the presence of special pyramidal cells, called place cells, that fire in a particular environment named the place field (O'Keefe and Dostrovsky, 1971; O'Keefe and Speakman, 1987).

In neurobiology, the hippocampus has served as a model for studying brain function, such as the mechanisms of synaptic plasticity and spatial coding of memories (Ho et al., 2011). Moreover, the hippocampal circuit is related to various neurological and neuropsychiatric disorders, being particularly vulnerable to ischemia, metabolic dysfunction, stress and epileptogenic events (Dhikav and Anand, 2011; Gallagher et al., 1996; Heckers, 2001; Scheff and Price, 1998; Shin et al., 2004). The hippocampus is especially damaged in the elderly and in patients affected by Alzheimer's disease (AD). In fact, loss of neurons and hippocampal shrinkage are core features and pathological criteria of AD (Halliday, 2017). Thus, the understanding of the molecular mechanisms underlying the maintenance of hippocampal plasticity and connectivity is of particularly interest in human physiology and pathology.

3.3 Introduction to the hippocampus: structure.

In humans, the hippocampus is located behind the cerebral cortex in the allocortex of the medial temporal lobe. It has a long, curved form with functionally distinct circuits segregated along the anterior (ventral)-posterior (dorsal) axis, which is symmetric between the two lobes and conserved across species (Figure 3.1A and 3.1C) (Strange et al., 2014). The hippocampal circuitry is shaped as two opposed and locked "C" shapes. One "C" is composed of the dentate gyrus (DG), whereas the second one is represented by the Ammon's horn formed by the CA3, CA2, CA1, the subiculum and the entorhinal cortex (Figure 3.1B and 3.1D) (Amaral and Witter, 1989). The hippocampus is a uni-directional network, which is commonly described as the trisynaptic pathway. This network projects from the Entorhinal Cortex (EC) to the DG granule cells and back to the CA3, CA1, Subiculum and back to the EC (Amaral and Witter, 1989; Bird and Burgess, 2008; Neves et al., 2008; Witter et al., 1988). The EC is connected to the DG via the Perforant Path (PP). The DG projects to the CA3 pyramidal neurons thanks to axonal projections from granule cells anatomically organized as mossy fibers (MF). CA3 cells project to other CA3 pyramidal neurons as well as to the CA1 through the Shaffer collaterals (SC) and the Commissural pathway. CA1 neurons receive input from the PP, sending their axons to the Subiculum (Sb) and then back to the EC. The hippocampus extrinsically projects to other regions of the brain like the lateral septum and the hypothalamus (Strange et al., 2014).

Hippocampal neurons have a laminar distribution structured in different strata: stratum oriens, stratum pyramidale, stratum radiatum and stratum lacunosum-moleculare. The two neuronal subpopulations enriched in the stratum pyramidale are excitatory and inhibitory neurons. Pyramidal cells represent the most abundant subpopulation of the excitatory glutamatergic neurons (Figure 3.2A). Inhibitory interneurons are only 11% of all neurons in the CA3 and CA1 regions (Bezaire and Soltesz, 2013). The main role of pyramidal neurons is to integrate the synaptic input into action potentials across the trysinaptic pathway, which is at the base of the functional involvement of the hippocampus in learning and memory formation (Bekkers, 2011; Spruston, 2008).

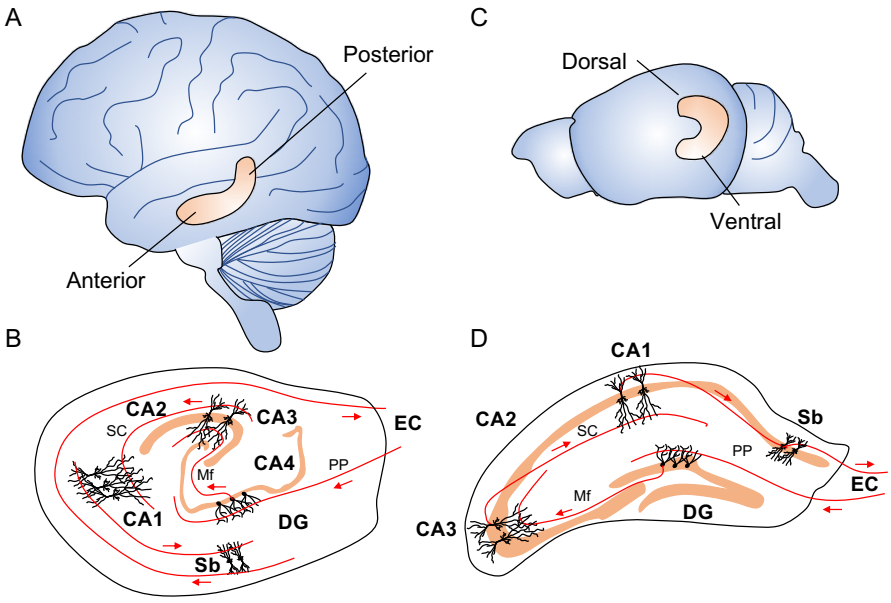

Figure 3.1 The hippocampus in the human and mouse brain. A) Schematic illustration of the hippocampus in the human brain. B) Schematic illustration of the trisynaptic pathway projections in the sagittal section of the human hippocampus. The Enthorinal cortex (EC) projects to the granule cells of the dentate gyrus (DG) through the Perforant Path (PP). The DG projects to the CA3 neurons through the mossy fibers (MF). The axonal projections of the CA3 pyramidal cells, the Shaffer collaterals (SC), extend to the CA1 neurons. CA1 neurons extend their axons to the Subiculum (Sb) and back to the EC. C) Schematic illustration of the hippocampus in the mouse brain. D) Schematic illustration of the trisynaptic pathway projections in the sagittal section of the mouse hippocampus.

Even though the hippocampus has often been interpreted as a framework of homogeneous cells, recent experimental studies suggest that it might contain discrete structural and functional subtypes of neurons (Nelson et al., 2006; Soltesz and Losonczy, 2018). Pyramidal neurons take their name from their pyramid-shaped soma. They are found in the CA3 and CA1 with unique dendritic morphology (Figure 3.2B) (Bekkers, 2011). While short basal dendrites emerging from the top rounded cell body of pyramidal cells stratify the stratum oriens (Spruston, 2008), apical dendrites from the pointy end of the soma radiate in the stratum radiuatum and stratum lacunosum-moleculare (Amaral and Witter, 1989). CA3 cells typically present a main apical dendrite and tuft, with secondary dendrites branching closer to the soma than the CA1 neurons (Spruston, 2008). The morphology of CA1 apical dendrites vary from neuron to neuron. Some CA1 cells present only one main apical trunk whereas others show a bifurcating arborization before reaching

the tuft. A single axon forming pre-synaptic buttons emerges from the base of the soma of CA1 cells and projects to the subiculum (Bekkers, 2011). CA1 cells receive synaptic input at the soma and along dendrites through dendritic spines. Only the soma and axon receive inhibitory γ-aminobutyric acid (GABA)-ergic input (Pouille and Scanziani, 2001). Most excitatory input projected to pyramidal cells comes from multiple sources (Amaral and Witter, 1989; Bird and Burgess, 2008; Neves et al., 2008; Witter et al., 1988). CA1 basal and proximal apical dendrites receive projections primarily from CA3 axons through the Schaffer collateral. The CA1 apical tuft receives input from the EC through the performant path and the thalamic nucleus reuniens.

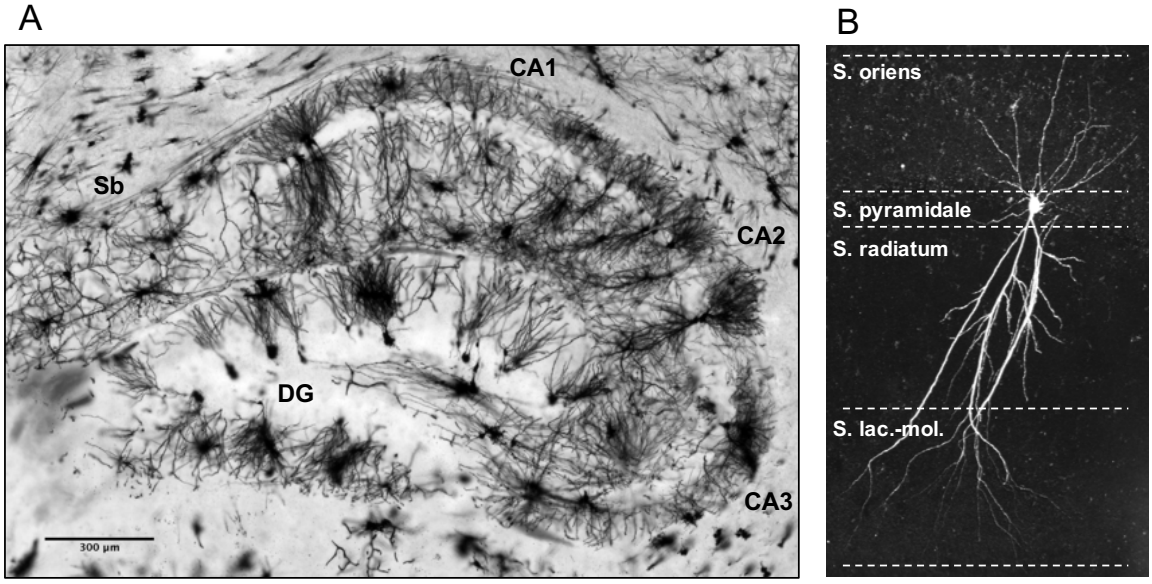

Figure 3.2 The CA1 pyramidal neurons of the hippocampus. A) Golgi staining shows the distribution of the neuronal subpopulations in the hippocampus of mice. Subiculum (Sb); dentate gyrus (DG). B) CA1 pyramidal neuron projects in the different strata.

3.4 Pyramidal neurons: synapses.

Synapses are cellular substructures that regulate neuron-to-neuron transmission of electrochemical signals (Spruston, 2008). These domains were first described by Santiago Ramón y Cajal who postulated, by using the silver staining of Camillo Golgi and a camera lucida, that these protrusions were points of contact between neurons (Yuste, 2015). The term synapse comprises both presynaptic axon terminals (pre-synaptic compartments) and post-synaptic compartments, which are located either in the soma or in dendritic spines

(Figure 3.3)(Sudhof and Malenka, 2008). Pre- and post-synaptic compartments are divided by a synaptic cleft of approximately 15-25 nm that is usually stabilized by adhesion molecules. Other components of synapses are neighboring astrocytes that respond to synaptic activity and influence neurotransmission. Synaptic activity occurs via vesicular release of neurotransmitters, which change resting membrane potentials of cells eventually triggering excitatory action potentials (EPSPs)(Hunt and Castillo, 2012). Glutamate is the most important neurotransmitter in pyramidal hippocampal cells. Glutamate is a non-essential amino acid that is synthetized in presynaptic terminals. This excitatory transmitter is released into the synaptic cleft through synaptic vesicles in a Ca^{2+}-depended fashion. In the cleft, it can bind ionotropic and metabotropic receptors located in the post-synaptic membrane. Ionotropic receptors are transmembrane ligand-gated ion channels, which main classes are glutamate ionotropic receptors, N-methyl-D-aspartate receptor (NMDAR) and α-amino-3-hydroxy-5-methyl-4-isoxazolepropionic acid receptors (AMPAR)(Luscher and Malenka, 2012). NMDA and AMPA receptors are glutamate-sensitive channels that lead to influx/efflux of Na^+, Ca^{2+} and K^+ between the extracellular and the intracellular space. Activation of these receptors is the main cause of the post-synaptic depolarization, which may trigger different forms of synaptic plasticity (Luscher and Malenka, 2012). Metabotropic receptors are instead G- coupled protein receptors, which initiate cascades triggering the activation/inhibition of other channels and molecular cascades. Hippocampal cells are rich with different metabotropic glutamate receptor subtypes (mGluRs). Glutamate-dependent activation of mGluRs induces the opening of intracellular Ca^{2+} channels and a broader synaptic activation. Ionotropic and metabotropic receptors cluster together in a portion of dendritic spines that binds the cytoskeleton (Oh and Derkach, 2005). Such a protein-enriched portion is commonly referred as postsynaptic density (PSD) (Sheng and Hoogenraad, 2007).

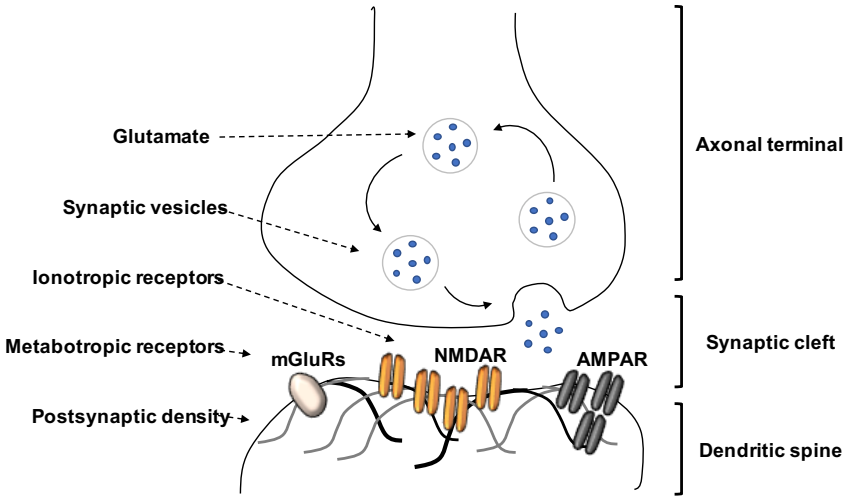

Figure 3.3 Schematic representation of a synapse. Presynaptic action potentials in the axonal terminal (presynaptic compartment) lead to the release of glutamate-containing vesicles in the synaptic cleft. As result, ionotropic and metabotropic receptors (N-methyl-D-aspartate receptor, NMDAR; α-amino-3-hydroxy-5-methyl-4-isoxazolepropionic acid receptors, AMPAR; metabotropic glutamate receptors, mGluRs) located in postsynaptic densities of dendritic spines allow the entrance of ions and the further trigger of other molecular cascades.

Postsynaptic dendritic spines are highly dynamic structures that vary in terms of content and morphology being heavily influenced by developmental stage, neuronal type and specific dendric location (Figure 3.4A) (Chicurel and Harris, 1992; Harris and Kater, 1994; Trommald and Hulleberg, 1997). Spines are classified based on their morphology as thin, stubby, mushroom or branched (Figure 3.4B) (Harris and Stevens, 1989). Thin spines have a total length greater than the neck diameter and a small head (<0.6 um) (Figure 3.4C). In the CA1 the neuron spine neck diameters is about 0.04-0.5 μm, while the length range 0.2-2 μm (Figure 3.4C) (Harris and Stevens, 1989). Stubby spines are shorter, without a neck and are considered to be immature (Figure 3.4C). Mushroom spines have a large head (>0.6 um) and a constricted neck (Figure 3.4C). These are the larger, stable spines and are usually associated with memory storage (Rochefort and Konnerth, 2012). Few spines are branched with multiple or perforated heads. The functional significance of perforated spines is still unclear (Harris et al., 1992). Rarely present in adult neurons, filipodia spines are formed by a long neck without a bulbous head (Ozcan, 2017). Assembly and maintenance of dendritic spines seems to be independent of synaptic glutamate release

(Sando et al., 2017; Sigler et al., 2017). However, recent *in vivo* data indicate that there are separate populations of stable and more plastic spines, and that spines change upon NMDARs-dependent activation (Berry and Nedivi, 2017; Gu et al., 2014; Noguchi et al., 2011; Pfeiffer et al., 2018; Rochefort and Konnerth, 2012).

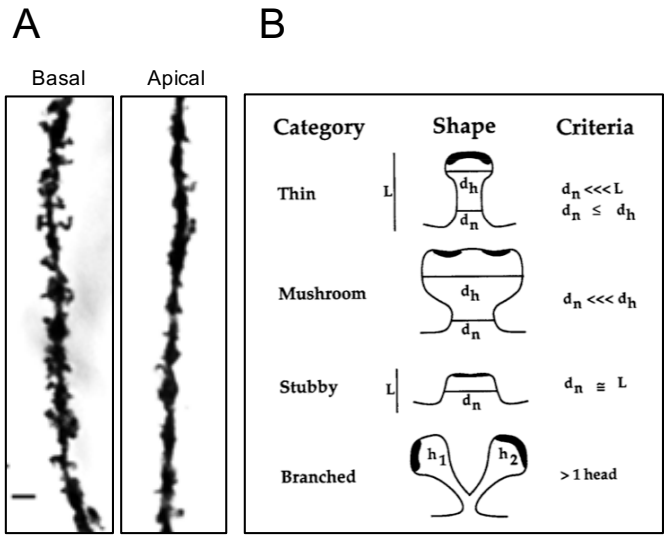

C

	Dentate gyrus[c]	CA3[b]	CA1[c]
Neck diameter (μm)	0.09-0.54	0.20-1.00	0.038-0.46
Spine length (μm)	0.02-1.78	0.60-6.50	0.160-2.13
Spine volume (μm^3)	0.003-0.23	0.13-1.83	0.004-0.56
Postsynaptic density area (μm^2)	0.003-0.23	0.01-0.60	0.008-0.54

Figure 3.4 Dendrites and dendritic spines of CA1 pyramidal neurons of the hippocampus. A) Golgi staining shows different spine content and composition in basal and apical dendrites on CA1 cells. Scale bar= 3 μm. B) Morphological classification of spines based on the ratiometric criteria among the length of the spine neck (L), the diameter of the spine head (d_h), the diameter of the spine neck (d_n) and the number of heads (Harris et al., 1992). (C) Dentate gyrus [c](Trommald and Hulleberg, 1997), CA3 neurons [b](Chicurel and Harris, 1992; Harris and Kater, 1994) and CA1 neurons [c](Harris and Stevens, 1989).

3.5 Pyramidal neurons: synaptic plasticity.

The synaptic strength of pyramidal cells can be modulated by different forms of stimulation. Low frequency stimulation usually causes synaptic weakening and results in

long-term depression (LTD), whereas high frequency stimuli enhance synaptic strength and lead to long-term potentiation (LTP) (Citri and Malenka, 2008). In this regard, hippocampal cells were the first neuronal type reported to undergo long-lasting activity-dependent changes. In fact, repetitive excitations lead to synaptic potentiation that can last for hours or even days with cognitive implications, as in the case of learning and memory. Hippocampal LTP activates discrete spines without affecting the state of adjacent microdomains. In adult excitatory glutamatergic neurons, the formation and maintenance of LTP and LTD rely on postsynaptic ionotropic NMDARs and AMPARs (Chua et al., 2010; Sheng and Hoogenraad, 2007). AMPARs provide most of the current at resting state, while NMDARs do not contribute much to basal synaptic activity. The activity of those channels strongly depends on membrane voltage, as the presence of extracellular Mg^{2+} blocks them. However, upon cell depolarization and in concomitance with glutamate, Mg^{2+} displacement from NMDARs allows the post-synaptic entrance of ions like Na^{+} and Ca^{2+} (Mayer et al., 1984). As a consequence, NMDARs can trigger LTP with a compartmentalized increase of Ca^{2+} only in active spines. Thus, single synapses from the same neuron or even dendrite can be involved in different synaptic circuits encoding separate information (Matsuzaki et al., 2004). NMDAR-dependent increase of Ca^{2+} levels leads to intracellular signaling cascades dependent on several protein kinases. Among those implicated in LTP maintenance, calcium/calmodulin-dependent protein kinase II (CaMKII), cyclic adenosine monophosphate-dependent kinase (PKA), protein kinase C (PKCv or PKMζ) and extracellular signal-regulated kinase (ERK)/mitogen-activated protein kinase (MAPK) are the most described (Malenka et al., 1989). The activation of kinases usually triggers phosphorylation changes of targets in a localized manner, although it can result in a signaling cascade that can extend to the nucleus. In combination, the activation of kinases leads to the increased conductance of synaptic AMPARs and an enriched presence of those channels into PSDs. Furthermore, actin polymerization and depolymerization preserves the cytoskeletal scaffold, increasing spine stability. Altogether, these events shape the enlargement of dendritic spines (Matsuzaki et al., 2004). In the case of LTD, the limited activation of NMDARs and the mild post-synaptic influx of Ca^{2+} lead to activation of protein phosphatases, which in turn trigger endocytosis of AMPARs from PSDs and their further degradation. Loss of AMPARs during LTD may be the cause of

spine regression (Nusser et al., 1998). Thus, it is commonly acknowledged that LTP and LTD are critical steps for the structural modification of synapses. Along with other mechanisms (*e.g.* metaplasticity and homeostatic plasticity), those bidirectional changes are the main regulators of synaptic morphology and strength (Matsuzaki et al., 2004; Nusser et al., 1998). Several studies point to a correlation between synaptic plasticity and formation of long-term memory (Bliss and Lomo, 1973; Martin et al., 2000; Morris and Frey, 1997). Defective synaptic plasticity of pyramidal cells has been linked to impaired hippocampal-dependent memory in many studies using both genetic and pharmacological treatment. In rodents, pharmacological inhibition as well as deletion of the NR1 subunit of NMDARs produced defective LTP associated with reduced spatial learning (Morris and Frey, 1997). Consistently, overexpression of the NMDAR subunit NR2B enhanced LTP and spatial learning (Tang et al., 1999).

3.6 Synaptic plasticity: the second messenger Ca^{2+}

Four billion years ago, ten billion years after the formation of the elements, cells started to adapt to signals using finely-tuned messengers (Clapham, 2007). Because of its abundance and high toxicity, Ca^{2+} became tightly regulated within cells (Berridge et al., 2003). As a result, the basal cytosolic gradient (100-200 nM) of cells is 10,000-fold less compared to the extracellular space, where it can rise to up to 1000 nM upon cell activation (Berridge et al., 2000; Carafoli, 2004; Clapham, 2007). Cells have developed specialized extrusion mechanisms and Ca^{2+} reservoirs. The main intracellular Ca^{2+} store is the sarcoplasmic/endoplasmic reticulum in which Ca^{2+} concentration can rise to up to 500 μM. Moreover, proteins have adapted to Ca^{2+} in charge and shape (Clapham, 2007). Ca^{2+} has become the universal second messenger of cells due its versatility in regulating a variety of processes including fertilization, proliferation, differentiation, contraction, secretion and cell death (Carafoli, 2004). In fact, as a ubiquitous second messenger, Ca^{2+} regulates gene expression, protein synthesis, cytoskeleton dynamics and local signaling (Figure 3.5A). Thus, Ca^{2+} is particularly important in neuronal physiology. In the pre-synaptic terminal, for example, Ca^{2+} triggers the release of neurotransmitters. Furthermore, as described above, post-synaptic Ca^{2+} influences both LTD and LTP forms of plasticity. Consequently, Ca^{2+} regulates a broad spectrum of neuronal processes, including excitability, morphology

and plasticity. In pyramidal neurons, NMDARs and other channels localized to the plasma membrane of dendritic spines regulate the initial cytosolic Ca^{2+} influx. Following NMDAR-depend Ca^{2+} influx, Ca^{2+} levels can be further enhanced by voltage-gated calcium channels (VGCCs). Hippocampal neurons are enriched with a subclass of VGCCs called L-type calcium channels (Rochefort and Konnerth, 2012).

Additionally, Ca^{2+} rises via inositol triphosphate receptor (IP_3R) and ryanodine receptor (RyR)-mediated release from the endoplasmic reticulum (ER) via a mechanism called calcium-induced calcium release (CICR) (Park and Spruston, 2012). The function of CICR is to amplify and potentiate the plasmalemma Ca^{2+} influx. Different mechanisms trigger the opening of IP_3R and RyR channels. Metabotropic mGluR determines the recruitment of G-proteins, thereby activating phospholipase C (PLC) to decompose the phosphatidylinositol 4,5-bisphosphate (PIP_2) into inositol trisphosphate (IP_3) and diacylglycerol (DAG). High content of IP_3 opens IP_3Rs on the ER to release Ca^{2+} (Nakamura et al., 1999; Segal and Korkotian, 2014; Spacek and Harris, 1997; Wu et al., 2017). Additionally, activation of Group I mGluRs activate the adenylyl cyclase (AC), which converts ATP to cAMP with the consequent activation of cyclic adenosine monophosphate-dependent kinase (PKA). In parallel, the NMDAR-dependent supra-threshold influx of Ca^{2+}, followed by the activation of VGCCs, leads to the activation of RyRs (Baker et al., 2013; Leybaert and Sanderson, 2012; Peng et al., 2016; Rizzuto and Pozzan, 2006; Van Petegem, 2012, 2015). Elevation of cAMP and increased Ca^{2+} concertation trigger to intracellular signaling cascades that involve several other protein kinases (*e.g.* CaMKII, PKCv, PKMζ and MAPK). In particular, the activation of the PKA-Rap1-ERK pathway results in the phosphorylation of CREB, a transcription factor important for the stimulus-evoked nuclear expression of immediate early genes (*e.g. c-fos*, *Zif268* and *C/EBPs*). ER Ca^{2+} homeostasis relies also on sarco/endoplasmatic-reticulum Ca^{2+} ATPase (SERCA) pumps, since it promotes ER Ca^{2+} refilling. In pyramidal neurons, less than 48% of spines contain an ER. Among those, 58% of immature spines and more than 80% of mushroom have an ER, suggesting a predominant role of CICR in the maturation of synapses (Spacek and Harris, 1997).

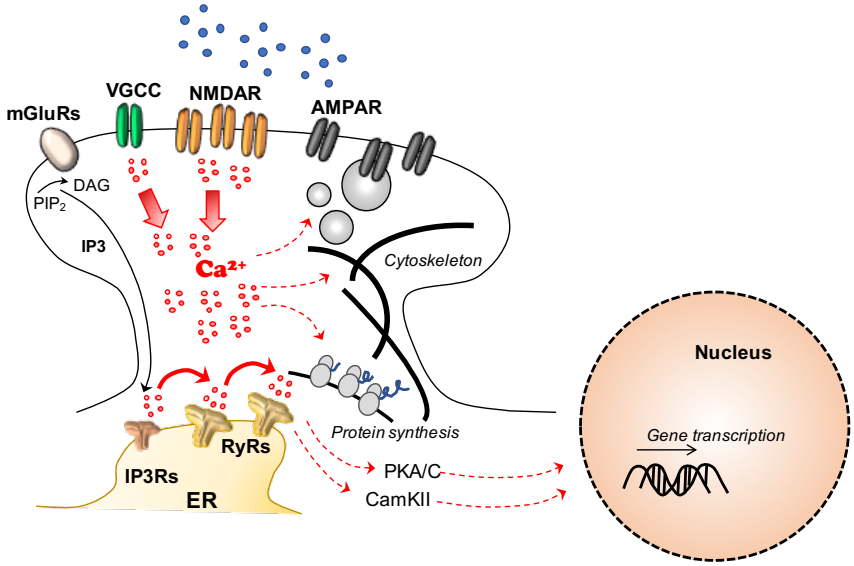

Figure 3.5 Schematic representation of a dendritic spine upon activation. Cytosolic Ca^{2+} concentration rises upon NMDAR and VGCC activation. The increased Ca^{2+} level triggers CICR with the local release of Ca^{2+} from the ER through IP3Rs and RyRs. IP3Rs are activated by metabotropic mGluR, which trigger the decomposition of the phosphatidylinositol 4,5-bisphosphate (PIP_2) into inositol trisphosphate (IP_3) and diacylglycerol (DAG). Ca^{2+} modulates synaptic plasticity affecting AMPAR trafficking, cytoskeleton dynamics and local proteins synthesis. Finally, Ca^{2+} leads to the activation of different protein kinases (*i.e.* PKA/C and CamKII) important for the nuclear expression of immediate early genes.

3.7 Ryanodine receptors: expression and activity-dependent transcription.

RyRs are homotetrametic channels of 2.2 MDa, which are encoded by 3 independent genes containing more than 100 exons (Takeshima et al., 1989; Van Petegem, 2015). In mammals, there are 3 RyR isoforms differently expressed in various tissues. RyR1 is predominantly expressed in skeletal muscle (Takeshima et al., 1989). In humans, the RyR1 gene is located on chromosome 19q13.2 and contains 104 exons. RyR2 is mostly expressed in the heart and brain and is encoded by a gene on chromosome 1q43 and containing 102 exons (Nakai et al., 1990). RyR3 is encoded by 103 exons on chromosome 15q13.3-14 and was originally discovered in the brain, although it is mainly expressed in other organs, such as skeletal and smooth muscle and endocrine tissues (Hakamata et al.,

1992). All the three RyRs isoforms are expressed in the brain (Giannini et al., 1995). In rodents, the expression pattern of RyRs varies considerably in embryos, postnatal animals and adults (Figure 3.6A-C) (Mori et al., 2000). For example, *Ryr2* expression is not detectable in the forebrain of rats at birth, whereas it is strongly upregulated at P7. Conversely, RyR3 mRNA levels are decreased in the caudal cerebral cortex after birth, while it remains highly expressed in the hippocampus in adulthood (Figure 3.6B). The expression pattern of RyR1 does not differ much during development and in adult brains, being mainly restricted to the Purkinje cells of the cerebellum (Figure 3.6A). In adulthood, RyR2 is enriched in the olfactory bulbus, cortex, hippocampus and granular cell layer, whereas RyR3 is mostly present in basal ganglia and in the CA1 layer of the hippocampus (Figure 3.6C). In pyramidal neurons of the hippocampus, RyRs are localized in all subcellular compartments, including the soma, axons, dendritic spines and dendritic shafts (Sharp et al., 1993).

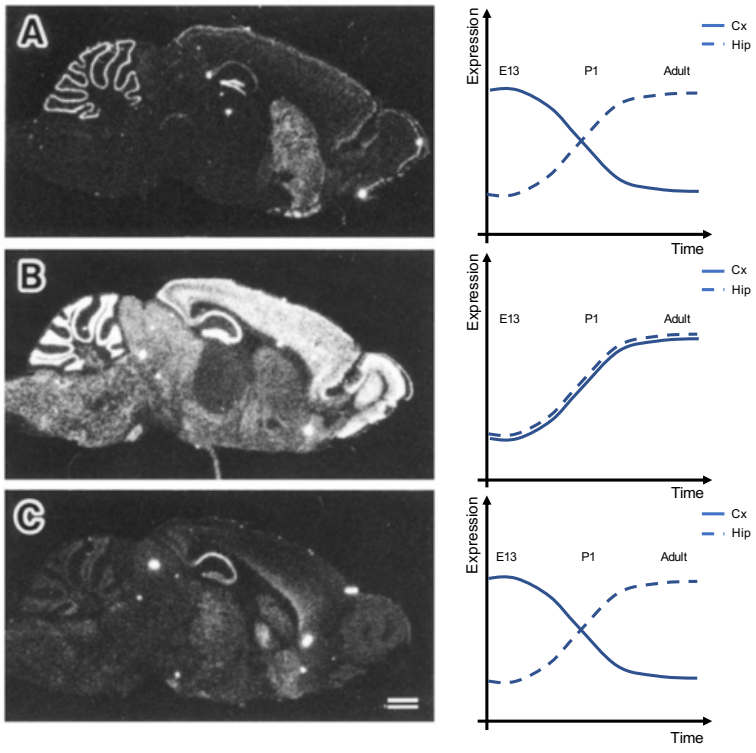

Figure 3.6 Expression pattern of RyRs. (A) RyR1 expression increases in the DG of the hippocampus at post-natal ages, while it is diminished in all other regions, including the cortex. (B) RyR2 expression level is barely detectable before birth. From P1, RyR2 expression rises in the forebrain and in the cerebellum. (C) RyR3 is abundant in the cortex during development and is then restricted to the hippocampus from P1 (Mori et al., 2000).

Although, RyR isoforms are constitutively expressed in the brain, they can be selectively upregulated in an activity-dependent manner by different transcription factors. Among the three isoforms, the transcription of RyR1 remains perhaps the most elusive. Conversely, RyR3 expression has been previously elucidated, since it seems to be epigenetically regulated by methyl CpG binding protein 2 (Mecp2) (Torres et al., 2017). In fact, the methylation of discrete cytosines in the promoter of RyR3 leads to the transcription of the gene in the hippocampus of rodents exposed to an enriched environment (EE) paradigm. In the same region of the brain, RyR3 content was also shown to rise after testing mice in the Morris water maze (MWM) (Adasme et al., 2011). RyR2 is the isoform more prone to be up-regulated and it undergoes activity-evoked transcription via a separate mechanism. Due to the presence of three CREB-binding response elements (CRE) in the *Ryr2* promoter region, neuronal activity enhances CICR Ca^{2+} transients through CREB-dependent genetic programming of RyR2 in specific circuits of the brain (Zhao et al., 2000; Ziviani et al., 2011). RyR2 up-regulation is itself required for long-term phosphorylation of CREB in a positive-feedback loop. As a result, spatial training (Zhao et al., 2000) or the exposure to psychoactive drugs up-regulate the channel in activated neuronal circuities (Figure 3.7) (Kurokawa et al., 2010; Ziviani et al., 2011). As an example, nicotine-mediated up-regulation of RyR2 in the mesolimbic-dopaminergic pathway is crucial in the behavioral sensitization of locomotor activity (Ziviani et al., 2011). In the same way, exposure to methamphetamine up-regulates RyR2 in the limbic forebrain (Kurokawa et al., 2011; Kurokawa et al., 2010). Furthermore, RyR2 upregulation has been associated with chronic administration of the psychoactive drug cocaine. Chronic treatment with cocaine increases the expression of the channel in the hippocampus and the ventral midbrain, without affecting its pattern in other regions of the brain (Ziviani et al., 2011).

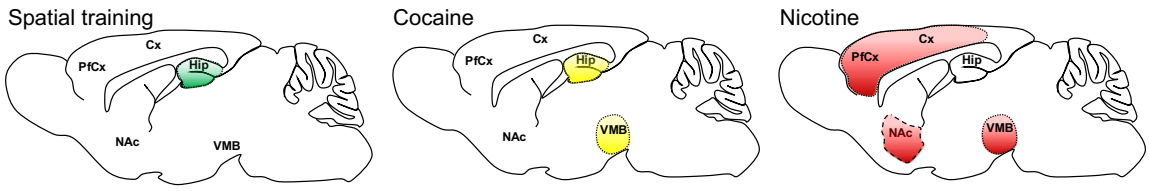

Figure 3.7 Activity-dependent re-programming of RyR2 after spatial training and chronic administration of nicotine or cocaine. Schematic representation of the brain (Cx, cortex; PfCx, Prefrontal Cortex; Hip, hippocampus; NAc, nucleus accumbens; VMB ventral midbrain). Spatial training in the MWM up-regulates *Ryr2* in the hippocampus (Adasme et al., 2011). Chronic treatment (once a day for 8 days, 15mg/kg) with cocaine rises RyR2 only in the Hip and VMB. Chronic treatment (once a day for 5 days) with nicotine rises RyR2 in the Cx, PfCx, NAc and VMB. (Ziviani et al., 2011).

3.8 Ryanodine receptors: structure.

All three RyR isoforms share 70% sequence identity and form large homotetrametric channels of approximately 2 MDa. The C-terminal region of each subunit consists of 500 amino acid residues that form the transmembrane ion-conducting domain (Coronado et al., 1994; Lanner et al., 2010). The cytoplasmic region is defined by the remaining ~ 4500 amino acids that compose the largest mushroom-like structure. RyRs are high conductance channels, for both monovalent and divalent cations, which have low Ca^{2+} affinity (Meissner, 2017; Van Petegem, 2012). This characteristic makes them ideal channels for conducting large amounts of Ca^{2+} over long periods of time (>5ms). The cytosolic concentration of Ca^{2+} directly regulates the probability that the channels will open. Low cytosolic Ca^{2+} concentrations (100-200 nM) result in a closed state, while channels have the highest probability of opening at micromolar levels (ca. 10 μM). Cytosolic concentrations above 10 μM instead decrease the aperture of the channels, which points to the presence of different Ca^{2+} binding sites with different affinities (Bezprozvanny et al., 1991). The structural integrity of these channels is of prime importance to their function, and any small conformational changes to their structure can result in severe pathological repercussions. Over 300 mutations are associated especially with skeletal and cardiac disorders (Medeiros-Domingo et al., 2009). *RYR1* mutations cause muscular disorders, including malignant hyperthermia (MH), central core disease (CCD) and atypical period paralyses. *RYR2* mutations lead to cardiac arrhythmic diseases, such as catecholaminergic

polymorphic ventricular tachycardia (CPVT) and arrhythmogenic right ventricular dysplasia type 2 (ARVD2) (Jiang et al., 2005; MacLennan et al., 1990; Zhang et al., 1993; Zhou et al., 2010). RyRs can also undergo aberrant posttranslational modifications in pathological conditions, which destabilize the conformation of the channels resulting in Ca^{2+} leakage (Marx et al., 2000; Takasago et al., 1991; Wehrens et al., 2003).

Several ligands and subunits bind the cytoplasmic portion and regulate the structure and function of the channel (Peng et al., 2016; Van Petegem, 2012, 2015). In particular, all four homotretramers bind FK506-binding proteins (FKBPs) of approximately 110 amino acids, which stabilize the conformational state of the channel. Likewise, RyRs are regulated by multiple factors and subunits including calmodulin (CaM), protein kinases (PKA and CaMKII) and phosphatases, active oxygen species, ATP, Mg^{2+} and Ca^{2+} itself (Brillantes et al., 1994; Porter Moore et al., 1999; Smith et al., 1986; Wang and Best, 1992). RyRs can also mechanically interact with other ion channels required for the excitation-contraction coupling that is essential for the mechanical function of muscle cells. In the sarcolemma of skeletal muscles, for example, RyR1 binds dihydropyridine receptor ($Ca_v1.1$), leading to Ca^{2+} release. In cardiomyocytes, the functional interaction between L-type Ca^{2+} channels and RyR2 results in the induction of CICR (Santulli et al., 2018). In neurons, RyR function and possible interaction partners are still under investigation.

3.9 Ryanodine receptors: synaptic plasticity.

RyRs have been shown to play a crucial role for some forms of neuronal plasticity (Grigoryan and Segal, 2016; Johenning et al., 2015; Lacampagne et al., 2017; Ohashi et al., 2014; Vlachos et al., 2009). In early postnatal weeks, excitatory neurons require NMDAR activation and the consequent engagement of CICR for the maturation and clustering of dendritic spines (Emptage et al., 1999; Kovalchuk et al., 2000; Kwon and Sabatini, 2011; Sabatini et al., 2002). In developing neurons, NMDAR-dependent activations determine cytosolic Ca^{2+} influx that triggers CICR. Subsequently, CICR induces the formation and propagation of Ca^{2+} waves from the activated spines along proximal dendrites, leading to the stimulation of neighboring protrusions (Figure 3.8). As a result, dendritic segments and adjacent developing spines synergistically mature and form clusters (Lee et al., 2016; Oh et al., 2015). This scenario does not fully occur in old age, when

NMDA receptors are the main contributors of cytosolic Ca^{2+} transients. In adulthood, dendritic spines represent functional distinct structures in which Ca^{2+} transients remain compartmentalized in the spine head. At this stage, the contribution of CICR to the formation and propagation of dendritic and synaptic Ca^{2+} waves is strongly reduced (Figure 3.8) (Kovalchuk et al., 2000; Lee et al., 2016; Sabatini et al., 2002). In line with this evidence and compared to wild type littermates, 3 months-old naïve *Ryr3* knockout mice exhibit the same spine content and number of mushroom spines in CA1 neurons of the hippocampus (Liu et al., 2014). On the contrary, and despite the normal neuronal structure of pyramidal cells, CA1 field recordings from *Ryr3* knockout mice show an altered maintenance of LTP (Futatsugi et al., 1999; Shimuta et al., 2001). This effect was observed in other pharmacological studies over the years, further supporting the contribution of RyRs on LTP (Arias-Cavieres et al., 2018; Grigoryan et al., 2012; Harvey and Collingridge, 1992; Martin and Buno, 2003; Obenaus et al., 1989; Welsby et al., 2006). A recent and possible explanation for this discrepancy may come from the involvement of RyRs in the back propagating action potential (bAP) activation of dendritic spines. Neuronal backpropagation is a secondary process in which, after an action potential, another voltage spike is triggered from the soma back to the dendritic arbor where the input originated. During this phenomenon, RyRs mediate local Ca^{2+} transients within single spines, which affect the future integration of signals (Johenning et al., 2015). *In vitro* data using primary neurons also suggest the possible involvement of RyR Ca^{2+} spikes in the long-term plasticity of spines (Adasme et al., 2011; More et al., 2018). Back in the '90s, studies showed that the caffeine-dependent Ca^{2+} transients produced spinogenesis in 3-week-old hippocampal neurons. This neuronal plasticity was blocked by pharmacological inhibition of RyRs, indicating that the caffeine-induced Ca^{2+} spikes and the formation of new spines relies on ryanodine-sensitive Ca^{2+} stores (Korkotian and Segal, 1999). In another experiment, primary hippocampal neurons co-treated with the antagonist ryanodine (50 μM) and brain-derived neurotropic factor (BDNF), a well-known effector that produces spine formation and maturation, do not change the content of dendritic spines over time (Adasme et al., 2011).

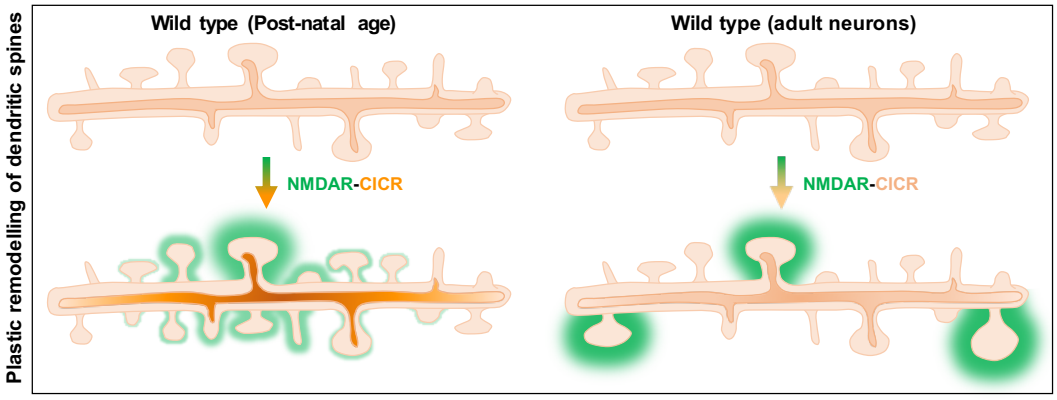

Figure 3.8 Schematic representation of CICR in post-natal age and adulthood. In the first two post-natal weeks, the activation of NMDA receptors is coupled with CICR, resulting in the formation and propagation of Ca^{2+} waves along proximal dendrites. This process strongly contributes to the clustering and maturation of dendritic spines during development. Already after the two post-natal weeks, NMDA receptors become the main trigger of the cytosolic Ca^{2+} influx, whereas the contribution of CICR is narrowed down. NMDAR-dependent Ca^{2+} transients remain compartmentalized in the spine head without spreading along dendrites.

3.10 Ryanodine receptors: cognitive implications.

RyRs have been shown to regulate a variety of cognitive functions and behaviors. Early studies have shown that pharmacological inhibition of RyRs results in memory defects. Dandrolene-mediated inhibition of RyRs decreases associative memory, while administration of the RyR agonist 4-Chloro-m-cresol improves memory consolidation in landfowl (Baker et al., 2010; Edwards and Rickard, 2006). Consistently, intracranial injection of ryanodine at inhibitory concentrations induces memory deficits in rats (Galeotti et al., 2008). Little is known about the physiological contribution of RyR1 and RyR2 in the brain. This is mainly due to the lethal effect of RyR1 and RyR2 knockout in rodents (Takeshima et al., 1994; Takeshima et al., 1998). Since RyR3 knockout mice are viable, a large amount of data has helped to unveil the contribution of RyR3 to neuronal physiology. RyR3 deficient mice exhibit a broad spectrum of neurological defects, such as decreased social behavior and an increased locomotion (Futatsugi et al., 1999; Kouzu et al., 2000; Matsuo et al., 2009; Shimuta et al., 2001; Takeshima et al., 1996). Interestingly, *Ryr3* knockout mice seem to have normal or even superior spatial memory, but a decreased capacity to learn the relocation of the target when tested in the Morris Water Maze (MWM). The importance of RyR2 in cognition has been supported by previous studies in various

experimental models. Selective downregulation of *Ryr2* by intracranial injection of oligonucleotides (ODNs) has been shown to produce an anti-depressant like phenotype in mice tested in the Force swimming test. Using the same approach, *Ryr2* downregulation has been recently shown to impair spatial memory in mice tested in the Oasis Maze, a dry version of the MWM (More et al., 2018). Some other indications of the role of RyR2 in cognition come from the availability of knock-in mutations associated with cardiac arrhythmias and heart failure. Disease-like mutations of RyR2 produce a leaky channel, burst activity and seizures (De Crescenzo et al., 2012; Lehnart et al., 2008; Liu et al., 2012). Equally important, chronically restrained and stressed mice exhibit increased levels of oxidized, nitrosylated and hyperphosphorylated RyR2, which ultimately leads to the depletion of the stabilizing subunit FKBP12.6/calstabin2 and consequent ER Ca^{2+} leakage (Liu et al., 2012). Genetic manipulation of the PKA phosphorylation site in the RyR2 protein as well as oral supplementation of the channel stabilizer S107 (or Rycal) prevent aberrant ER Ca^{2+} release and improve stress-induced cognitive dysfunction. Consistent with this line of evidence, FKBP12.6/calstabin2 knockout induces neuronal RyR2 Ca^{2+} leakage, reduces LTP and impairs learning and long-term memory of mice (Yuan et al., 2016). This effect on cognitive performance seems to be highly specific to RyR2, since stress-induced cognitive dysfunction does not depend on RyR1 (Liu et al., 2012).

3.11 Ryanodine receptors: neurodegenerative diseases.

In humans, RyR dysregulation has been associated with mild cognitive impairment (MCI) as well as Alzheimer's disease (AD) (Bruno et al., 2012; Lacampagne et al., 2017; Oules et al., 2012), In fact, *de novo* mutations, post-translational modifications and aberrant expression of *RYRs* have been linked to the Ca^{2+} hypothesis of AD. In this context, alterations of intracellular Ca^{2+}-dependent pathways were reported in samples from human patients and models of AD. For example, RyR expression was reported to be increased at early stages of sporadic and monogenic early onset AD (Bruno et al., 2012; Kelliher et al., 1999). This increase was largely confirmed also in AD mouse models of $PS1^{M146V}$ and 3xTG-AD (Tau^{P301L}, $APP^{K670N/M671L}$, $PS1^{M146V}$). In contrast, RyRs were shown to be strongly reduced in subiculum, CA1-CA4 regions at late stages of AD (Antonell et al., 2013). These

contradictory results could indicate that RyRs are differentially regulated in different brain regions and/or stages of the disease. In line with this theory, the deletion of *Ryr3* in young $APP^{swe}PS1^{L166P}$ mice resulted in elevated Aβ content and cell hyperexcitability (Liu et al., 2014). In adult $APP_{swe}PS1_{L166P}$ mice, RyR3 knockout prevented neuronal excitability and rescued the loss of mature spines.

Many cases of presenilin (PS) mutations were reported to deregulate RyR function, as in the cases of FAD-linked PS1 and PS2 mutations. Notably, exogenous Aβ oligomers caused a marked increase of RyR activity of up to 10-fold. Interestingly, pharmacological blockage of RyRs reduced Aβ production in primary neurons. Furthermore, treatment with dantrolene diminished the Aβ load and histological lesions in APP_{swe} mice (Tg2576) (Del Prete et al., 2014; Oules et al., 2012). RyR2 has been shown to undergo post-translational modifications caused by PKA phosphorylation, oxidation/nitroylation and depletion of the stabilizing subunit calstabin2 in both human sporadic AD as well as in $APPPS1_{K670N/M671L}$ $PS1_{M146V}$ and 3xTg-AD transgenic models. Oral supplementation of Rycal prevents RyR2 Ca^{2+} leakage and therefore rescues synaptic plasticity, cognitive function and plaque formation (Lacampagne et al., 2017). A genetic confirmation that supports the importance RyR2 stability comes from crossing APP/PS1 and $RyR2_{S2808A}$ knock-in mice. The fact that RyR2-$_{S2808A}$ cannot be phosphorylated by PKA produced an overall reduction of the pathology in the brain and improved cognitive performance. In line with these findings, rodents constitutively expressing the leaky PKA $RyR2_{S2808D}$ channel showed early cognitive impairment and synaptic dysfunction. All together, these data suggest that RyRs may act as an amplification pathway for the Ca^{2+} pathology linked to neurodegenerative diseases, thought the exact mechanisms are still poorly understood.

4. Aim of the project

Neuronal plasticity shapes brain circuitries, with implications in cognition and behavior. Dendritic spines are dynamic structures that are subjected to substantial remodelling upon a variety of different stimuli. In excitatory glutamatergic neurons, local Ca^{2+} transients are triggered by ionotropic receptors. NMDAR activity leads to cytosolic influx of extracellular Ca^{2+} and the consequent elicit of local signaling cascades. Neuronal structure and function are modulated as a consequence of these local activations, which may lead to the formation of *de novo* spines. Despite decades of research, the importance of the contribution of CICR in plastic remodeling of dendritic spines, and its involvement in cognition, is still not clear.

The submitted thesis aims to unravel the relevance of RyR2-dependent Ca^{2+} signaling in the maintenance and remodeling of dendritic spines. To do so, (1) dendritic spines were measured in control and RyR2 knockdown primary hippocampal neurons; (2) an array of tissue-specific RyR2 knockout mice were generated; (3) spine density and morphology were characterized in the hippocampus throughout the generated models; (4) transgenic mice were subjected to three paradigms of synaptic plasticity to measure activity-evoked remodeling of dendritic spines.

Our novel findings demonstrate that genetic ablation of RyR2 causes cell shrinkage and regression of dendritic spines in CA1 cells. Lack of RyR2 particularly affects mushroom spines, leading to their regression to less mature stubby structures. Remarkably, neuronal RyR2 knockout suppresses experience-evoked spine remodeling in various brain areas and in different paradigms of synaptic plasticity. Together, these data demonstrate a significant contribution of RyR2 to dendritic spine homeostasis, which critically impacts hippocampal spatial memory acquisition.

5. Results

5.1 RyR2 mediates activity-dependent spinogenesis in primary hippocampal neurons.

A consistent body of literature indicates that RyRs mediate dendritic spine remodeling *in vitro* in cultured hippocampal neurons (Adasme et al., 2011; Korkotian and Segal, 1999; Kovalchuk et al., 2000; More et al., 2018; Ohashi et al., 2014). To dissect the distinct processes underlying RyR2-dependent neuronal plasticity, we initially tested the effect of the irreversible antagonist ryanodine (Rya) on dendritic spine maintenance. Primary hippocampal rat neurons at *day in vitro* (DIV) 8 were transfected with a vector encoding GFP and then treated with 50 μM Rya or DMSO (control) at DIV 14 (Figure 5.1A-E). One-hour treatment with Rya did not affect the dendritic complexity of primary cells (Figure 5.1B, RM Two-way Anova; Interaction F (55, 1815) = 1.662, p=0.0018; radius F (55, 1815) = 147, p<0.0001; treatment F (1, 33) = 1.621, p=0.211), although it did alter neuronal size (Figure 5.1C; unpaired t-test, p=0.0089). In line with previously published studies (Adasme et al., 2011; Korkotian and Segal, 1999), Rya treatment resulted in a reduced number of dendritic spines (Figure 5.1D-E, Table 6.1). Together, these data suggest the involvement of RyRs in the stability of neuronal structure.

Next, we assessed the long-term effect of RyR2 downregulation in pyramidal cells (Figure 5.1F-L). Neuronal cells were transfected at DIV 8 with vectors encoding GFP as well as either a scramble (scramble) or a short-hairpin RNA against *Ryr2* (sh-RyR2). Compared to the scramble vector, short hairpin RNA against *Ryr2* led to a significant downregulation of the RyR2 protein (Figure 5.1F). Neuronal arborization was measured at DIV 10 and DIV 14 as measured by Sholl analysis (Figure 5.1G). Compared to scramble-transfected cells, RyR2 deficient cells exhibited a decreased neuronal complexity at DIV 10 and DIV 14 (Figure 5.1H; DIV 10 RM Two-way Anova; Interaction F (150, 5587) = 1.723, p<0.0001; radius F (150, 5587) = 35.02, p<0.0001; genotype F (1, 5587) = 789.5, p<0.0001; DIV 14 Interaction F (151, 3496) = 2.082, p<0.0001; radius F (151, 3496) = 41.72, p<0.0001; genotype F (1, 3496) = 1032, p<0.0001). Together, this set of data suggests that RyR2 promotes the maintenance and complexity of dendritic arbors.

As a further step, we assessed the involvement of RyR2 in the maintenance and the activity-dependent remodeling of dendritic spines. DIV 14 transfected cells were compared at resting condition and under chemical LTP (cLTP), induced by a combination of inhibitors and activators (*i.e.*, forskolin, picrotoxin and rolipram, see "Materials and Methods") that stimulate Ca^{2+} influx (Figure 5.1I) (Oh et al., 2006; Otmakhov et al., 2004). At resting conditions, RyR2 deficient neurons showed a decreased number of spines compared to scramble GFP transfected cells (Figure 5.1J-K, Table 6.1). Consistent with previous results (Dinamarca et al., 2016), cLTP induced spine biogenesis in control cells, which did not occur in RyR2 knockdown ones (Figure 5.1K). Furthermore, we assessed the maturation status of dendritic spines. Spine morphology was classified accordingly to their shape as mushroom, thin and stubby (Figure 5.1L)(Lippi et al., 2011). At resting conditions, RyR2 deficient neurons showed a decreased percentage of mushroom spines compared to scramble cells (-12.61 %) (Figure 5.1L, Table 7.1), whereas stubby spines were significantly reduced in RyR2 knockdown cells (-10.75 %) (Figure 5.1L, Table 6.1). Scramble as well as RyR2 knockdown neurons exhibited an increased percentage of mushroom spines after cLTP induction (scramble: +9.54 %, sh-RyR2: +8.7 %) (Figure 5.1L, Table 6.1). Notably, decreased RyR2 content and/or cLTP did not affected the proportion of thin spines. Taken together, our data support the involvement of RyR2 in the homeostasis of dendric spines. Moreover, RyR2 is required for the stability of already existing mature spines and for activity-dependent spine biogenesis, but is dispensable for spine maturation.

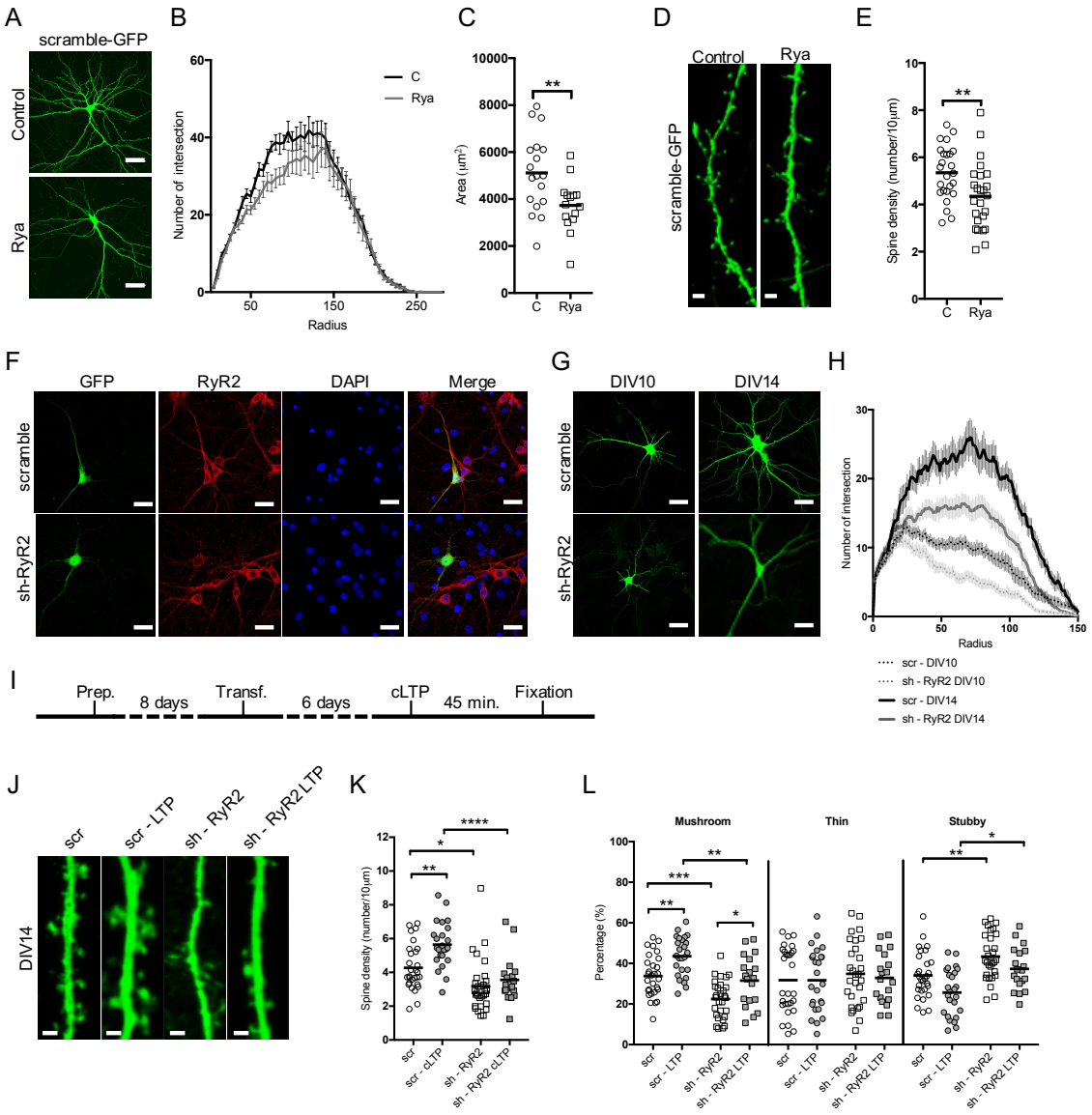

Figure 5.1. RyR2 mediates activity-dependent spinogenesis in primary hippocampal neurons. (A) Representative images of DIV14 primary hippocampal neurons transfected with scramble vector. Scale bar: 50 µm (B) Sholl analysis of 2D reconstructed pyramidal neurons using concentric spheres centered at the cell body of control and Rya-treated neurons (n=3; C: n=16 cells, Rya: n=16 cells). (C) Neuronal area of DIV14 control and Rya-treated neurons transfected with scramble vector (n=3; C: n=18 cells, Rya: n=15 cells). (D) Representative images of dendritic spines from control and Rya-treated DIV 14 primary hippocampal neurons transfected with scramble vector. Scale bar: 5 µm. (E) Quantification of spine density from GFP-positive control and Rya-treated neurons (n=3; C: n=25 cells, Rya: n=25 cells). (F) Representative images of DIV 14 primary hippocampal neurons transfected with scramble or sh-RyR2. Scale bar: 50 µm. (G) Representative picture of DIV10 and DIV14 scramble and sh-RyR2 transfected neurons. Scale bar: 50 µm. (H) Sholl analysis of pyramidal neurons of control and RyR2 knockdown neurons (n=3, DIV10 scramble:

n=21 cells, DIV10 sh-RyR2: n=15 cells, DIV14 scramble: n=11 cells, DIV14 sh-RyR2: n=14 cells). (I) Diagram of the experimental setup for the measurement of dendritic spines at rest and upon cLTP induction. (J) Representative pictures of dendritic spines from scramble (scr), scramble with cLTP (scr cLTP), short hairpin-RyR2 (sh-RyR2) and short hairpin-RyR2 with cLTP (sh-RyR2 cLTP) neurons. Scale bar: 2 μm (K) Quantification of dendritic spines from scr, scr cLTP, sh-RyR2 and sh-RyR2 cLTP neurons (n=3, scr: n=29 cells, scr cLTP n=24 cells, sh-RyR2: n=30 cells, sh-RyR2-cLTP: n=19 cells). (L) Spine classification in scr, scr cLTP, sh-RyR2 and sh-RyR2 cLTP neurons (n=3, scramble: n=29 cells, scramble cLTP n=24 cells, sh-RyR2: n=30 cells, sh-RyR2-cLTP: n=19 cells). Data are reported as mean ± SEM; student's *t* test or Two-way ANOVA or RM two-way ANOVA with Bonferroni post hoc comparison, ****$p<0.0001$, ***$p<0.001$, **$p<0.01$, *$p<0.05$. Statistical analyses for spine densities are reported in Table 6.1.

5.2 Generation and validation of conditional *Ryr2* knockout mice.

To study the relevance of RyR2 in the brain, we used transgenic mice carrying floxed *Ryr2* alleles generated by ingenious Targeting Laboratory (iTL) (Figure 5.2A). *Ryr2* floxed mice were bred with a line ubiquitously expressing the bacterial Cre-recombinase (*CMV-Cre*$^{tg/wt}$). Genetic recombination of l*oxP* sites flanking exon 8 produced a premature stop codon that abrogated *Ryr2* expression, causing early embryonic lethality as previously reported (Figure 5.2B) (Takeshima et al., 1998). This suggests that Cre-mediated recombination of our floxed alleles results in RyR2 KO. To overcome embryonic lethality and obtain conditional *Ryr2* knockout mice, *Ryr2*$^{fl/fl}$ males were crossed with females expressing Cre-recombinase under cell-type specific promoters (*Nestin*, *Synapsin* and *Camk2α*). The *Nestin-Cre* strain was used to drive the deletion of *Ryr2* in the entire central and peripheral nervous system starting from embryonic day 11 (E11) (Tronche et al., 1999). *Synapsin I* promoter was used to delete the channel in neurons starting from embryonic day 12.5 (E12.5) (Zhu et al., 2001). *Camk2α-Cre T29-1* line was chosen to generate mice lacking RyR2 in the forebrain (predominantly in the CA1 neurons of the hippocampus) from postnatal day 19 (P19) (Tsien et al., 1996). The loss of RyR2 was confirmed by immunoblot analyses and quantitative RT-PCR of brain tissue from 4 month-old *Nestin-Cre;Ryr2*$^{fl/fl}$ mice (Figure 5.2C, unpaired t-test, $p<0.0001$) and *Synapsin-Cre;Ryr2*$^{fl/fl}$ mice (Figure 5.2D, unpaired t-test, $p=0.033$). *In situ* hybridization in brain tissue confirmed that *Ryr2* mRNA levels were significantly reduced in all our *Ryr2* knockout models (Figure 5.2E).

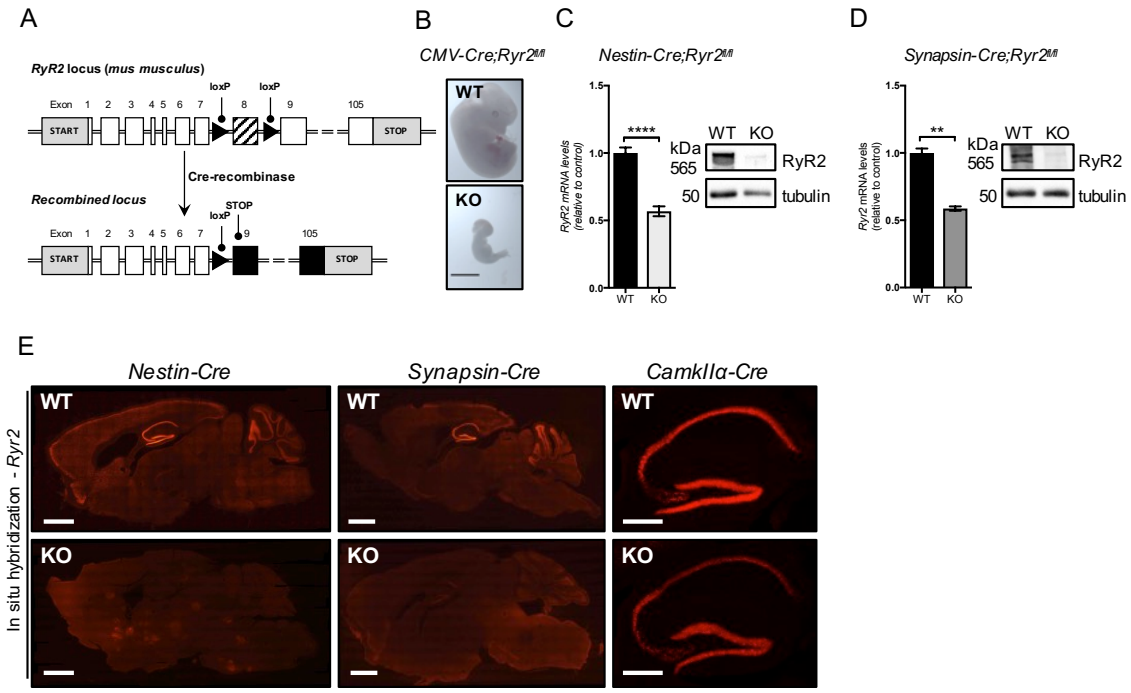

Figure 5.2 Generation and validation of RyR2 knockout mice. (A) Schematic representation of the genetic targeting strategy. Recombination of the two-*lox*P sites flanking exon 8 in *Ryr2* knockout. (B) Ubiquitous deletion of *Ryr2* (*CMV-Cre*$^{tg/wt}$) and the consequent embryonic lethality at E12.5. Scale bar: 1 mm. (C-D) qRT-PCR and western blot for RyR2 in brain homogenates from controls, (C) *Nestin-Cre*$^{tg/wt}$*;Ryr2*$^{fl/fl}$ (n=3) and (D) *Synapsin-Cre*$^{tg/wt}$*;Ryr2*$^{fl/fl}$ mice (n=3). (E) In situ hybridization for *Ryr2* in sagittal brain sections from control and *Nestin-Cre*$^{tg/wt}$, *Synapsin-Cre*$^{tg/wt}$ (Scale bar: 1 mm) and *Camk2α-Cre*$^{tg/wt}$*;Ryr2*$^{fl/fl}$ mice (Scale bar: 400 μm). qRT-PCR values rappresented in relative expression. Mean ± SEM. Student's *t* test, ****p<0.0001, **p<0.01).

5.3 Genetic deletion of *Ryr2* affects motor coordination associated with decreased spine density in cerebellar Purkinje cells.

Our first aim was to study the possible implication of RyR2 in hippocampal-dependent learning and memory. *Nestin-Cre*$^{tg/wt}$ animals were excluded since this line exhibits a strong impairment in the acquisition of both contextual- and cued- conditioned fear, affecting cognitive tests (Giusti et al., 2014). Thus, we started to characterize *Syn-Cre*$^{tg/wt}$*;Ryr2*$^{fl/fl}$ mice and found no major anatomical differences in brains from 6 month-old animals (Figure 5.3A). However, RyR2 knockout animals displayed decreased locomotor activity (Figure 5.3B, Table 6.2) and reduced movement velocity (Figure 5.3C, Table 6.2) compared to control mice. Furthermore, neuron-specific *Ryr2* knockout mice showed

persistent motor coordination impairments in the rotarod test, as they did not improve their performance over the three days of trial (Figure 5.3D, Table 6.2). To study hippocampus-related cognition, we performed the Morris water maze (MWM) test and observed that *Syn-Cre$^{tg/wt}$;Ryr2$^{fl/fl}$* mice were unable to swim properly during training trials, with a reduced swim speed (Figure 5.3E, Table 6.2) and a pronounced tendency of floating behavior (Figure 5.3F, Table 6.2). This swimming impairment compromised the interpretation of the data, since we could not address any cognitive aspects in *Syn-Cre$^{tg/wt}$;Ryr2$^{fl/fl}$* mice. We also tried to perform alternative spatial learning and memory tests, but all were similarly influenced by the altered motor function. Given the impaired performance of *Syn-Cre$^{tg/wt}$;Ryr2$^{fl/fl}$* mice, we studied cerebellum neuroanatomy, as the cerebellum is functionally linked to motor coordination in mammals. Cerebellar size, foliation and lamination of *Syn-Cre$^{tg/wt}$;Ryr2$^{fl/fl}$* mice were comparable to control littermates (Figure 5.3G). Immunostaining of Purkinje cells did not reveal any major alteration in their alignment or number in *Syn-Cre$^{tg/wt}$;Ryr2$^{fl/fl}$* compared to control mice (Figure 5.3H). We measured the dendritic arbor of Golgi-stained Purkinje cells by Sholl analysis and observed no obvious alterations in their complexity (Figure 5.3I). However, spine density of secondary dendrites was significantly reduced in Purkinje cells of *Syn-Cre$^{tg/wt}$;Ryr2$^{fl/fl}$* compared to control mice (Figure 5.3J, Table 6.1). Together, these findings support an altered homeostasis of dendritic spines in Purkinje cells lacking RyR2, which might contribute to the locomotor defect observed in the aforementioned behavioral tests.

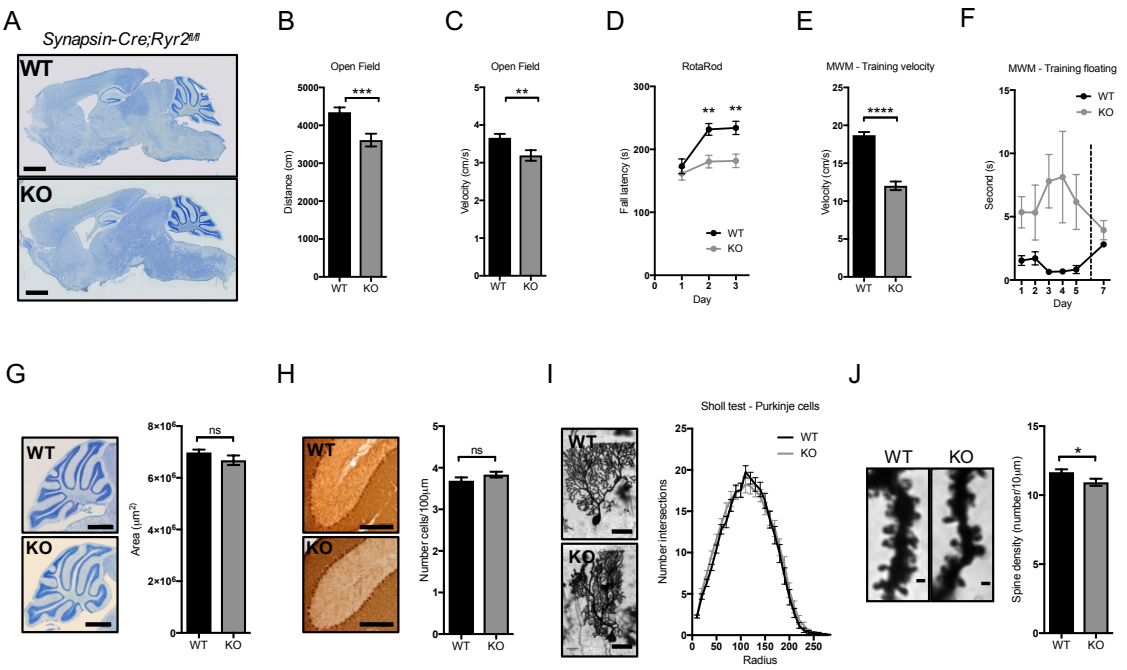

Figure 5.3 RyR2 contributes to motor coordination and spine maintenance in Purkinje cells. (A) Nissl staining in sagittal brain sections of control and *Synapsin-Cre*$^{tg/wt}$*; Ryr2*$^{fl/fl}$ mice. Scale bar: 1 mm. (B) Travelled distance measured in the open field of control and *Synapsin-Cre*$^{tg/wt}$*; Ryr2*$^{fl/fl}$ mice (WT: n=31, KO: n=30). (C) Mean velocity measured in the open field of control and *Synapsin-Cre*$^{tg/wt}$*; Ryr2*$^{fl/fl}$ mice (WT: n=31, KO: n=30). (D) Fall latencies was measured in the rotarod test comparing control and *Synapsin-Cre*$^{tg/wt}$*;Ryr2*$^{fl/fl}$ mice (WT: n=32, KO: n=30). (E) Swim speed and (F) floating time during training in the MWM of control and *Synapsin-Cre*$^{tg/wt}$ mice (WT: n=12, KO: n=7). (G) Nissl staining in sagittal brain sections and quantification of the cerebellar size in control and *Synapsin-Cre*$^{tg/wt}$*; Ryr2*$^{fl/fl}$ mice (WT: n=5, KO: n=5). Scale bar: 1 mm. (H) DAB immunohistochemistry of calbindin-labeled Purkinje cells in sagittal brain sections in control and *Synapsin-Cre*$^{tg/wt}$*; Ryr2*$^{fl/fl}$ mice (WT: n=3, KO: n=3). Scale bar 500 µm. (I) Sholl analysis of the dendritic arbor of Golgi-stained Purkinje cells from control and *Synapsin-Cre*$^{tg/wt}$*; Ryr2*$^{fl/fl}$ mice (WT: n=43 cells/ mice n=7, KO: n=49 cells/ mice n=6). Scale bar: 60 µm. (J) Spine density of secondary dendrites of Golgi-stained Purkinje cells in *Synapsin-Cre*$^{tg/wt}$*; Ryr2*$^{fl/fl}$ compared to control mice (WT: n=70 cells/ mice n=7, KO: n=65 cells/ mice n=6). Scale bar: 1 µm. Data are reported as mean ± SEM. Unpaired Student's *t* test or Two-way ANOVA or RM two-way ANOVA with Bonferroni post hoc comparison, ****p<0.0001, ***p<0.001, **p<0.01, *p<0.05. Statistical analyses for spine densities and behavioral tests are reported in Table 6.1 and 6.2, respectively.

5.4 Genetic deletion of *Ryr2* impairs spine maintenance in the hippocampus.

Based on our *in vitro* and *in vivo* findings, we reasoned that genetic manipulation of *Ryr2* would impact the spine maintenance in the hippocampus (Figure 5.4A). Initially,

we assessed for possible compensatory mechanisms of other channels involved in the Ca^{2+} homeostasis. We performed qRT-PCR and assessed the expression levels of *Ryr1*, *Ryr3*, *Ip3R1*, *Ip3R2*, *Ip3R3*, *SERCA1*, *SERCA2*, $Ca_v1.2$ and $Ca_v1.3$. Genetic deletion of *Ryr2* in the hippocampus did not trigger any major compensatory expression changes of other Ca^{2+} transporters, apart from a moderate *Ryr3* up-regulation (Figure 5.4B, unpaired *t*-test, *Ryr2* $p<0.0001$; *Ryr3* $p=0.0453$). We then quantified dendritic spines in the hippocampus of *Synapsin-Cre*$^{tg/wt}$*;Ryr2*$^{fl/fl}$ mice and found that, compared to control littermates, spine density was significantly reduced in the basal dendrites of CA1 and CA3 pyramidal neurons (Figure 5.4C-D). We did not find any difference in spine content of apical dendrites of CA1 and CA3 pyramidal neurons or in the granule cells of the dentate gyrus (DG) (Figure 5.4C-D, Table 6.1). These data confirm that RyR2 contributes to the maintenance of dendritic spines in the CA1 and CA3 region of the hippocampus.

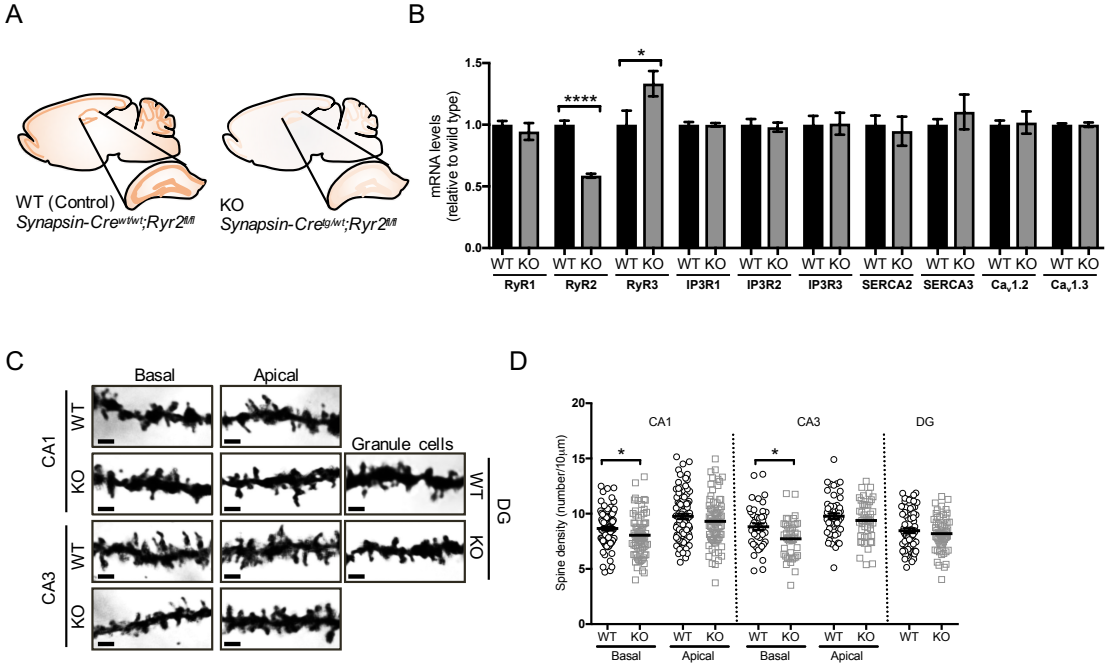

Figure 5.4 Deletion of *Ryr2* impairs spine maintenance in the CA1 and CA3 of the hippocampus. (A) Representative scheme of control and *Synapsin-Cre*$^{tg/wt}$*; Ryr2*$^{fl/fl}$ mice. (B) qRT-PCR analysis of channels involved in calcium homeostasis from dissected hippocampal samples in control and *Synapsin-Cre*$^{tg/wt}$*;Ryr2*$^{fl/fl}$ mice (WT: n=3, KO: n=3). (C-D) Spine density of secondary basal and apical dendrites was measured in Golgi-stained CA1 (WT: n=82 cells/ mice n=7, KO: n=71 cells/ mice n=6), CA3 (WT: n=44 cells/ mice n=7,

KO: n=38 cells/ mice n=6) and DG (WT: n=75 cells/ mice n=7, KO: n=56 cells/ mice n=6) regions of the hippocampus comparing control and *Synapsin-Cre$^{tg/wt}$; Ryr2$^{fl/fl}$* mice. Scale bar: 2 µm. Data are reported as mean ± SEM. Unpaired Student's *t* test or Two-way ANOVA with Bonferroni post hoc comparison, ****p<0.0001, ***p<0.001, **p<0.01, *p<0.05. Statistical analyses for spine densities are reported in Table 6.1.

5.5 *Ryr2* deletion in adulthood causes neuronal shrinkage and loss of dendritic spines in CA1 neurons.

RyRs are implicated in the post-natal differentiation of neurons (Sukhareva et al., 2002; Yu et al., 2008). Since the genetic ablation of *Ryr2* in *Synapsin-Cre$^{tg/wt}$;Ryr2$^{fl/fl}$* mice occurs prenatally, we aimed to exclude the possible confounding effects of aberrant embryonic processes and/or compensatory mechanisms. Thus, we unilaterally injected either *rAAV5.CamK2α.GFP-cre* (KO) or *rAVV.CamK2αGFP* (WT) (as a control) in the CA1 region of the hippocampus of 5 month-old *Ryr2$^{fl/fl}$* mice (Figure 5.5A). Whole cell patch clamp recordings in acute sections were performed 4-6 weeks after viral injections. The intrinsic excitability was recorded in GFP-positive neurons (data not shown) followed by 3D reconstruction. After recording, CA1 neurons were filled with biocytin and stained with streptavidin (Figure 5.5A). *In situ* hybridization against *Ryr2* mRNA in hippocampal sections confirmed the effect of the viral strategy (Figure 5.5B). Sholl analysis of CA1 cells (Figure 5.5D; RM Two-way Anova; Interaction F (857, 27424) = 2.676, p<0.0001; radius F (857, 27424) = 47.73, p<0.0001; genotype F (1, 32) = 11.93, p=0.0016) and morphometric analyses (Table 6.3) revealed a significant decrease in dendritic length, diameter, branching, area and volume in the entire CA1 strata of *Ryr2* knockout cells. Basal dendrites of the stratum s. oriens were particularly affected with a significant reduction in all parameters measured, including length, diameter, area, volume and branch points (Table 6.3). Upon RyR2 loss, decreased area, volume and diameter was observed in apical dendrites, including radial oblique dendrites of the s. radiatum layer and the apical tuft dendrites protruding from the distal trunk into the s. lacunosum-moleculare (Table 6.3). Overall, *Ryr2* knockout neurons were ~30.7% shorter in length, ~30.6% smaller in area, ~31.1% smaller in volume and reduced by ~8.1% in diameter (Table 6.3). These changes imply cell shrinkage and a decreased complexity of the dendritic arbor.

To confirm the importance of RyR2 in the maintenance of postsynaptic compartments, we measured spine density and morphology in all the dendritic strata of the reconstructed pyramidal cells (Figure 5.5E-G). Spine density was significantly reduced in all dendrites of the stratum s. oriens, s. radiatum and s. lacunosum-moleculare of *Ryr2* knockout cells (Figure 5.5E-F and Table 6.4). Morphological classification of spines revealed a significantly altered maturational state of *Ryr2* knockout pyramidal cells (Figure 6.4G and Table 6.4). In dendrites of the s. oriens, *Ryr2* knockout cells showed less mushroom (-12.8%), more stubby (+14.2%) and an equal number of thin spines (Table 6.4). Similarly, dendrites of the s. lacunosum-moleculare layer displayed a decreased number of mature spines (Table 6.4; -9.1% mushroom; +11.5% stubby). In dendrites of the radial oblique, the proportions of the spine classes remained unchanged (Table 6.4). Compared to control cells, RyR2 knockout neurons exhibited a shorter spine neck (Table 6.4) in both basal dendrites of the s. oriens and apical dendrites of the s. lacunosum-molecolare (Table 6.4). Spine length in radial oblique dendrites was comparable to control cells (Table 6.4). This set of experiments confirms that RyR2 sustains spine stability, particularly that of mature spines, in adult neurons.

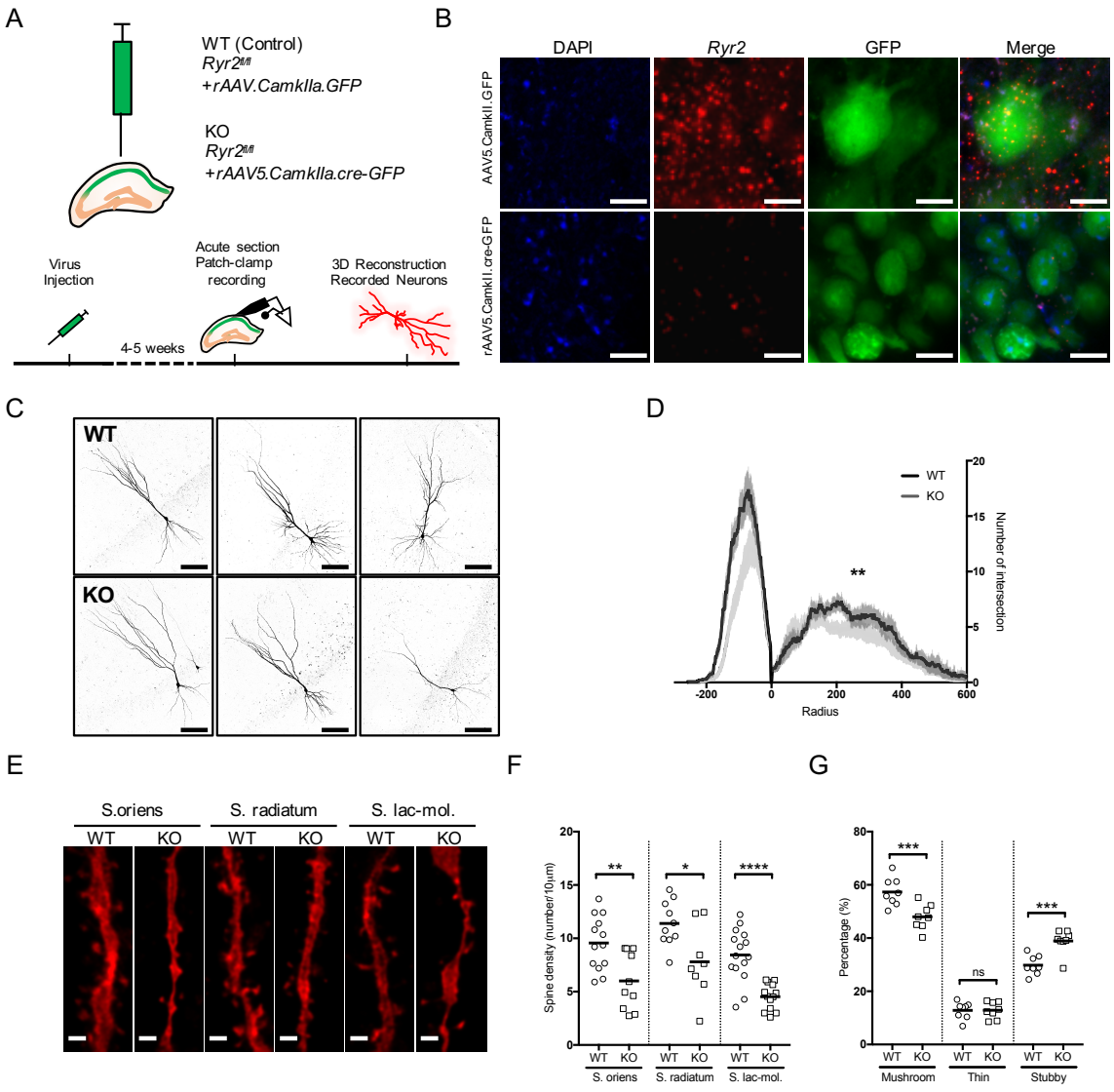

Figure 5.5 RyR2 deletion in adult CA1 neurons produces neuronal shrinkage and loss of dendritic spines. (A) Schematic representation of the experimental design. *Ryr2*$^{fl/fl}$ mice were stereotaxically injected with *rAAV.Camk2α-GFP*, as a control, or with *rAAV5.Camk2α.cre-GFP* to delete *Ryr2* in the CA1 of the hippocampus. Patch-clamp recordings were conducted in acute sections from mice after 4-6 weeks from the stereotaxic injection. The recorded neurons were filled with biocytin and stained with streptavidin for 3D reconstruction. (B) *In situ* hybridization of *Ryr2* in CA1 pyramidal cells showed the efficiency of the genetic deletion of the channel. Scale bar: 100 µm. (C) Representative reconstructions of patch-clamp recorded control (WT) and *Ryr2* knockout (KO) CA1 pyramidal neurons. Scale bar: 100 µm. (D) Sholl analysis of 3D reconstructed pyramidal neurons using concentric spheres centered at the cell body for control and *Ryr2* knockout neurons (WT: n=15 cells/ 9 mice; KO: 18 cells/ 11 mice). (E-G) Spine density and morphology were measured from the recorded pyramidal neurons in the dendrites of the stratum s. oriens (WT: n=13

cells/ 9 mice; KO: 10 cells/ 5 mice), s. radiatum (WT: n=10 cells/ 7 mice; KO: 8 cells/ 4 mice) and s. lacunosum-moleculare (WT: n=15 cells/ 9 mice; KO: 13 cells/ 6 mice). Scale bar: 1 μm. Data are reported as mean ± SEM. Unpaired Student's *t* test or Two-way ANOVA or RM two-way ANOVA with Bonferroni post hoc comparison, ****$p<0.0001$, ***$p<0.001$, **$p<0.01$, *$p<0.05$. Statistical analyses are reported in Table 6.3-6.4.

5.6 RyR2 contributes to hippocampal spatial learning and activity-dependent spine remodeling in CA1 neurons.

A consistent line of evidence supports that spatial learning increases dendritic spines in CA1 neurons, which is also associated with *Ryr2* up-regulation (Adasme et al., 2011; Maguire et al., 2000; Mori et al., 2000; Moser et al., 1994; Moser et al., 1997; Rusakov et al., 1997; Zhao et al., 2000). To confirm that RyR2 mediates the activity-evoked remodeling of dendritic spines *in vivo*, we subjected mice to the MWM. To this end, we trained 5 month-old control and the forebrain *Ryr2* deleted *Camk2α-Cre$^{tg/wt}$;Ryr2$^{fl/fl}$* mice. Postnatal (*i.e.*, around P17.5) loss of RyR2 did not result in major anatomical alterations of the hippocampus (Figure 5.6A) and did not alter locomotor activity nor motor coordination (Figure 5.6B-C, Table 6.2), as observed in *Synapsin-Cre$^{tg/wt}$;Ryr2$^{fl/fl}$* mice. Control and *Camk2α-Cre$^{tg/wt}$;Ryr2$^{fl/fl}$* mice were trained in the MWM over five consecutive days (Figure 5.6D, Table 6.2). Swim distances (data not shown) and escape latencies gradually decreased, as indexed by a significant main effect of day (Figure 5.6E, Table 6.2). Compared to control mice, *Camk2α-Cre$^{tg/wt}$;Ryr2$^{fl/fl}$* animals showed a reduced improvement in performance during the initial training trials, which resulted in a higher escape latency on day 3 of training (Figure 5.6E, Table 6.2). In contrast, *Camk2α-Cre$^{tg/wt}$;Ryr2$^{fl/fl}$* mice performed similar to control littermates by the last day of training. Short-term memory was assessed by removing the platform from the maze at day 3, 90 minutes after the training trials. The time the mice spent in the target quadrant (quadrant occupancy) was compared to the time spent in the non-target quadrants (*i.e.* right, opposite, left). Unlike control mice, *Camk2α-Cre$^{tg/wt}$;Ryr2$^{fl/fl}$* mice failed to remember the platform location (Figure 5.6F, Table 6.2). However, *Camk2α-Cre$^{tg/wt}$;Ryr2$^{fl/fl}$* mice performed as well as control mice during the long-term memory probe trial performed 24 hours after the last training session (Figure 5.6G, Table 6.2). Based on these results, animals lacking *Ryr2* in

the forebrain exhibited a reduced capacity to acquire memories, but they still displayed normal long-term memory (Galeotti et al., 2008; Liu et al., 2012; More et al., 2018; Zhao et al., 2000).

To demonstrate that RyR2 is the driving force for activity-induced spine formation, a cohort of trained control and *Camk2α-Cre*$^{tg/wt}$*;Ryr2*$^{fl/fl}$ mice was sacrificed 24 hours after the long-term memory test and compared to a cohort of naïve control and *Camk2α-Cre*$^{tg/wt}$*;Ryr2*$^{fl/fl}$ animals. As previously described, we confirmed that spatial training produced a hippocampal-specific *Ryr2* up-regulation (Figure 5.6H, unpaired Student's *t* test, p =0.0085)(Adasme et al., 2011). Dendritic spines of CA1 pyramidal cells were Golgi-stained in naïve and trained control and *Camk2α-Cre*$^{tg/wt}$*;Ryr2*$^{fl/fl}$ mice. In control mice, MWM training produced a significant increase of spine density in apical dendrites (Figure 5.6I-J, Table 6.1), but not in basal ones (Figure 5.6K-L, Table 6.1). Naïve *Camk2α-Cre*$^{tg/wt}$*;Ryr2*$^{fl/fl}$ mice exhibited significantly fewer spines in basal dendrites compared to naïve control littermates (Figure 5.6K-L, Table 6.1), whereas they showed the same spine density in apical dendrites (Figure 5.6I-J, Table 6.1). *Camk2α Cre*$^{tg/wt}$*; Ryr2*$^{fl/fl}$ mice did not exhibit changes in spine density either on apical (Figure 5.6I-J) or basal dendrites (Figure 5.6K-L) upon MWM training. These findings demonstrate that RyR2 is an important regulator of activity-evoked spine plasticity associated with spatial acquisition of memories.

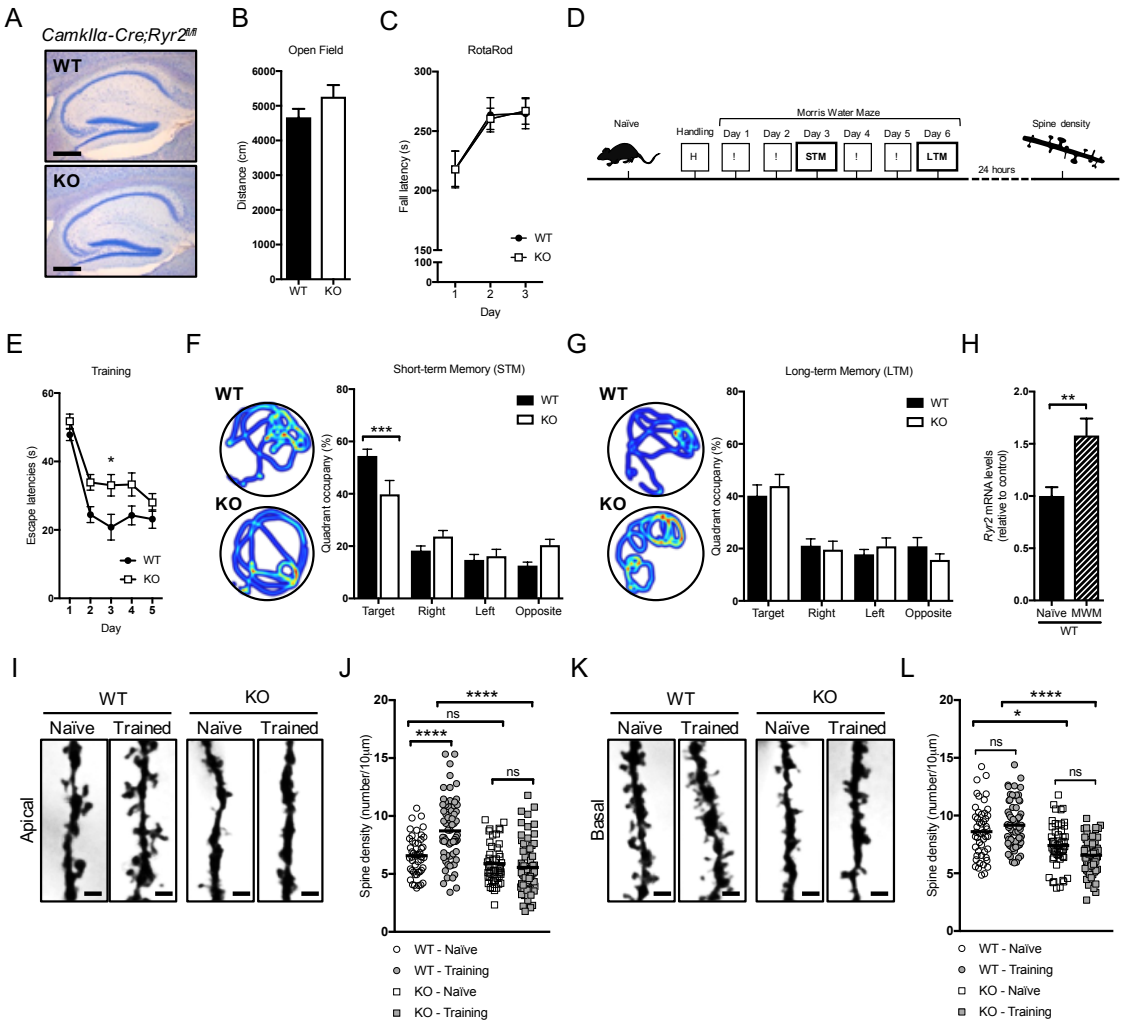

Figure 5.6 RyR2 contributes to hippocampal spatial learning and activity-dependent spine remodeling in CA1 neurons. (A) Nissl staining in sagittal hippocampal sections from control and *Camk2α-Cre*$^{tg/wt}$*;Ryr2*$^{fl/fl}$. Scale bar: 400 µm. (B) Distance run in open field test of control and *Camk2α-Cre*$^{tg/wt}$*;Ryr2*$^{fl/fl}$ mice (WT: n=20, KO: n=19). (C) Fall latency of control and *Camk2α-Cre*$^{tg/wt}$*;Ryr2*$^{fl/fl}$ mice in rotarod test (WT: n=15, KO: n=16). (D) Diagram of the experimental timeline for MWM test. Control and *Camk2α-Cre*$^{tg/wt}$*;Ryr2*$^{fl/fl}$ mice were subjected to spatial training over 5 days. Short-term memory (STM) was assess 90 minutes after the training session at day 3. Long-term memory (LTM) was tested twenty-four hours after the last day of training at day 6. Twenty-four hours after the long-term memory test, mice were sacrificed and Golgi staining was performed on brains for morphometrical quantification of dendritic spines. (E) Escape latencies of control and *Camk2α-Cre*$^{tg/wt}$*;Ryr2*$^{fl/fl}$ mice over the 5 days of training (WT: n=13, KO: n=18). (F) Short-term memory was tested in control and *Camk2α-Cre*$^{tg/wt}$*;Ryr2*$^{fl/fl}$ mice quantifying the target quadrant occupancy at day 3 (WT: n=13, KO: n=18). (G) Long-term memory was tested in control *Camk2α-Cre*$^{tg/wt}$*;Ryr2*$^{fl/fl}$ mice measuring the target quadrant occupancy 24 h after the last training at day 6 (WT: n=13, KO: n=18). (H) qRT-PCR for *Ryr2* from

hippocampal samples of control naïve and MWM-trained mice (WT: n=6, KO: n=4). (I-L) Quantifications of spine density in the apical (I-J) (WT naïve: n=47 cells/ 5 mice , WT trained: n=69 cells/ 7 mice, KO naïve: n=48 cells/ 5 mice, KO trained: n=66 cells/ 7 mice) and basal (K-L) (WT naïve: n=48 cells/ 5 mice , WT trained: n=66 cells/ 7 mice, KO naïve: n=50 cells/ 5 mice, KO trained: n=67 cells/ 7 mice) dendrites of CA1 neurons in naïve and MWM-trained control and *Camk2α-Cre$^{tg/wt}$;Ryr2$^{fl/fl}$*mice. Scale bar: 2 μm. Data are reported as mean ± SEM. Unpaired Student's *t* test, Two-way ANOVA or RM two-way ANOVA with Bonferroni post hoc comparison, ****p<0.0001, ***p<0.001, **p<0.01, *p<0.05. Statistical analyses for spine densities and behavioral tests are reported in Table 6.1 and 6.2, respectively.

5.7 RyR2 contributes to drug-induced context-associated memory and activity-dependent spine remodeling in CA1 neurons.

Next, we aimed to confirm that RyR2 is a mediator of spine remodeling and memory acquisition with a second test that implies the reinforcing effect of psychoactive drugs. Cocaine was used as a stimulus to trigger spinogenesis and *Ryr2* upregulation in the hippocampus of rodents (Kurokawa et al., 2011; Ziviani et al., 2011). *Camk2α-Cre$^{tg/wt}$;Ryr2$^{fl/fl}$* and *Camk2α-Cre$^{wt/wt}$;Ryr2$^{fl/fl}$* mice were tested in drug-induced conditioned place preference (CPP), which is a test that employs associative learning, spatial and contextual memory (O'Keefe, 1976; O'Keefe and Dostrovsky, 1971; O'Keefe and Speakman, 1987; Phillips and LeDoux, 1994; White and Carr, 1985)(Figure 5.7A). Mice were conditioned to associate the rewarding properties of cocaine with a distinct cocaine-paired context in comparison to a distinct saline-paired context (Figure 5.7B). *Camk2α-Cre$^{tg/wt}$;Ryr2$^{fl/fl}$* and control mice were alternately injected with either saline or cocaine (20 mg/kg) over 6 days of conditioning (Figure 5.7C). Cocaine-associated memory was tested 24 h after the last saline injection at day 8 (post-conditioning). In the pre-conditioning test, neither control nor *Camk2α-Cre$^{tg/wt}$; Ryr2$^{fl/fl}$* mice showed an initial preference for either the black or white chamber of the CPP apparatus. Instead, the conditioning phase led control mice to a significant preference for the cocaine-paired chamber, while *Camk2α-Cre$^{tg/wt}$; Ryr2$^{fl/fl}$* mice showed a lower CPP score, suggesting impaired cocaine-associated memory formation (Figure 5.7D-E, Table 6.2). Cocaine administration in control mice resulted in the specific up-regulation of *Ryr2* in the hippocampus (Figure 5.7F, unpaired Student's *t* test, p =0.0102), as previously reported (Ziviani et al., 2011). Control and *Camk2α-Cre$^{tg/wt}$; Ryr2$^{fl/fl}$* mice were sacrificed 24 hours after the CPP test and brains were impregnated with Golgi

staining. In comparison with saline-injected control littermates, control cocaine-treated mice exhibited an increased spine density in the apical region (Figure 5.7G-H, Table 6.1), but not in the basal dendrites (Figure 5.7I-J, Table 6.1). Instead, saline- and cocaine-treated *Camk2α-Cre*$^{tg/wt}$*;Ryr2*$^{fl/fl}$ mice did not show changes in spine density in both apical and basal dendrites (Figure 5.7G-J, Table 6.1). Altogether, these findings demonstrate the key contribution of RyR2 in hippocampal-dependent cocaine-associated memory formation and dendritic spine remodeling of CA1 cells.

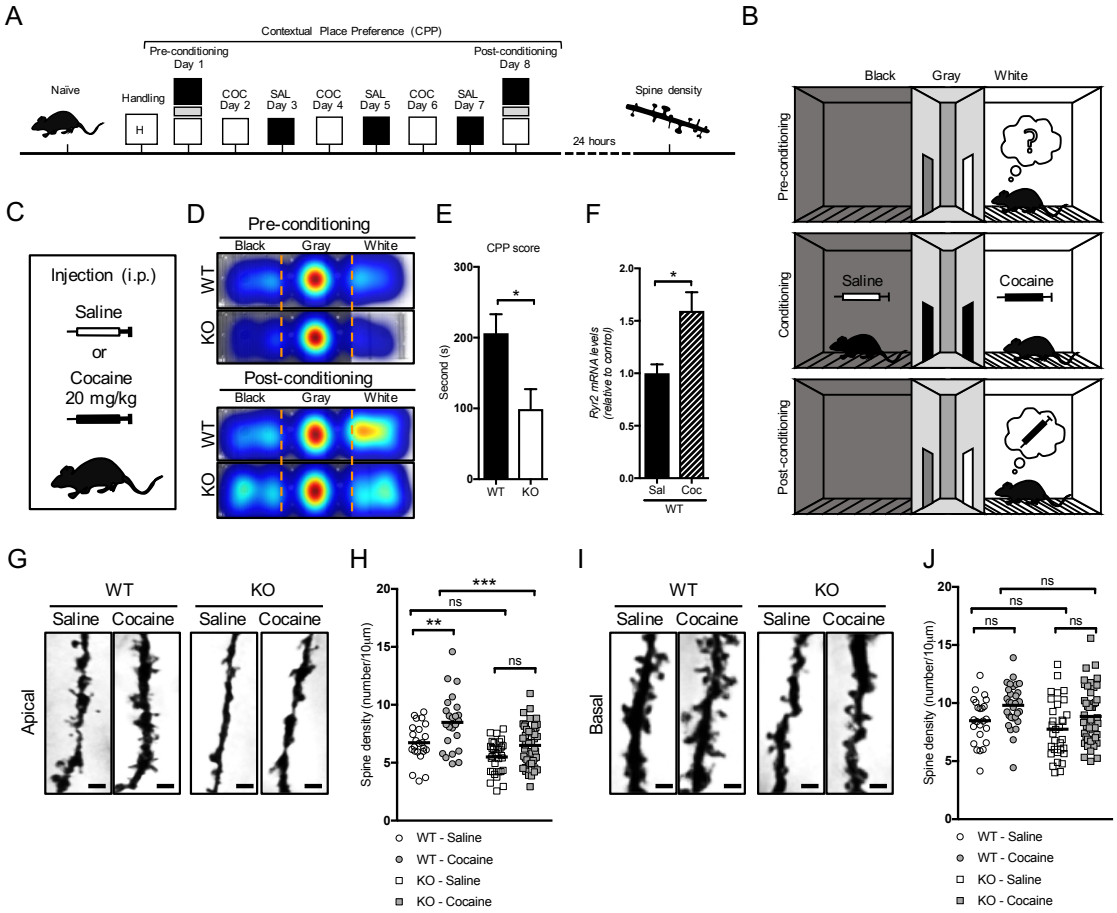

Figure 5.7 RyR2 contributes to hippocampal drug-induced context-associated memory and activity-dependent spine remodeling in CA1 neurons. (A) Schematic representation of the cocaine-induced conditioned place preference (CPP) test. (B-C) *Camk2α-Cre*$^{tg/wt}$*;Ryr2*$^{fl/fl}$ and control mice were intraperitoneally injected (i.p.) every other day with either cocaine (20 mg/kg) or saline solution for a total of 6 days. Cocaine-associated memory was tested on day 8, 24h after the last saline injection. (D) Heatmaps depict the development of spatial preference before (pre-conditioning) and after (post-conditioning) cocaine administration in control and *Camk2α Cre*$^{tg/wt}$*;Ryr2*$^{fl/fl}$ mice. (E) Contextual place preference score of cocaine-treated control and *Camk2α Cre*$^{tg/wt}$*;Ryr2*$^{fl/fl}$ mice (WT cocaine: n=8, KO cocaine: n=8). (F) qRT-PCR of *Ryr2*

mRNA expression of hippocampal samples from cocaine- and saline-treated control mice (WT saline: n=6, WT cocaine: n=3). (G-J) Golgi-stained spines were counted in the apical (G-H) (WT naïve: n=23 cells/ 3 mice , WT cocaine: n=24 cells/ 4 mice, KO naïve: n=32 cells/ 4 mice, KO cocaine: n=47 cells/ 6 mice) and basal (I-J) (WT naïve: n=24 cells/ 3 mice , WT cocaine: n=31 cells/ 4 mice, KO naïve: n=32 cells/ 4 mice, KO cocaine: n=48 cells/ 6 mice) dendrites of CA1 neurons, comparing cocaine-treated and saline-treated control and *Camk2α-Cre*$^{tg/wt}$*;Ryr2*$^{fl/fl}$ mice. Scale bar: 2 μm. Data are reported as mean ± SEM. Unpaired Student's *t* test or Two-way ANOVA with Bonferroni post hoc comparison, ****p<0.0001, ***p<0.001, **p<0.01, *p<0.05. Statistical analyses for spine densities and behavioral tests are reported in Table 6.1 and 6.2, respectively.

5.8 Nicotine-dependent spine remodeling in the mesolimbic pathway requires RyR2.

To confirm that RyR2 is a common denominator of experience-driven spine remodeling in different neuronal subtypes and regions of the brain, we administered nicotine as an alternative paradigm of drug-evoked neuronal plasticity (Brown and Kolb, 2001; Kang et al., 2015). Control and *Nestin-Cre*$^{tg/wt}$*;Ryr2*$^{fl/fl}$ were injected daily (i.p.) with either saline or 0.5 mg/kg of nicotine over 7 consecutive days (Figure 5.8A-B). In line with previously published data, control mice treated with nicotine led to a significant *Ryr2* upregulation in the pre-frontal cortex (PfCx)(Figure 5.8C-D, unpaired Student's *t* test, p =0.0202) and in the nucleus accumbens (NAc)(Figure 5.8G-H, unpaired Student's *t* test, p =0.0016) but not in the hippocampus (Hip)(Figure 5.8K) (Ziviani et al., 2011). 24h after the last nicotine injection, spine density was measured in saline- and nicotine-treated control and *Nestin-Cre*$^{tg/wt}$*;Ryr2*$^{fl/fl}$ mice. First, we assessed the distal projections of pyramidal neurons of the medial PfCx (Figure 5.8E-F). In control mice, chronic nicotine treatment induced an increased number of spines in apical dendrites (Figure 5.8E-F, Table 6.1). Conversely, nicotine-treated *Nestin-Cre*$^{tg/wt}$*;Ryr2*$^{fl/fl}$ mice did not exhibit any change in their spine content compared to saline-injected RyR2 knockout mice (Figure 5.8E-F, Table 6.1). We detected a significant decrease of spine density between saline-injected control and *Nestin-Cre*$^{tg/wt}$*;Ryr2*$^{fl/fl}$ mice (Figure 5.8E-F, Table 6.1). Secondly, we compared the spine density in secondary dendrites of GABAergic medium spiny neurons (MSNs) in the shell of the NAc of saline and nicotine-treated mice (Figure 5.8I-J, Table 6.1). MSNs neurons showed a lower spine density in saline-treated *Nestin-Cre*$^{tg/wt}$*;Ryr2*$^{fl/fl}$ mice compared to

saline-treated control littermates (Figure 5.8I-J, Table 6.1). Consistent with our previous results, nicotine treated *Nestin-Cre*$^{tg/wt}$*;Ryr2*$^{fl/fl}$ mice displayed no significant alteration of spine density compared to untreated RyR2 knockout mice, whereas control mice did produce plastic remodeling of spines in MSNs (Figure 5.8I-J, Table 6.1). Notably, in the hippocampus control and *Nestin-Cre*$^{tg/wt}$*;Ryr2*$^{fl/fl}$ mice did not show increased spine density after the treatment, both at the basal and apical levels of CA1 neurons (Figure 5.8L-O, Table 6.1). These data imply that RyR2 mediates nicotine-induced spine plasticity of the mesolimbic and mesocortical circuits. Importantly, RyR2 is a driving and conserved mechanism for maintenance (Figure 5.8P) and activity-evoked neuronal plasticity (Figure 5.8Q) in different regions of the brain.

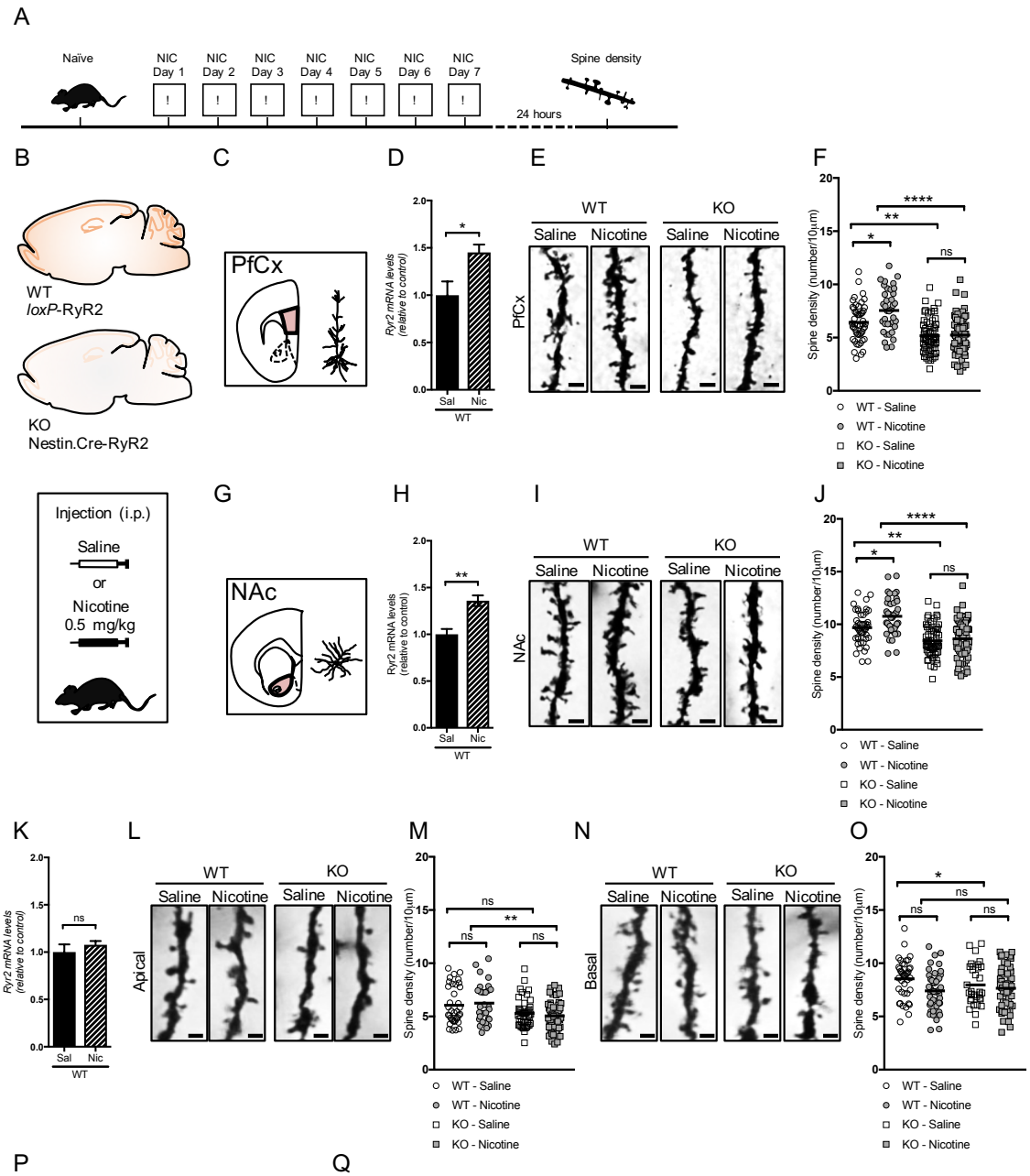
A
Naïve
NIC Day 1
NIC Day 2
NIC Day 3
NIC Day 4
NIC Day 5
NIC Day 6
NIC Day 7
Spine density
24 hours
B
WT loxP-RyR2
KO Nestin.Cre-RyR2
C
PfCx
D
Ryr2 mRNA levels (relative to control)
Sal
Nic
WT
E
WT
KO
Saline
Nicotine
PfCx
F
Spine density (number/10µm)
WT - Saline
WT - Nicotine
KO - Saline
KO - Nicotine
Injection (i.p.)
Saline
or
Nicotine
0.5 mg/kg
G
NAc
H
I
J
K
L
Apical
M
N
Basal
O
ns
P
Wild type (adult brain)
RyR2 deletion
Maintenance of dendritic spines
Q
Ryr2 KO (adult brain)
Experience-driven spine remodeling
Plastic remodelling of dendritic spines

5.8 Nicotine-dependent spine remodeling of excitatory and inhibitory neurons in the mesolimbic pathway requires RyR2. (A) Experimental setup for chronic administration of nicotine. (B) Control and whole-brain *Nestin-Cre*$^{tg/wt}$*;Ryr2*$^{fl/fl}$ mice were chronically treated with nicotine (i.p. 0.5mg/kg) or saline solution for 7 consecutive days. (C-D) *Ryr2* expression levels in the prefrontal cortex of control mice treated with saline solution or nicotine (WT saline: n=5, WT nicotine: n=6). (E-F) Brains were collected 24 h after the last nicotine injection and Golgi-stained spines were counted in the apical dendrites of cortical pyramidal cells, comparing nicotine-treated and saline-treated control and *Nestin2α-Cre*$^{tg/wt}$*;Ryr2*$^{fl/fl}$ mice (WT naïve: n=50 cells/ 5 mice , WT nicotine: n=36 cells/ 4 mice, KO naïve: n=59 cells/ 6 mice, KO nicotine: n=69 cells/ 7 mice). Scale bar: 2 μm. (G-H) *Ryr2* expression levels in the NAc of control mice treated with saline solution or nicotine (WT saline: n=5, WT nicotine: n=7). (I-J) Spines were counted in the secondary dendrites of the GABAergic medium spiny neurons (MSNs), comparing nicotine-treated and saline-treated control and *Nestin2α-Cre*$^{tg/wt}$*;Ryr2*$^{fl/fl}$ mice (WT naïve: n=45 cells/ 5 mice , WT nicotine: n=40 cells/ 4 mice, KO naïve: n=58 cells/ 6 mice, KO nicotine: n=65 cells/ 7 mice). Scale bar: 2 μm. (K) *Ryr2* expression levels in the hippocampus of control saline- and nicotine-injected mice (WT saline: n=3, WT nicotine: n=3). (L-O) Spine density in the apical (L-M) (WT naïve: n=36 cells/ 5 mice , WT nicotine: n=28 cells/ 4 mice, KO naïve: n=44 cells/ 6 mice, KO nicotine: n=52 cells/ 7 mice) and basal (N-O) (WT naïve: n=41 cells/ 5 mice , WT nicotine: n=47 cells/ 4 mice, KO naïve: n=36 cells/ 6 mice, KO nicotine: n=56 cells/ 7 mice) dendrites of CA1 neurons, comparing nicotine-treated and saline-treated control and *Nestin-Cre*$^{tg/wt}$*;Ryr2*$^{fl/fl}$ mice. Scale bar: 2 μm. Data are reported as mean ± SEM. Unpaired Student's *t* test or Two-way ANOVA or RM two-way ANOVA with Bonferroni post hoc comparison, ****p<0.0001, ***p<0.001, **p<0.01, *p<0.05. Statistical analyses are reported in Table 6.1.

6. Table of statistics

Table 6.1 Statistical analysis for dendritic spine density.

Fig.	Model	Test	Factor	F(DFn,Dfd)	p-value	Sum	Bonf.	*p* value	Sum
5.1E	Primary neurons DIV 14	Unpaired *t* test	Treatment		*p*=0.082	**			
5.1K	Primary neurons DIV 14 cLTP (L)	Two-way ANOVA	Interaction Genotype cLTP	F(1, 98)=3.11 F(1, 98)=9.16 F(1, 98)=31.57	*p*=0.081 *p*=0.0026 *p*<0.0001	**ns** ** ****	WT vs KO WT vs WT L KO vs KO L WT L vs KO L	*p*=0.0218 *p*=0.0037 *p* >0.99 *p*<0.0001	* ** **ns** ****
5.1L	Primary neurons DIV 14 cLTP (L)	Two-way ANOVA	**Mushroom** Interaction Genotype cLTP **Thin** Interaction Genotype cLTP **Stubby** Interaction Genotype cLTP	 F(1, 99)=1.105 F(1, 99)=21.69 F(1, 99)=32.8 F(1, 99)=0.27 F(1, 99)=0.294 F(1, 99)=0.287 F(1, 99)=0.032 F(1, 99)=11.15 F(1, 99)=21.9	 *p*=0.97 *p*<0.0001 *p*<0.0001 *p*=0.86 *p*=0.86 *p*=0.59 *p*=0.85 *p*=0.0012 *p*<0.0001	 **ns** **** **** **ns** **ns** **ns** **ns** ** ****	 WT vs KO WT vs WT L KO vs KO L WT L vs KO L WT vs KO WT vs WT L KO vs KO L WT L vs KO L WT vs KO WT vs WT L KO vs KO L WT L vs KO L	 *p*=0.0002 *p*=0.0050 *p*=0.0127 *p*=0.0015 *p*>0.99 *p*>0.99 *p*>0.99 *p*>0.99 *p*=0.0048 *p*=0.067 *p*=0.2 *p*=0.011	 *** ** * ** **ns** **ns** **ns** **ns** ** **ns** **ns** *
5.3J	*Synapsin-Cre;Ryr2*^{ko} Purkinje	Unpaired *t* test	Genotype		*p*=0.0320	*			
5.4D	*Synapsin-Cre;Ryr2*^{ko} CA1	Two-way ANOVA	Interaction Genotype Region	F(1, 299)=1.105 F(1, 299)=9.137 F(1, 299)=26.56	*p*=0.2940 *p*=0.027 *p*<0.0001	**ns** ** ****	WT vs KO apical WT vs KO basal	*p*=0.9410 *p*=0.0297	**ns** *
5.4D	*Synapsin-Cre;Ryr2*^{ko} CA3	Two-way ANOVA	Interaction Genotype Region	F(1, 174)=1.522 F(1, 174)=6.804 F(1, 174)=21.41	*p*=0.2189 *p*<0.0099 *p*<0.0001	**ns** ** ****	WT vs KO Apical WT vs KO basal	*p* = 0.209 *p* =0.038	**ns** *
5.4D	*Synapsin-Cre;Ryr2*^{ko} DG	Unpaired *t* test	Genotype		*p*=0.170	**ns**			
5.6J	*Camk2α-Cre;Ryr2*^{ko} CA1 apical Training (T)	Two-way ANOVA	Interaction Genotype Training	F(1,226)=17.69 F(1,226)=42.38 F(1,226)=9.402	*p*<0.0001 *p*<0.0001 *p*=0.0024	**** **** **	WT vs KO WT vs WT T KO vs KO T WT T vs KO T	*p*=0.8038 *p*<0.0001 *p* >0.99 *p*<0.0001	**ns** **** **ns** ****
5.6L	*Camk2α-Cre;Ryr2*^{ko} CA1 basal Training (T)	Two-way ANOVA	Interaction Genotype Training	F(1, 227)=7.457 F(1, 227)=54.75 F(1,227)=0.303	*p*=0.0068 *p*<0.0001 *p*=0.5825	** **** **ns**	WT vs KO WT vs WT T KO vs KO T WT T vs KO T	*p*=0.0141 *p* =0.764 *p* >0.99 *p*<0.0001	* **ns** **ns** ****

5.7H	*Camk2α-Cre;Ryr2*$^{fl/fl}$ CA1 apical Cocaine (C)	Two-way ANOVA	Interaction Genotype Cocaine	F(1,122)=1.247 F(1,122)=22.96 F(1,122)=16.72	p=0.2664 p<0.0001 p<0.0001	**ns** **** ****	WT vs KO WT vs WT C KO vs KO C WT C vs KO C	p=0.0658 p=0.0067 p=0.0813 p=0.0002	**ns** ** **ns** ***
5.7J	*Camk2α-Cre;Ryr2*$^{fl/fl}$ CA1 basal Cocaine (C)	Two-way ANOVA	Interaction Genotype Cocaine	F(1,131)=0.547 F(1,131)=20.22 F(1,131)=10.79	p=0.778 p<0.0.23 p=0.0025	**ns** * **	WT vs KO WT vs WT C KO vs KO C WT C vs KO C	p=0.604 p=0.131 p=0.136 p=0.2401	**ns** **ns** **ns** **ns**
5.8F	*Nestin-Cre;Ryr2*$^{fl/fl}$ PfCx apical Nicotine (N)	Two-way ANOVA	Interaction Genotype Nicotine	F(1, 211)=4.718 F(1, 211)=52.84 F(1, 211)=5.825	p=0.0310 p<0.0001 p=0.0167	* **** *	WT vs KO WT vs WT N KO vs KO N WT N vs KO N	p=0.0016 p=0.0205 p>0.99 p<0.0001	** * **ns** ****
5.8J	*Nestin-Cre;Ryr2*$^{fl/fl}$ NAc MSN Nicotine (N)	Two-way ANOVA	Interaction Genotype Nicotine	F(1, 204)=3.509 F(1, 204)=51 F(1, 204)=7.307	p=0.0625 p<0.0001 p=0.0074	**ns** **** **	WT vs KO WT vs WT N KO vs KO N WT N vs KO N	p=0.001 p=0.0205 p>0.99 p<0.0001	** * **ns** ****
5.8M	*Nestin-Cre;Ryr2*$^{fl/fl}$ CA1 apical Nicotine (N)	Two-way ANOVA	Interaction Genotype Nicotine	F(1, 157)=0.790 F(1, 157)=14.94 F(1, 157)=0.009	p=0.3753 p=0.0002 p=0.92	**ns** *** **ns**	WT vs KO WT vs WT N KO vs KO N WT N vs KO N	p=0.145 p=0.955 p=0.86 p=0.0063	**ns** **ns** **ns** **
5.8O	*Nestin-Cre;Ryr2*$^{fl/fl}$ CA1 basal Nicotine (N)	Two-way ANOVA	Interaction Genotype Nicotine	F(1, 172)=2.022 F(1, 172)=6.355 F(1, 172)=0.323	p=0.1568 p=0.0126 p=0.5703	**ns** * **ns**	WT vs KO WT vs WT N KO vs KO N WT N vs KO N	p=0.0260 p=0.0.56 p=0.909 p=0.8705	* **ns** **ns** **ns**

Table 6.2 Statistical analysis of behavioral test.

Fig.	Test	Statistic	Factor	F(DFn,Dfd)	p-value	Sum	Bonf.	*p*-value	Sum
5.3B	Open Field Distance moved *Synapsin- Cre;Ryr2*^{wt} mice	Unpaired *t* test	Genotype		*p*=0.009	***			
5.3C	Open Field Velocity *Synapsin-* *Cre;Ryr2*^{wt}mice	Unpaired *t* test	Genotype		*p*=0.0091	**			
5.3D	RotaRod Fall latency *Synapsin-* *Cre;Ryr2*^{wt}mice	Two-way RM ANOVA	Interaction Day Genotype	F(2,120)=6.597 F(2,120)=26.03 F(1,60)=9.041	*p*=0.002 *p*<0.0001 *p*=0.0039	** **** **	WT vs KO Day 1 Day2 Day3	 *p*=0.8156 *p*=0.0019 *p*=0.0015	 ns ** **
5.3E	MWM Training velocity *Synapsin-* *Cre;Ryr2*^{wt}mice	Unpaired *t* test	Genotype		*p*<0.0001	****			
5.3F	MWM Training floating *Synapsin-* *Cre;Ryr2*^{wt}mice	Two-way RM ANOVA	Interaction Day Genotype	F(5,85)=3.99 F(5,85)=0.55 F(1,17)=13.44	*p*=0.002 *p*=0.73 *p*=0.0019	** ns **			
5.6B	Open Field Distance moved *Camk2α-* *Cre;Ryr2*^{wt}mice	Unpaired t test	Genotype		*p*=0.157	**ns**			
5.6C	RotaRod Fall latency *Camk2α-* *Cre;Ryr2*^{wt}mice	Two-way RM ANOVA	Interaction Day Genotype	F(2,58)=0.006 F(2,58)=21.31 F(1,29)=0.0009	*p*=0.94 *p*<0.0001 *p*=0.97	**ns** **** **ns**			
5.6E	MWM Escape Latencies *Camk2α-* *Cre;Ryr2*^{wt}mice	Two-way RM ANOVA	Interaction Day Genotype	F(4,116)=1.003 F(4,116)=34 F(1,29)=9.938	*p*=0.409 *p*<0.0001 *p*=0.0037	**ns** **** **	WT vs KO Day1 Day2 Day3 Day4 Day5	 *p*>0.9999 *p*=0.0936 *p*=0.0121 *p*=0.1196 *p*>0.9999	 ns ns * ns ns
5.6F	MWM Quadrant occupancy (90min) *Camk2α-* *Cre;Ryr2*^{wt}mice	Two-way RM ANOVA	Interaction Quandrant Genotype	F(3,90)=5.293 F(3,90)=46.28 F(1,90)=1.136	*p*=0.0021 *p*<0.0001 *p*=0.295	** **** **ns**	WT vs KO Target Right Left Opposite	 *p*=0.0008 *p*=0.6355 *p*>0.9999 *p*=0.1689	 *** ns ns ns
5.6G	MWM Quadrant occupancy (24h) *Camk2α-* *Cre;Ryr2*^{wt}mice	Two-way RM ANOVA	Interaction Quandrant Genotype	F(3,99)=0.602 F(3,99)=18.5 F(1,33)=2.112	*p*=0.602 *p*<0.0001 *p*=0.1556	**ns** **** **ns**	WT vs KO Target Right Left Opposite	 *p*>0.9999 *p*>0.9999 *p*>0.9999 *p*>0.9999	 ns ns ns ns
5.7E	CCP score Cocaine treatment *Camk2α-* *Cre;Ryr2*^{wt}mice	Unpaired t test	Genotype		*p*=0.0204	*			

Table 6.3 Statistical analysis of *rAAV.Camk2α.GFP* and *rAAV5.Camk2α.Cre-GFP* reconstructed CA1 pyramidal cells.

Neurons	Control	RyR2 KO	*p* value	Sum
Basal dendrites				
Length (μm)	2268±185.5	1381±149.2	0.0006	***
Surface area (μm²)	14672±1223	8700±905.1	0.0003	***
Volume (μm³)	8391±743.5	4859±554.1	0.0004	***
Dendritic thickness (μm)	2.193±0.04045	2.04±0.04509	0.0173	*
Number branch points	35.44±3.58	21.14±2.925	0.0035	**
Apical dendrites				
Length (μm)	2938±271.3	2386±161.5	0.0729	**ns**
Surface area (μm²)	20193±1724	15494±1205	0.0277	*
Volume (μm³)	12042±992.9	8749±779.9	0.0128	*
Dendritic thickness (μm)	2.318±0.05193	2.159±0.0321	0.0100	*
Number branch points	34.5±4.863	32.1±3.8	0.6964	**ns**
Total				
Length (μm)	4810±461.6	3335±282.5	0.0100	*
Surface area (μm²)	32122±2921	22280±2032	0.0097	**
Volume (μm³)	18767±1674	12936±1403	0.0133	*
Dendritic thickness (μm)	2.264±0.05678	2.08±0.04186	0.0197	*
Number branch points	65.55±9.009	44.54±5.7	0.0543	**ns**

Table 6.4 Statistical analysis of reconstructed dendritic spines of *rAAV.Camk2α.GFP* and *rAAV5.Camk2α.Cre-GFP* transfected CA1 pyramidal cells.

Spines	Control	RyR2 KO	*p* value	Sum
S. Oriens				
Density	9.556±0.7015	6.004±0.842	0.0037	**
% Mushroom	59.47±1.652	46.64±2.726	0.0005	***
% Thin	10.18±0.9954	8.701±1.229	0.3569	**ns**
% Stubby	30.25±1.579	44.45±3.074	0.0003	***
Spine length (μm)	1.217±0.0193	1.095±0.0254	0.0001	***
S. Radiatium				
Density	11.4±0.6692	7.797±1.195	0.0137	*
% Mushroom	56.86±2.124	53.98±2.891	0.4356	**ns**
% Thin	12.01±1.481	12.8±1.381	0.7026	**ns**
% Stubby	31.13±1.428	33.22±2.051	0.4170	**ns**
Spine length (μm)	1.224 ± 0.02199	1.219±0.0227	0.8663	**ns**
S. Lac-Moleculare				
Density	8.444±0.6342	4.529 ± 0.34	<0.0001	****
% Mushroom	55.99±2.851	46.88±3.025	0.0386	*
% Thin	18.14±1.475	15.45±1.878	0.2639	**ns**
% Stubby	25.87±2.218	37.32±3.003	0.0046	**
Spine length (μm)	1.396±0.02258	1.29±0.03129	0.0068	**
Total				
Density	9.602±0.425	5.848 ±0.4809	<0.0001	****
% Mushroom	57.32±1.865	47.96±1.674	0.0022	**
% Thin	12.84±1.126	12.88±1.1	0.9771	**ns**
% Stubby	29.79±1.268	38.9±1.568	0.0005	***
Spine length (μm)	1.38±0.0132	1.219±0.0193	<0.0001	****

7. Discussion

Formation, maturation and elimination of dendritic spines shape the connectivity of neuronal networks and underpin learning, memory and forgetting. According to the developmental stage, different mechanisms dictate the remodeling of dendritic spines. From embryogenesis until postnatal ages, *de novo* formation of dendritic spines relies on extrinsic cues and intrinsic programs (Ledda and Paratcha, 2017). In adulthood, spines are generally preserved and slowly decline during aging, when the aberrant loss of connectivity strongly correlates with cognitive defects, as seen in the elderly (Bourgeois and Rakic, 1993; Duan et al., 2003; Dumitriu et al., 2010). Thus, the understanding of the pathophysiological mechanisms underlying neuronal structure and connectivity in adulthood remains an outstanding and relevant question, with important implications for the development of new targeted strategies against age-related cognitive dysfunction.

In an effort to clarify the processes modulating the stability and dynamics of dendritic spines in adulthood, we hypothesized a critical role for RyR-mediated CICR. We generated a set of brain-specific *Ryr2* knockout mice. First, we focused on neuronal-specific *Syn-Cre*$^{tg/wt}$*;Ryr2*$^{fl/fl}$ mice. Loss of RyR2 did not result in any noticeable change in gross brain morphology. However, open field and RotaRod tests highlighted a reduced locomotion and impaired motor skills learning. To explain such a defect, we studied the cerebellum, since it is a region functionally linked to motor coordination. Macro anatomy, cerebellar lamination, content and complexity of Purkinje cells were unaltered. These findings do not confirm the previously published involvement of RyR2 in mediating dendritic complexity and differentiation of Purkinje cells, as shown in *in vitro* cerebellar cultures (Ohashi et al., 2014). Instead, we detected a mild but significant decrease in the number of spines in Purkinje cells. Such a reduction may explain the locomotor deficiency, although we could not exclude that other neuronal circuits had contributed to the observed behavioral changes. In this regard, RyRs were previously reported to play a role in neuromuscular junctions (Gartz Hanson and Niswander, 2015; Liu et al., 2005), axon stability in the spinal cord (Kihira et al., 2005; Liao et al., 2016; Pelisch et al., 2017; Shimizu et al., 2008) and in the dopamine release of the nigrostriatal circuit (Wan et al.,

1999). A much broader and detailed characterization of our models may give more insight into the contribution of RyR2 in these tissues.

The defective motor coordination prevented us from further investigating other cognitive functions using *Syn-Cre*$^{tg/wt}$*;Ryr2*$^{fl/fl}$ mice. On the other hand, *Syn-Cre*$^{tg/wt}$*;Ryr2*$^{fl/fl}$ mice exhibited reduced spine content in the CA1 and CA3 pyramidal cells of the hippocampus. Therefore, we restricted the *Ryr2* deletion in the forebrain using *Camk-Cre*$^{tg/wt}$*;Ryr2*$^{fl/fl}$ mice. *Camk-Cre*$^{tg/wt}$*;Ryr2*$^{fl/fl}$ mice showed reduced spatial learning and short-term memory, while they were still capable of developing normal long-term memories. These data suggest a reduced hippocampus-dependent memory acquisition, which is further confirmed by the defective context-associated memory and reward behavior upon cocaine treatment as reported in our contextual place preference test. Our results are in line with previous studies suggesting that the pharmacological modulation of RyRs alters cognitive processes (Adasme et al., 2011; Baker et al., 2010; Edwards and Rickard, 2006; Galeotti et al., 2008; Shimuta et al., 2001). Consistently, downregulation of *Ryr2* by intrahippocampal injection of ODNs has been shown to impair spatial memory in mice tested in the Oasis Maze, a dry version of the MWM (More et al., 2018). Moreover, forebrain deletion of *Ryr2* partially phenocopies the memory deficiency of the genetic model full-knockout for *Ryr3* (Balschun et al., 1999; Futatsugi et al., 1999), albeit lack of *Ryr3* was shown to affect only reversal learning in MWM (Balschun et al., 1999; Futatsugi et al., 1999; Shimuta et al., 2001). Together, these data confirm the involvement of RyRs in spatial learning and memory formation. The higher content of RyR2 in the hippocampus compared to RyR3 may explain its predominant role. However, we cannot exclude the possibility that different RyR isoforms may have unique functions in distinct brain regions or cell types.

Structure, density and turnover of dendritic spines impact learning and memory. In immature neurons, the physiological coupling between NMDAR and CICR allow the formation of new dendritic spines that can eventually form neuronal circuitries (Lee et al., 2016; Oh et al., 2015). In order to study a possible role of CICR in adult neurons, we performed a thorough characterization of spine content in all our transgenic models. Pre-natal (*Nestin-Cre*$^{tg/wt}$ and *Synapsin-Cre*$^{tg/wt}$) and post-natal (*Camk2α;Ryr2*$^{fl/fl}$) deletion of RyR2 led to a mild but significant reduction of spines in both excitatory and inhibitory neurons, including in the CA1 and CA3 of the hippocampus, prefrontal cortex, nucleus accumbens

and cerebellum. Our data support that RyR2 is involved in the homeostasis of spines across brain regions. This phenotype is particular of RyR2 since 3 month-old RyR3 transgenic knockout mice were shown to have normal density and mature spines in CA1 neurons (Liu et al., 2014). This discrepancy can be explained by possible compensatory or developmental mechanisms. In line with this hypothesis, *Synapsin-Cre*$^{tg/wt}$*;Ryr2*$^{fl/fl}$ mice exhibit *Ryr3* up-regulation in the hippocampus compared to control animals. Moreover, AAV-mediated *RyR2* deletion in adult CA1 neurons causes a much stronger reduction of spines, in particular of mushroom spines. Strikingly, this loss of complexity is not limited to spines, but it extends to the dendritic shafts. RyR2 KO cells present a decreased membrane cell area and reduced dendritic arborization, which overall results in smaller neurons. This evident shrinkage may significantly affect the input resistance of neurons, leading to increased excitability and disrupted patterns of neuronal activity (Lerdkrai et al., 2018; Siskova et al., 2014). Therefore, while the loss of RyR2 within a certain timeframe can be partially compensated for, it is less efficient or even absent in adult neurons. Thus, RyR2-mediated Ca^{2+} signaling may be one of the intrinsic programs that defines neuronal morphology. Yet, it remains unclear whether and how the pre- or the early post-natal deletion of *Ryr2* influences the architecture of hippocampal neurons. Overall, our data indicate that RyR2 strongly stabilizes the architecture of adult cells, in particular the maintenance of dendrites and mature spines.

Experience-driven neuronal activation dynamically shapes spines through Ca^{2+}-dependent mechanisms at the base of the Hebbian plasticity (Engert and Bonhoeffer, 1999; Hubener and Bonhoeffer, 2010; Rochefort and Konnerth, 2012). Starting from previous *in vitro* findings and from the abundance of RyR2 in the hippocampus (Zhao et al., 2000) (Adasme et al., 2011; More et al., 2018), we hypothesized that RyR2 could be involved in activity-evoked remodeling of hippocampal neurons. To clarify the effect of RyR2 on spine plasticity, we performed *in vitro* experiments in primary dissociated neurons and found that RyR2 is essential for cLTP-mediated biogenesis, rather than the maturation of spines. This set of data is in line with previous evidence obtained from primary neurons (Adasme et al., 2011; Korkotian and Segal, 1999; More et al., 2018). To address the gap of knowledge in the field, we set off to translate these finding *in vivo*. Using three independent paradigms, we tested spinogenesis associated with *Ryr2* up-regulation in distinct neuronal

circuits (Adasme et al., 2011; Ziviani et al., 2011). First, we triggered spine remodeling in the hippocampus by subjecting mice to the MWM test (Moser et al., 1994). We exposed *Camk2α-Cre;Ryr2*$^{fl/fl}$ mice to spatial training and observed no remodeling of spines in comparison to naïve littermates, which demonstrated that RyR2 and its up-regulation is a driving force for activity-evoked spine remodeling in CA1 neurons. Secondly, we tested whether RyR2-mediated spine remodeling occurred regardless of the nature of the stimulus, as demonstrated by our paradigm of the cocaine-induced *Ryr2* upregulation in the hippocampus (Ka et al., 2016; Ziviani et al., 2011). Cocaine administration produced increased spine density only in control animals but not in *Camk2α-Cre;Ryr2*$^{fl/fl}$ mice, suggesting that the RyR2 modulates the plasticity of CA1 neurons necessary for the formation of cocaine-induced context-associated memory and reward behavior (Gauthier and Tank, 2018; LeGates et al., 2018). Third, we described that the activity-dependent genetic programming of RyR2 and consequent plastic effect is not limited to the hippocampus but is also extended to other brain regions. In a complementary paradigm of plasticity (Brown and Kolb, 2001), we subjected control and RyR2 knockout mice to chronic treatment with nicotine, which induces *Ryr2* expression in control mice in the mesolimbic and mesocortical pathways, but not in the hippocampus (Ziviani et al., 2011). Consistently, nicotine treatment did not increase spine density of CA1 pyramidal cells, whereas it did in neurons of the PfCx and NAc, two brain regions crucially involved in the behavioral sensitization of nicotine (Ziviani et al., 2011). Altogether, our data show that the genetic reprogramming of *Ryr2* occurs only in those neuronal circuits undergoing spine remodeling. Furthermore, we describe a major function of RyR2 in the plastic remodeling of dendritic spines upon neuronal activity. A mechanistic model of such an effect may be reconducted to the involvement of RyRs in the local generation of bAP Ca^{2+} transients within single spines (Johenning et al., 2015). In fact, bAP Ca^{2+} transients occur exclusively after the generation of action potentials, which could explain why RyR2 is necessary especially during activity. On the other hand, RyR2-dependent spinogenesis occurs mainly in distal dendrites, which may suggest a specialized role for each compartment. One possible explanation could be that, although well distributed along dendrites and spines (Deisseroth et al., 1996), RyR2 might dynamically cluster and aggregate, forming elementary units for Ca^{2+} release. Noteworthy, such units could be physiologically relevant

since, at least in smooth muscle cells, modified clusters of RyR2 trigger microvascular dysfunctions (Hiess et al., 2018; Hiess et al., 2015; Pritchard et al., 2018; Walker et al., 2015. In neurons, studies on RyR2 dynamics and clusters are still missing and we cannot exclude that the local distribution of RyR2 may vary within single spines during cell activity. Supporting this hypothesis, one study on synaptopodin (SP), an actin-binding protein shown to tightly couple with RyRs (Vlachos et al., 2009), claims that the recruitment of RyRs by SP at the base of spines is instrumental in the Ca^{2+}-dependent formation of those microdomains (Grigoryan and Segal, 2016). In line with these findings, a recent computation model emphasizes the relevance of the precise positioning of RyRs in tuning spine-to-dendrite Ca^{2+} communication (Breit et al., 2018). Thus, RyR2 dynamics may modulate CICR differently depending on its subcellular localization (i.e. soma, dendrites and spines).

To conclude, our findings indicate that RyR2 knockout mice have impaired spine remodeling but normal long-term memory. These data support the idea that RyR2 augments spine number as a potentiation mechanism to increase memory acquisition capacity during the learning phase. In contrast, RyR2 does not affect the preservation or the recall of formed memories. In summary, we demonstrate that *Ryr2* deletion provokes neuronal shrinkage and regression of mature spines in CA1 neurons. The role of RyR2 seems pivotal in different neuronal subtypes, since the reduction of spine density occurs in the hippocampus, cortex, mesolimbic pathway and cerebellum. Our study validates the biological meaning of the genetic reprogramming of RyR2, highlighting its function in driving mechanisms for the remodeling of spines associated with learning, memory and locomotion.

8. Methods

8.1 Animal work

8.1.1 Mice

Animal care and experiments were conducted following the institutional animal welfare guidelines approved by the State Agency for Nature, Environment and Consumer Protection (LANUV) of North Rhine-Westphalia, Germany. Mice were housed in cages of two to four under a 12/12h light/dark cycle, free access to tap water and food ad libitum (ssniff® V1534-300). All animals used in the experiments had C57BL/6 genetic background. Pups were weaned at three weeks of age and ear-clips were assigned. The following Cre transgenic mouse lines were purchased from Jackson Laboratory (Bar Harbor, ME): *CMV-Cre*$^{tg/wt}$ (B6.C-Tg(CMV-cre)1Cgn/J), *Nestin-Cre*$^{tg/wt}$ (B6.Cg-Tg(Nes-cre)1Kln/J), *Synapsin-Cre*$^{tg/wt}$ (B6.Cg-Tg(Syn1-cre)671Jxm/J) and *Camk2α-Cre*$^{tg/wt}$ (B6.Cg-Tg(Camk2α-cre)T29-1Stl/J). The generation of *Ryr2*$^{fl/fl}$ mice was performed by InGenious Targeting Laboratory (2200 Smithtown Ave, Ronkonkoma, NY 11779, United States of America).

8.1.2 Behavioral tests

Animals of both genders were used for the behavioral experiments. Mice were handled before behavioral tests.

Open field. General locomotor activity and exploratory willingness was assessed in open field squared boxes (27 cm x 27 cm x 27 cm) in a room illuminated with a diffused light. Each animal was recorded for 20 min. Total distance moved (cm) and the mean velocity (cm/s) was calculated.

Rotarod. Motor coordination was quantified with a rotarod system (TSE Systems, Bad Homburg, Germany). Mice were drilled to stand on the rod. The rod rotated with accelerating speed from 4 to 40 rpm. Fall latency from the rod was measured. The rotarod test lasted over three consecutive days with three sessions per day. The duration of the session lasted for a maximum 5 min and a 30 min break was given to the mice between individual training sessions.

Morris water maze (MWM). MWM test was used to assess spatial learning and memory in *Camk2α-Cre*$^{tg/wt}$*;Ryr2*$^{fl/fl}$ and control mice. Briefly, the MWM apparatus consisted of a white circular swimming pool (diameter of 1.5 m) filled with white colored water at 22 °C. The circular swimming pool was divided into four quadrants (target, right, opposite and left). In the target quadrant, a fixed Plexiglas platform was positioned at 0.5 cm below the water surface. Mice were trained to localize the fixed platform over 5 consecutive days of training, 4 trials per day with a maximum trial duration of 60 s. Starting positions were semi-randomized. Breaks of 30 min were given to the mice between every 2 trial sessions. Short-term memory was assessed on day 3, 90 min after the four trials of training in a 60 s probe trial, whereas long-term memory was investigated on day 6, 24 hours after the last training session. Escape latency, swim speed (cm/s), swim distance (cm), number of target crossings and time in the target compared to non-target quadrants were analyzed. Mice were sacrificed 24 h after the last training.

Conditioned place preference test (CPP). CPP was measured in *Camk2α-Cre*$^{tg/wt}$*;Ryr2*$^{fl/fl}$ and control mice treated with cocaine or saline solution. The CPP apparatus consisted of two compartments of identical sizes (27*27 cm) divided by a connecting corridor (5*10 cm). The two compartments had walls of different colors (black and white) and different grid flooring (grid rod and wire mesh) to allow the mice to discriminate between the two environments. Animals were handled one day before the experiment. Spontaneous preference for the black or white CPP compartments was assessed in the pre-test (day 1), when one animal at a time was free to access to all three distinct compartments for 20 min. Conditioning was induced during the next 6 consecutive days (day 2 – day 7). One animal at a time was injected with either saline or cocaine (20 mg/kg, i.p.) and confined to the black or to the white chamber for 20 min. The day after the first injection, all mice were injected with 0.9% saline and then placed into the opposite chamber in respect to the first injection. The conditioning phase with daily injection of cocaine or saline lasted for a total of 5 days. Cocaine-induced place preference was assessed 24 hours after the last conditioning injection (day 8). One animal at a time was free to access to all three distinct compartments again for 20 min and CPP score was calculated as the time spent in cocaine-paired minus the time spent in the saline-paired compartment. Mice were sacrificed 24 h after the CPP test.

Chronic nicotine treatment. *Nestin-Cre$^{tg/wt}$;Ryr2$^{fl/fl}$* and control mice were injected with nicotine (i.p. 0.5 mg/kg) or 0.9% saline solutions for 7 consecutive days. Mice were sacrificed 24 h after the last injection.

Behavioral tests were analyzed using the EthoVision tracking system (Noldus, The Netherlands).

8.1.3 Samples preparation

Samples for biochemical experiments were obtained from animals sacrificed through cervical dislocation. Brains were removed from the skull, dissected, snap frozen in liquid nitrogen and stored at -80°C. Brains for immunohistochemistry (IHC) were collected from animals anaesthetized with a 1:1 mixture of Ketamine and Xylazine and transcardially perfused with 4% paraformaldehyde (PFA). Brains were subsequently fixed in 4% PFA overnight at 4°C, bathed in a 30 % sucrose solution for 3-5 days at 4°C and frozen at -80°C. Brain sections (sagittal or coronal) were cut using a Cryostar NX70 (Thermo Fisher Scientific) with a thickness between 15-40 µm. Sections were frozen at -20°C in cryoprotective solution (Table 9.1).

8.2 Molecular biology

8.2.1 Genotyping mice

8.2.1.1 From biopsies to DNA

Mouse genotyping was performed using isolated genomic DNA (gDNA) from biopsies of either ears or tails, which were collected at three weeks of age after pups weaning and after their sacrifice, respectively. Samples were lysed in 500 µl of lysis buffer (Table 9.1) with 5 µl of Proteinase K (Applichem, 200 µg/ml) on shaking incubator at 55°C for at least 4 hours. Samples were centrifuged for 20 min at 13,000 *g*. The supernatant containing the DNA was added to new tubes containing 500 µl of isopropanol. DNA was precipitated for 20 min at 13,000 *g* and washed by adding 200 µl of EtOH 70% in H_2O. The remaining DNA-enriched pellet was dried at 37 °C for 1 hour and resuspended with 10-100 µl of TE^{-4} buffer (Table 9.1), proportional to the pellet size.

8.2.1.2 Polymerase chain reaction (PCR)

PCR was used for genotyping extracted gDNA from mouse biopsies. Each reaction used 1 µl of extracted gDNA as a template. Reagents used for a single PCR reaction are listed in Table 8.1. PCR reaction protocols were adapted as described in Table 8.2. Amplification of DNA fragments was performed using a Biometra thermocycler TProfessional TRIO PCR (Analytikjena). Specific oligonucleotides (Table 8.3) against CRE transgene, *loxP* and KO alleles and the CRE transgene were designed by ingenious Targeting Laboratory (iTL).

Table 8.1 PCR reaction mix.

Reagent	Volume
My Taq Red Mix (Bioline)	12 µl
Primer Fw	1 µl (10 µM)
Primer Rw	1 µl (10 µM)
gDNA	1 µl
H_2O	10 µl

Table 8.2 PCR reaction protocol.

Step	Temperature	Time
Denaturation	94 °C	5 min
Amplification (40 cycles)	94 °C	30 sec
	variable	30 sec
	72 °C	variable
Elongation	72 °C	5 min

Table 8.3 List of primers for genotyping and PCR protocols.

Primers	Fw primer	Rw primer	Amplicon (bp)	Annealing (°C)	Elongation (seconds)
Ryr2 ko	aataagattgtttagggaatgaaat	tatattaaatccatagttgccttatc	wt=979 floxed=1234 ko=351	54	30
Ryr2 floxed	gtacagctctccgtactaagagtccag	gccaaactcacttagggtaggaca	wt=400 floxed=474 ko= none.	59	45
Nestin-Cre	cgcttccgctgggtcactgtcg	tcgttgcatcgaccggtaatgcaggc	300	58	30
Synapsin-Cre	gcattaccggtcgatgcaacgagtg	gaacgctagagcctgttttgcacgttc	100	65	30
Camk2α-Cre	gcattaccggtcgatgcaacgagtg	gaacgctagagcctgttttgcacgttc	100	65	30

The PCR reaction was loaded on a 1.5 % agarose gel. RedSafe™ Nucleic Acid Staining Solution (iNtRON Biotechnology) was used to detect amplicons under UV light. Electrophoresis was run at 120-140mV for 30-40 min, depending on the gel size.

8.2.2 Quantitative mRNA expression

8.2.2.1 RNA extraction

RNA was extracted from dissected snap-frozen brains using an RNeasy kit (Qiagen). Samples were initially stored at -80 °C in QIAzol (Qiagen) lysis reagent (400-800 µl). Then, samples were thawed, homogenized on ice, transferred to Qiashredder (Qiagen) columns and centrifuged at 4 °C for 10 min at 12,000 rpm. Eluates were transferred to Phase Lock Gel Heavy tubes (5 PRIME) and 200 µl of chloroform was added. Samples were put in an agitator for 5 min at RT and then centrifuged 5 min at 13,000 *g* at 4 °C. The supernatant containing RNA (upper phase), was then transferred to new tubes. An isovolume of EtOH 70% in H_2O was added, tubes were mixed and transferred to RNeasy columns (Qiagen). Following the manufacturer's protocol, tubes were centrifuged at 4 °C for 10 min at 12,000 rpm and the flow through was discarded. Samples were washed with RW1 buffer and DNA was digested for 15 min at RT with a DNAse enzyme (Qiagen). After various washes with RW1 and RPE buffers, the final eluate was collected in RNAse-free water and stored in Eppendorf DNA LoBind tubes. RNA concentration and purity (A260/280) was tested using a NanoDrop system (Thermo Scientific) and samples were either stored at -80 °C or retro-transcribed to cDNA.

8.2.2.2 Reverse transcription polymerase chain reaction (RT-PCR)

The reverse transcription of the RNA to cDNA was performed using the qScript cDNA SuperMix (Quanta Bioscience). Concentrations and volumes for a single micro-tube (0.2 µl) are indicated in Table 8.4.

Table 8.4 Reverse transcription polymerase chain mix.

Reagent	Volume	Final concentration
qScript cDNA SuperMix	4 µl	1X
RNA template	100/300ng	5-15 ng/µl

RNase-free water	variable	-
Total volume	20 µl	-

The retro transcription was performed as per the manufacturer's instructions (Table 8.5).

Table 8.5 Reverse transcription polymerase chain protocol.

Step	Temperature	Time
I	25 °C	5 min
II	42 °C	30 min
III	85 °C	5 min

The concentration and purity (A260/280) of cDNA was tested using a NanoDrop system (Thermo Scientific) and samples were store at -20 °C.

8.2.2.3 Validation of the primers

Primers were designed using the online tool Primer Blast (National Center for Biotechnology Information, NCBI). Target mRNAs were identified through their accession numbers. Primers were designed to be specific for the target mRNA in question, amplify 50-200 bp, and to span an exon-exon junction. Primers were purchased from Sigma Life Science and stocks of oligonucleotides were stored at -20 °C at 100 µM in PCR grade H_2O (working dilution 1:10, 10 µM).

Primers were validated starting from the definition of the optimal concentration. Gene expression analysis was performed with Fast SYBR Green Master Mix (Applied Biosystems) on a Step One Plus Real Time PCR System (Applied Biosystems) using 96-well plates. As shown in Table 8.6, 5 reactions with 9 different combinations (100-400 nM) of Fw and Rw primers were tested in triplicate. In each well 1 µl of cDNA was added. Non-template wells (NT) containing only primers were used as negative controls. The preparation of the reaction was done on ice and using ice blocks.

Table 8.6 Template with different combinations of primer used for validation.

	1	2	3	4	5	6	7	8	9
A	100/100	100/200	200/100	200/200	100/400	400/100	200/400	400/200	400/400
B	100/100	100/200	200/100	200/200	100/400	400/100	200/400	400/200	400/400
C	100/100	100/200	200/100	200/200	100/400	400/100	200/400	400/200	400/400
D	100/100 NT	100/200 NT	200/100 NT	200/200 NT	100/400 NT	400/100 NT	200/400 NT	400/200 NT	400/400 NT

Before running the reaction, 96-well plates were centrifuged for 1 min at 1500 rpm. The best pair of primers and their best working concentration were selected regarding the melting curve (indicative of the primer specificity), lowest Ct (standardized MIQE guidelines) and the absence of primer dimers or off-target amplicons. To confirm the size of the amplicons and exclude the formation of other DNA products, Real-time reaction samples were run into an 3% agarose gel for 40 min at 130V.

The chosen pairs of primers were further tested to evaluate the PCR amplification efficiency. A standard cDNA was diluted with PCR grade water from 5 ng to 0.15 ng, as described in Table 8.7. Values were normalized to a housekeeping gene (actin). Non-templates were run as negative controls.

Table 8.7 Template used for standard curve.

Primer		1	2	3	4	5	6
Primer validated	A	5	2.5	1.25	0.625	0.312	0.156
	B	5	2.5	1.25	0.625	0.312	0.156
	C	5	2.5	1.25	0.625	0.312	0.156
Actin	D	5	2.5	1.25	0.625	0.312	0.156
	E	5	2.5	1.25	0.625	0.312	0.156
	F	5	2.5	1.25	0.625	0.312	0.156
Negative Ctrl	G	NT	NT				

Real-time PCR standard curves were graphically represented in Excel files as a semi-log representation line, plotting the mean Ct values versus the dilutions of the template. The slope of the curve was calculated. Delta slope of 0 (i.e. a parallel slope) with the slope of the housekeeping gene represented the best primers selected for real-time experiments.

8.2.2.4 Real-time polymerase chain reaction (Real-Time qPCR)

Gene expression analysis was conducted with Fast SYBR Green Master Mix (Applied Biosystems) on a Step One Plus Real Time PCR System (Applied Biosystems) using 96-well plates. The cycling conditions used were as follows in Table 8.8. At least 3 technical replicates were used for each sample using the comparative ΔΔCt method (Livak and Schmittgen, 2001). The validated primers used for qRT-PCR are listed in Table 8.9.

Table 8.8 Validated primers used for real-time qPCR.

Step	Temperature	Time
AmpliTaq Polymerase activation	95 °C	20 sec
Denaturation (40x)	95 °C	3s
Annealing (40x)	60°C	30 sec

Table 8.9 Validated primers used for real-time qPCR.

Name	Fw primer	Rw primer
Ryr1	agctgacaataagagcaaaatgg	tgatctgagccacctgactg
Ryr2	ctacccgaacctccagcgatact	gcaaaagaaggagatgatggtgtg
Ryr3	cagtgggtatgcttcccataa	ggccagcttgcagaatagg
IP3R1	ccacagagcaggagcttgaa	ttgccaagctggtaaggct
IP3R2	acatcgtgtccctgtacgc	tggctgcaaagaggtcaact
IP3R3	ctacccgaacctccagcgatact	caggaacttctcctgctccg
SERCA2	gatggggctccaacgaattg	tcttccccttcctcgaacca
SERCA3	gacgctcaccaccaatcaga	ctcccctttgcctcacttcg
Ca_v 1.2	cctggccatgcagcactat	gctcccaatgacgatgagga
Ca_v 1.3	tggccatgcagcactatgag	cgtgttccaggcgtcactaa

8.3 Protein detection

8.3.1 Protein extraction and quantification

Tissue was snap-frozen in liquid nitrogen and stored at – 80 °C. Samples were thawed on ice and RIPA buffer (Sigma Aldrich) and supplemented with inhibitors of proteases (Complete Protease Inhibitor Cocktail Tablets, EDTA free, Roche) and phosphatases (PhosSTOP Phosphate Inhibitor Cocktail Tablets, Roche). Samples were homogenized with an IKA Ultra-Turrax homogenizer, sonicated and incubated for 20 min on ice. Cell debris was pelleted (centrifugation 1000 *g* for 5 min). Supernatant was transferred to clean tubes and protein concentration was quantified by Bradford protein assay (Biorad), following manufacturer's instruction. Standard curve was obtained diluting bovine serum albumin (BSA) (0, 2, 4, 6, 8, 10, 12, 14 μg/μl). Samples were diluted with Leammli buffer (Table 9.1). Afterwards, protein samples were stored at -20 °C.

8.3.2 SDS-PAGE and western blot

Proteins samples (10-30 μg) were separated by SDS polyacrylamide gel electrophoresis (SDS-PAGE) (Table 9.1). Gels were self-prepared by pouring running and stacking gels in glass chambers. Stacking gel was prepared with a acrylamide concentration of 5%. Running gel was prepared with a concentration of 7% (Table 9.1). Gels were loaded with protein samples and run in a running chamber filled with running buffer (Table 9.1). Current of 80-100 V was applied and proteins migrated through the gel accordingly to their molecular weight. Afterwards, proteins were transferred on nitrocellulose membranes. Traditional wet protein transfer were run at 20 V for 15h at 4°C with a transferring buffer (Table 9.1). Proper protein transfer was controlled using Ponceau Red solution (Sigma). Nitrocellulose membranes were then, blocked for 1h in blocking solution (Table 9.1). Membranes were incubated with primary antibodies in the buffer for antibody dilution (Table 9.1). Primary antibodies were incubated overnight at 4 °C and exposed to secondary antibodies for 1h at RT after been rinsed 3 times in whishing buffer (Table 9.1). Membranes were developed with SuperSignal West Pico Chemiluminescent Substrate (Thermo-Scientific) and imaged with the chemiluminescent analyzer Chemidoc imaging system (Bio-Rad). Bands were quantified by densitometry (ImageLab software, Bio-Rad). Table 8.10 lists the antibodies used for western blot.

Table 8.10 List of antibodies.

Antibody	Host	Company	Concentration
anti-GAPDH	Rabbit	Cell Signaling, 2118	1:5000
Ryanodine receptor antibody	Mouse	Abcam, 2868	1:5000
HRP-conjugated secondary antibodies	Rabbit	Promega	1:2000

8.4 Histology and immunohistochemistry

8.4.1 Nissl staining

Nissl-stained sections were prepared as follows: EtOH 100% (2 min), EtOH 90% (2 min), EtOH 70% (2 min), bi-distilled water (2 min), Crystal Violet (15 min), bi-distilled water (2 min), EtOH 70% (2min), EtOH 90% (2 min), EtOH 100% (2 min), Xylol (2 min). Sections were mounted using DePex (VWR) and dried overnight.

8.4.2 Golgi Staining

Golgi stainings were performed using FD rapid Golgistain$_{TM}$ Kit (FD NeuroTechnologies) following the manufacturer's instructions. Briefly, mice were sacrificed through cervical dislocation and fresh brains were immersed in a 1:1 mixture of solution A and B at RT for 2 weeks in the dark. Brains were then moved to Solution C at RT for 5 days. Brains were frozen in metilbutane and kept at -80 °C. Samples were sectioned via sagittal or coronal cut with a thickness of 100 μm using a cryostat NX70 (Thermo Fisher Scientific) and mounted on glass slides. The next day, sections were developed as follows: 2 times 4 min in bi-distilled water, 10 min in development solution (1:1:2 of solution D:E:bi-distilled water), 2 times 4 min in bi-distilled water, 4 min in EtOH 50%, EtOH 70%, EtOH 90%, 3 times in EtOH 100% and a final step in Xylol. Sections were mounted using DePex (VWR) and dried overnight.

8.4.3 3,3'-Diaminobenzidine (DAB) staining

Immunohistochemical (IHC) experiments were performed using free-floating or glass slide mounted sections. 3,3'-Diaminobenzidine (DAB) staining was executed by blocking the slices in a solution of 10% NGS, 0.5% Triton-X 100, 0.1% H_2O_2 in PBS 1X. Primary antibodies were incubated in a solution of 10% NGS, 0.1% Triton-X 100, 0.5% Natzid in PBS 1X for 48-72 hours at 4 °C. Slices were then incubated with secondary biotynilated antibodies (1:500) for 48 hours at 4 °C. Sections were developed with the Vector Elite ABC kit for detection with 3-3' diaminobenzidine (DAB) following the kit's instructions. Section were mounted, dried overnight at RT and dehydrated with with 70%, 90%, and 100% ethanol incubations. Coverslips were mounted using DePex Mounting Media (VWR). The listed antibodies were used for IHC (Table 8.11).

Table 8.11 List of antibodies used for DAB.

Antibody	Host	Company	Concentration
anti-calbindin	Rabbit	Swant CD 68	1:1000
biotinylated antibodies	Anti-rabbit	Dako	1:1000

8.4.4 *In situ* hybridization

In situ hybridization experiments were performed using the RNAscope® Multiplex Flourescent Reagent Kit v2 (ACD, a bio-techne brand). Assays were operated as described in the company's protocol. Brain sections of 30-35 μm of thickness were mounted on glass slides and dried for 60 min. Slides were rinsed in PBS and RNAscope® Hydrogen Peroxide was added at RT for 10 min. Target retrieval was performed using the kit Target Retrieval Reagent at 90 °C for 5 min. Sections were shortly washed in bi-distilled water, dehydrated in 100% alcohol for 3 min and dried for 30 min at 37 °C. RNAscope® Protease III was added to the sections for 30 min at 40 °C. The probe was hybridized and amplified following the company's instructions. The TSA® Plus Cyanine 3 (CyR3,1:750) (Perkinelmer) fluorophore was used to detect the amplified probe. Brain nuclei were stained with DAPI (4′,6-diamidino-2-phenylindole) for 15 min at RT. Coverslips were mounted using Dako Fluorescent Mounting Media (S3023, Agilent). The *Ryr2* probe (Cat No. 479981) was purchased from ACD probes to detect the mRNA target region 735–1636 bp.

8.5 Preparation and culturing of primary hippocampal neurons

Primary dissociated hippocampal neurons were prepared using E18-19 embryos from pregnant Sprague Dawley rats. Hippocampi were dissected in cold solution (Table 9.1), mechanically dissociated and digested with trypsin. Neurons were seeded onto 15 mm coverslips pre-coated with 1 mg/ml poly-L-lysine and grown in DMEM (Gibco) + 10% Horse Serum at a cell density of 17,000 cell/cm^2. Medium was replaced with Neurobasal Medium (1% B27, antibiotics and glutamine) after 4 hours. Neurons were transfected at DIV8 using calcium phosphate with the following vectors: SMART vector RyR2, promoter mCMV expressing Turbo GFP (V3SR11242-240064983), SMART vector Non-targeting Control, promotor mCMV expressing Turbo GFP (VSC11708). Calcium phosphate was performed collecting the Neurobasal Medium and bathing neurons in MEM+Glutamax (Gibco) for 30 min. Meanwhile DNA precipitates were prepared mixing DNA plasmids with H_2O and $CaCl_2$ at a final concentration of 2 μg/μl. Precipitates were obtained by adding 80 μl of the solution containing the DNA dropwise to a tube with 80 μl of HBS 2X. Precipitates were put in the dark at RT for 30 min and then added to neurons for 12 min. Afterwards neurons were washed 2 times in MEM+Glutamax and finally after 20 min

MEM+Glutamax was replaced with the original Neurobasal Medium. Pharmacological inhibition of RyRs was performed with 50μM ryanodine (Tocris) in DIV14 neurons. DMSO was used as a control. To induce cLTP, neurons were incubated in ACSF buffer for 30 min, stimulated in ACSF (without $MgCl_2$) with 0.05 mM Forskolin (Sigma Aldrich), 0.1 mM Picrotoxin (Tocris) and 100 nM Rolipram (Calbiochem) for 16 min. Cells were incubated again in ACSF for 44 min. Untreated cells were incubated in ACSF for all the experimental time. Cells were fixed 5 min in PBS containing 4% paraformaldehyde and 4% sucrose.

8.6 Imaging

8.6.1 Microscopy

Histological samples (*i.e.*, sections stained with Nissl, Golgi and DAB) were imaged using Zeiss EPI-SCOPE1 Apotome (ZEN 2012 blue edition) in bright field. The microscope was equipped with 20x, 40x and 63x objectives (Zeiss). Image analysis was performed in ImageJ (US National Institutes of Health, Maryland, USA). Fluorescent imaging of sections and cells was performed with the LSM 700 or upright LSM 700 Zeiss confocal microscope equipped with ZEN 2012 black edition (Zeiss) and with 20x, 40x or 63x Plan-Apochromat objectives.

8.6.2 Reconstruction of neurons and spine morphology

Stereotactic viral injections in *Ryr2*$^{p/p}$ mice were performed as previously described (Fuhrmann et al., 2015). Briefly, *rAAV5.CamKIIa.GFP-cre* (Gene Therapy Center Vector Core, The University of North Carolina at Chapel Hill) and *rAAV.CamKII.GFP* as a control vector (UNC, Gene Therapy, Center VectorCore) were injected in separate groups of mice. Electrophysiological experiments were performed 4-6 weeks after viral injection in transverse hippocampal slices (thickness: 300 μM), using a VT-1200S vibratome (Leica Microsystems, Wetzlar, Germany) bathed in ice-cold sucrose solution containing: 60 mM NaCl, 100 mM sucrose, 2.5 KCl, 1.25 NaH2PO4, 26 NaHCO3, 1 CaCl2, 5 MgCl2, 20 glucose, oxygenated with 95 % O2 and 5 % CO2. Coronal hippocampal slices were placed

for 30 min at 35 °C in sucrose solution for recovery and then bathed in ACSF (Table 9.1) at RT, where they were kept up to 6 hours for patch-clamp recording. Neurons electrophysiologically recorded were filled with biocytin (0.4%) through a recording pipette. Sections were fixed in paraformaldehyde (4%) for 12 hours, washed with 0.1M PBS at RT, incubated 15 min in 0.5% Triton X-100 and stained using streptavidin-coupled Alexa 555 (4mg/ml in TBS-2%NGS) (life technologies, S21381) for 2 hours. Sections were mounted with Poly Aqua Mount (Polysciences) and stored at 4°C in the dark. Single whole-neuronal imaging was obtained with tile z-stack scans of 70–130 planes using a 20x objective. Morphological reconstructions of neurons were performed using Imaris FilamentTracer (Bitplane). The following parameters were measured: dendritic volume, dendritic length, number of dendritic segments, number of dendritic branches, dendritic area, branch level and Scholl analysis. Images for the reconstruction of dendritic spines were acquired using a 63x objective (Plan Apochromat 63x 1.4, Zeiss). In order to improve the quality of the reconstructions, images were deconvoluted with Huygens software (Scientific Volume Imaging). NeuronStudio was used for semi-automatic morphological characterization of spines (Rodriguez et al., 2008; Wearne et al., 2005).

8.7 Statistics

GraphPad Prism Software 7 (GraphPad Software) was used for statistical analyses. All the data are shown as means ± SEM. Statistical analysis used is specified in each experiment. Real Time-PCR data were performed by comparative ΔΔCt. Statistical significance was reported as ****$p<0.0001$, ***$p<0.001$, **$p<0.01$, *$p<0.05$.

9. Materials

Table 9.1 List of buffers.

Buffer	Compound
ACSF	125 mM NaCl, 2.5 mM KCl, 1 mM $MgCl_2$, 2 mM $CaCl_2$, 33 mM D-glucose and 25 mM HEPES, pH 7.3
ACSF - Mg	125 mM NaCl, 2.5 mM KCl, 2 mM $CaCl_2$, 33 mM D-glucose and 25 mM HEPES, pH 7.3
Cryoprotective solution	8.56g+0.14g $MgCl_2*H_2O$ in PBS and up to 100 ml with glycerol
Cold Solution	136 mM NaCl, 5.4 mM KCl, 0.2 mM Na2HPO4, 2mMKH2PO4, 16.7 mM glucose, 20.8 mM sucrose, 0.0012% phenol red, and 10 mM HEPES, pH 7.4
Lysis buffer	100 mM Tris/HCL pH 8.5; 5 mM EDTA; 0.2% (w/v) SDS; 200mM NaCl; 200 µg/ml Proteinase K
TE^- buffer	10 mM Tris/HCl pH 8.0; 0.1 mM EDTA pH 8.0; for DNA from tissue/tail with RNase A (end-concentration 50 µg/ml)
Leammli buffer	250 mM Tris/HCL pH 6.8; 8% SDS; 40% glycerol; 20% β-mercaptoethanol, 1 mg/ml bromophenolblue
Upper gel solution	125 mM Tris Base, 0.1% SDS (pH 6.8), 6% acrylamide. 0.5% (w/v) APS and 1 µL/mL TEMED added prior polymerization
Lower gel solution	375 mM Tris Base, 0.1% SDS (pH 8.8), 7% acrylamide. 0.34% (w/v) APS and 1 µL/mL TEMED added prior polymerization
Running buffer	25 mM Tris Base, 192 mM glycine, 0.1% (w/v) SDS
Transfer buffer	10% Methanol, 10% TRIS glycine, 0.05% Tween 20 in H_2O
Blocking buffer	15.3 mM Tris-HCl. 1.4 M NaCl, 5% BSA (pH 7.6), freshly prepared
Washing buffer	15.3 mM Tris-Hcl. 1.4 M NaCl, 0.05% Tween (pH 7.6)
Buffer for Ab diliution	15.3 mM Tris-Hcl. 1.4 M NaCl, 0.05% Tween (pH 7.6), 5% BSA (pH 7.6), freshly prepared

Table 9.2 List of reagents/kits.

Reagent/Kit	Company
96-well plates	Applied Biosystems
12-well plates	Applied Biosystems
B27	Gibco
Bradford protein assay	Biorad
Chloroform	Applichem
Complete Protease Inhibitor Cocktail Tablets	Roche
Dako Fluorescent Mounting Media	Agilent
DePex	VWR
DMEM	Gibco
DNAse enzyme	Qiagen
DNA LoBind tubes	Eppendorf
Fast SYBR Green Master Mix	Applied Biosystems
FD rapid Golgistain™ Kit	FD NeuroTechnologies
GlutaMax	Gibco

Lysis reagent Qiashredder	Qiagen
Micro-tube (0.2 µl)	npnerbe plus
My Taq Red Mix	Bioline
NeuroBasal	Gibco
Nitrocellulose membranes	POTRAN
Normal Goat Serum	Biozol
Phase Lock Gel Heavy tube	5 PRIME
PhosSTOP Phosphate Inhibitor Cocktail Tablets	Roche
QIAzol	Qiagen
qScript cDNA SuperMix	Quanta Bioscience
RedSafe™ Nucleic Acid Staining Solution	iNtRON Biotechnology
RIPA buffer	Sigma Aldrich
RNAscope® Hydrogen Peroxide	ACD, a bio-techne brand
RNAscope® Multiplex Flourescent Reagent Kit v2	ACD, a bio-techne brand
RNAscope® Protease III	ACD, a bio-techne brand
RNeasy columns	Qiagen
RNeasy kit	Qiagen
SuperSignal West Pico Chemiluminescent Substrate	Thermo-Scientific
TSA® Plus Cyanine 3	Perkinelmer
ABC kit (DAB)	Vector Elite

Table 9.3 List of machines.

Instrument	Company
Biometra thermocycler TProfessional TRIO PCR	Biometra
BioPhotometer plus	Eppendorf
Chemidoc imaging system	Bio-Rad
Cryostar NX70	Thermo Fisher Scientific
Electrophoresis gel boxes	Bio-rad
EthoVision tracking system	Noldus
Housing cages	TECNIPLAST
Ultra-Turrax homogenizer	IKA
LSM 700 or upright LSM 700	Zeiss
Mechanical homogenizer for tissues	VWR
NanoDrop system	Thermo Scientific
Power Source TM 300V	Bio-rad
RotaRod system	TSE Systems
Step One Plus Real Time PCR System	Applied Biosystems
Tube rotator VWR	VWR
EPI-SCOPE1 Apotome	Zeiss

Table 9.4 List of software.

Software	Company
GraphPad Prism Software 7	GraphPad Software
ImageJ	US National Institutes of Health
ImageLab software	Bio-Rad
Imaris FilamentTracer	Bitplane
NeuronStudio	(Rodriguez et al., 2008; Wearne et al., 2005)

10. List of abbreviations

Abbreviation	Extended name
DAB	3,3'-Diaminobenzidine
AC	Adenylyl Cyclase
AD	Alzheimer's disease
AMPA	α-amino-3-hydroxy-5-methyl-4-isoxazolepropionic acid
ARVD2	Arrhythmogenic Right Ventricular Dysplasia type 2
et al.,	and others (“”et alii”)
ATP	Adenosine Triphosphate
AAV	Adeno Associated Virus
bAP	back propagating Action Potential
bp	Base Pair
BDNF	Brain-Derived Neurotropic Factor
BSA	Bovine Serum Albumin
CICR	Calcium-Induced Calcium Release
CAMKII	Calcium/Calmodulin-dependent Protein Kinase II
CPVT	Catecholaminergic Polymorphic Ventricular Tachycardia
CCD	Central Core Disease
CPP	Conditioned Place Preference
CFC	Contextual Fear Condition
Cre	Cyclization recombinant
Ct	Coefficient for temperature
DG	Dentate Gyrus
DIV	Days In Vitro
DNA	Deoxyribonucleic acid
EDTA	EthyleneDiamineTetraacetic Acid
EE	Enriched Enviroment
ER	Endoplasmic Reticulum
EC	Enthorinal Cortex
EtOH	Ethanol
FKBPs	FK506-binding protein
fl	floxed
fw	forward
gDNA	genomic DNA
GFP	Green Fluorescent Protein
HRP	Horseradish Peroxidase
i.p.	intra peritoneal
IHC	ImmunoHistoChemistry
iTL	ingenious Targeting Laboratory
GABA	γ-aminobutyric acid
IP_3R	Inositol Triphosphate Receptor
IP_3	Inositol Trisphosphate
KO	Knock Out

LTD	Long-Term Depression
LTM	Long-Term Memory
LTP	Long-Term Potentiation
MH	Malignant Hyperthermia
MSN	Medium Spiny Neurons
mGluRs	Metabotropic receptors
MCI	Mild Cognitive Impairment
MWM	Morris Water Maze
MF	Mossy Fibers
mRNA	messenger RNA
NAc	Nucleus Acumbens
nd	not detected
NMDA	N-methyl-D-aspartic acid
NGS	Normal Goat Serum
nt	nucleotide
ODN	Oligonucleotides
PFA	ParaformAldehyde
PBS	Phosphate-Buffered Saline
PCR	Polymerase Chain Reaction
PP	Perforant Path
pH	power of Hydrogen
PIP_2	PhosphatidylInositol 4,5-bisPhosphate
PLC	Phospholipase C
Ps	Presinilin
PSD	Post Synaptic Densities
PTSD	Post Traumatic Stress Disorder
PfCx	Prefrontal Cortex
PKA	Protein Kinase A
PKC	Protein Kinase C
qPCR	quantitative PCR
RNase	Ribonuclease
RT	Room Temperature
Rw	Reverse
RyR1	Ryanodine Receptor 1
RyR2	Ryanodine Receptor 2
RyR3	Ryanodine Receptor 3
RyRs	Ryanodine Receptors
S.	Stratum
scr	*scramble*
SDS	*Sodium Dodecyl Sulfate*
SEM	Standard Error Mean
sh	short hairpin
SC	Shaffer Collaterals
STM	Short Term Memory

sNTP	Nucleoside Triphosphate
Sb	Subiculum
SP	Synaptopodin
TEMED	Tetramethylethylenediamine
VGCCs	Voltage-Gated Calcium Channel
WT	Wild Type

11. References

Adasme, T., Haeger, P., Paula-Lima, A.C., Espinoza, I., Casas-Alarcon, M.M., Carrasco, M.A., and Hidalgo, C. (2011). Involvement of ryanodine receptors in neurotrophin-induced hippocampal synaptic plasticity and spatial memory formation. Proc Natl Acad Sci U S A *108*, 3029-3034.

Amaral, D.G., and Witter, M.P. (1989). The three-dimensional organization of the hippocampal formation: a review of anatomical data. Neuroscience *31*, 571-591.

Antonell, A., Llado, A., Altirriba, J., Botta-Orfila, T., Balasa, M., Fernandez, M., Ferrer, I., Sanchez-Valle, R., and Molinuevo, J.L. (2013). A preliminary study of the whole-genome expression profile of sporadic and monogenic early-onset Alzheimer's disease. Neurobiol Aging *34*, 1772-1778.

Arias-Cavieres, A., Barrientos, G.C., Sanchez, G., Elgueta, C., Munoz, P., and Hidalgo, C. (2018). Ryanodine Receptor-Mediated Calcium Release Has a Key Role in Hippocampal LTD Induction. Front Cell Neurosci *12*, 403.

Awasthi, A., Ramachandran, B., Ahmed, S., Benito, E., Shinoda, Y., Nitzan, N., Heukamp, A., Rannio, S., Martens, H., Barth, J., et al. (2019). Synaptotagmin-3 drives AMPA receptor endocytosis, depression of synapse strength, and forgetting. Science *363*.

Baker, K.D., Edwards, T.M., and Rickard, N.S. (2010). A ryanodine receptor agonist promotes the consolidation of long-term memory in young chicks. Behav Brain Res *206*, 143-146.

Baker, K.D., Edwards, T.M., and Rickard, N.S. (2013). The role of intracellular calcium stores in synaptic plasticity and memory consolidation. Neurosci Biobehav Rev *37*, 1211-1239.

Balschun, D., Wolfer, D.P., Bertocchini, F., Barone, V., Conti, A., Zuschratter, W., Missiaen, L., Lipp, H.P., Frey, J.U., and Sorrentino, V. (1999). Deletion of the ryanodine receptor type 3 (RyR3) impairs forms of synaptic plasticity and spatial learning. EMBO J *18*, 5264-5273.

Bays, P.M., Gorgoraptis, N., Wee, N., Marshall, L., and Husain, M. (2011). Temporal dynamics of encoding, storage, and reallocation of visual working memory. J Vis *11*.

Bekkers, J.M. (2011). Pyramidal neurons. Curr Biol *21*, R975.

Berridge, M.J., Bootman, M.D., and Roderick, H.L. (2003). Calcium signalling: dynamics, homeostasis and remodelling. Nat Rev Mol Cell Biol *4*, 517-529.

Berridge, M.J., Lipp, P., and Bootman, M.D. (2000). The versatility and universality of calcium signalling. Nat Rev Mol Cell Biol *1*, 11-21.

Berry, K.P., and Nedivi, E. (2017). Spine Dynamics: Are They All the Same? Neuron *96*, 43-55.

Bezaire, M.J., and Soltesz, I. (2013). Quantitative assessment of CA1 local circuits: knowledge base for interneuron-pyramidal cell connectivity. Hippocampus *23*, 751-785.

Bezprozvanny, I., Watras, J., and Ehrlich, B.E. (1991). Bell-shaped calcium-response curves of Ins(1,4,5)P3- and calcium-gated channels from endoplasmic reticulum of cerebellum. Nature *351*, 751-754.

Bird, C.M., and Burgess, N. (2008). The hippocampus and memory: insights from spatial processing. Nat Rev Neurosci *9*, 182-194.

Bliss, T.V., and Lomo, T. (1973). Long-lasting potentiation of synaptic transmission in the dentate area of the anaesthetized rabbit following stimulation of the perforant path. J Physiol *232*, 331-356.

Bourgeois, J.P., and Rakic, P. (1993). Changes of synaptic density in the primary visual cortex of the macaque monkey from fetal to adult stage. J Neurosci *13*, 2801-2820.

Breit, M., Kessler, M., Stepniewski, M., Vlachos, A., and Queisser, G. (2018). Spine-to-Dendrite Calcium Modeling Discloses Relevance for Precise Positioning of Ryanodine Receptor-Containing Spine Endoplasmic Reticulum. Sci Rep *8*, 15624.

Brillantes, A.B., Ondrias, K., Scott, A., Kobrinsky, E., Ondriasova, E., Moschella, M.C., Jayaraman, T., Landers, M., Ehrlich, B.E., and Marks, A.R. (1994). Stabilization of calcium release channel (ryanodine receptor) function by FK506-binding protein. Cell *77*, 513-523.

Brown, R.W., and Kolb, B. (2001). Nicotine sensitization increases dendritic length and spine density in the nucleus accumbens and cingulate cortex. Brain Res *899*, 94-100.

Bruno, A.M., Huang, J.Y., Bennett, D.A., Marr, R.A., Hastings, M.L., and Stutzmann, G.E. (2012). Altered ryanodine receptor expression in mild cognitive impairment and Alzheimer's disease. Neurobiol Aging *33*, 1001 e1001-1006.

Carafoli, E. (2004). Calcium-mediated cellular signals: a story of failures. Trends Biochem Sci *29*, 371-379.

Chicurel, M.E., and Harris, K.M. (1992). Three-dimensional analysis of the structure and composition of CA3 branched dendritic spines and their synaptic relationships with mossy fiber boutons in the rat hippocampus. J Comp Neurol *325*, 169-182.

Chua, J.J., Kindler, S., Boyken, J., and Jahn, R. (2010). The architecture of an excitatory synapse. J Cell Sci *123*, 819-823.

Citri, A., and Malenka, R.C. (2008). Synaptic plasticity: multiple forms, functions, and mechanisms. Neuropsychopharmacology *33*, 18-41.

Clapham, D.E. (2007). Calcium signaling. Cell *131*, 1047-1058.

Colgan, L.A., and Yasuda, R. (2014). Plasticity of dendritic spines: subcompartmentalization of signaling. Annu Rev Physiol *76*, 365-385.

Coronado, R., Morrissette, J., Sukhareva, M., and Vaughan, D.M. (1994). Structure and function of ryanodine receptors. Am J Physiol *266*, C1485-1504.

De Crescenzo, V., Fogarty, K.E., Lefkowitz, J.J., Bellve, K.D., Zvaritch, E., MacLennan, D.H., and Walsh, J.V., Jr. (2012). Type 1 ryanodine receptor knock-in mutation causing central core disease of skeletal muscle also displays a neuronal phenotype. Proc Natl Acad Sci U S A *109*, 610-615.

Deisseroth, K., Bito, H., and Tsien, R.W. (1996). Signaling from synapse to nucleus: postsynaptic CREB phosphorylation during multiple forms of hippocampal synaptic plasticity. Neuron *16*, 89-101.

Del Prete, D., Checler, F., and Chami, M. (2014). Ryanodine receptors: physiological function and deregulation in Alzheimer disease. Mol Neurodegener *9*, 21.

Dhikav, V., and Anand, K. (2011). Potential predictors of hippocampal atrophy in Alzheimer's disease. Drugs Aging *28*, 1-11.

Dinamarca, M.C., Guzzetti, F., Karpova, A., Lim, D., Mitro, N., Musardo, S., Mellone, M., Marcello, E., Stanic, J., Samaddar, T., et al. (2016). Ring finger protein 10 is a novel synaptonuclear messenger encoding activation of NMDA receptors in hippocampus. Elife *5*, e12430.

Duan, H., Wearne, S.L., Rocher, A.B., Macedo, A., Morrison, J.H., and Hof, P.R. (2003). Age-related dendritic and spine changes in corticocortically projecting neurons in macaque monkeys. Cereb Cortex *13*, 950-961.

Dumitriu, D., Hao, J., Hara, Y., Kaufmann, J., Janssen, W.G., Lou, W., Rapp, P.R., and Morrison, J.H. (2010). Selective changes in thin spine density and morphology in monkey prefrontal cortex correlate with aging-related cognitive impairment. J Neurosci *30*, 7507-7515.

Edwards, T.M., and Rickard, N.S. (2006). Pharmaco-behavioural evidence indicating a complex role for ryanodine receptor calcium release channels in memory processing for a passive avoidance task. Neurobiol Learn Mem *86*, 1-8.

Eichenbaum, H. (2001). The hippocampus and declarative memory: cognitive mechanisms and neural codes. Behav Brain Res *127*, 199-207.

Emptage, N., Bliss, T.V., and Fine, A. (1999). Single synaptic events evoke NMDA receptor-mediated release of calcium from internal stores in hippocampal dendritic spines. Neuron *22*, 115-124.

Engert, F., and Bonhoeffer, T. (1999). Dendritic spine changes associated with hippocampal long-term synaptic plasticity. Nature *399*, 66-70.

Fuhrmann, F., Justus, D., Sosulina, L., Kaneko, H., Beutel, T., Friedrichs, D., Schoch, S., Schwarz, M.K., Fuhrmann, M., and Remy, S. (2015). Locomotion, Theta Oscillations, and the Speed-Correlated Firing of Hippocampal Neurons Are Controlled by a Medial Septal Glutamatergic Circuit. Neuron *86*, 1253-1264.

Futatsugi, A., Kato, K., Ogura, H., Li, S.T., Nagata, E., Kuwajima, G., Tanaka, K., Itohara, S., and Mikoshiba, K. (1999). Facilitation of NMDAR-independent LTP and spatial learning in mutant mice lacking ryanodine receptor type 3. Neuron *24*, 701-713.

Galeotti, N., Quattrone, A., Vivoli, E., Norcini, M., Bartolini, A., and Ghelardini, C. (2008). Different involvement of type 1, 2, and 3 ryanodine receptors in memory processes. Learn Mem *15*, 315-323.

Gallagher, M., Landfield, P.W., McEwen, B., Meaney, M.J., Rapp, P.R., Sapolsky, R., and West, M.J. (1996). Hippocampal neurodegeneration in aging. Science *274*, 484-485.

Gartz Hanson, M., and Niswander, L.A. (2015). Rectification of muscle and nerve deficits in paralyzed ryanodine receptor type 1 mutant embryos. Dev Biol *404*, 76-87.

Gauthier, J.L., and Tank, D.W. (2018). A Dedicated Population for Reward Coding in the Hippocampus. Neuron *99*, 179-193 e177.

Giannini, G., Conti, A., Mammarella, S., Scrobogna, M., and Sorrentino, V. (1995). The ryanodine receptor/calcium channel genes are widely and differentially expressed in murine brain and peripheral tissues. J Cell Biol *128*, 893-904.

Giusti, S.A., Vercelli, C.A., Vogl, A.M., Kolarz, A.W., Pino, N.S., Deussing, J.M., and Refojo, D. (2014). Behavioral phenotyping of Nestin-Cre mice: implications for genetic mouse models of psychiatric disorders. J Psychiatr Res *55*, 87-95.

Grigoryan, G., Korkotian, E., and Segal, M. (2012). Selective facilitation of LTP in the ventral hippocampus by calcium stores. Hippocampus *22*, 1635-1644.

Grigoryan, G., and Segal, M. (2016). Ryanodine-mediated conversion of STP to LTP is lacking in synaptopodin-deficient mice. Brain Struct Funct *221*, 2393-2397.

Grutzendler, J., Kasthuri, N., and Gan, W.B. (2002). Long-term dendritic spine stability in the adult cortex. Nature *420*, 812-816.

Gu, L., Kleiber, S., Schmid, L., Nebeling, F., Chamoun, M., Steffen, J., Wagner, J., and Fuhrmann, M. (2014). Long-term in vivo imaging of dendritic spines in the hippocampus reveals structural plasticity. J Neurosci *34*, 13948-13953.

Hakamata, Y., Nakai, J., Takeshima, H., and Imoto, K. (1992). Primary structure and distribution of a novel ryanodine receptor/calcium release channel from rabbit brain. FEBS Lett *312*, 229-235.

Halliday, G. (2017). Pathology and hippocampal atrophy in Alzheimer's disease. Lancet Neurol *16*, 862-864.

Harris, K.M., Jensen, F.E., and Tsao, B. (1992). Three-dimensional structure of dendritic spines and synapses in rat hippocampus (CA1) at postnatal day 15 and adult ages: implications for the maturation of synaptic physiology and long-term potentiation. J Neurosci *12*, 2685-2705.

Harris, K.M., and Kater, S.B. (1994). Dendritic spines: cellular specializations imparting both stability and flexibility to synaptic function. Annu Rev Neurosci *17*, 341-371.

Harris, K.M., and Stevens, J.K. (1989). Dendritic spines of CA 1 pyramidal cells in the rat hippocampus: serial electron microscopy with reference to their biophysical characteristics. J Neurosci *9*, 2982-2997.

Harvey, J., and Collingridge, G.L. (1992). Thapsigargin blocks the induction of long-term potentiation in rat hippocampal slices. Neurosci Lett *139*, 197-200.

Hebb, D.O. (1949). The organization of behavior; a neuropsychological theory. (New York,: Wiley).

Heckers, S. (2001). Neuroimaging studies of the hippocampus in schizophrenia. Hippocampus *11*, 520-528.

Hiess, F., Detampel, P., Nolla-Colomer, C., Vallmitjana, A., Ganguly, A., Amrein, M., Ter Keurs, H., Benitez, R., Hove-Madsen, L., and Chen, S.R.W. (2018). Dynamic and Irregular Distribution of RyR2 Clusters in the Periphery of Live Ventricular Myocytes. Biophys J *114*, 343-354.

Hiess, F., Vallmitjana, A., Wang, R., Cheng, H., ter Keurs, H.E., Chen, J., Hove-Madsen, L., Benitez, R., and Chen, S.R. (2015). Distribution and Function of Cardiac Ryanodine Receptor Clusters in Live Ventricular Myocytes. J Biol Chem *290*, 20477-20487.

Ho, V.M., Lee, J.A., and Martin, K.C. (2011). The cell biology of synaptic plasticity. Science *334*, 623-628.

Hubener, M., and Bonhoeffer, T. (2010). Searching for engrams. Neuron *67*, 363-371.

Hunt, D.L., and Castillo, P.E. (2012). Synaptic plasticity of NMDA receptors: mechanisms and functional implications. Curr Opin Neurobiol *22*, 496-508.

Jiang, D., Wang, R., Xiao, B., Kong, H., Hunt, D.J., Choi, P., Zhang, L., and Chen, S.R. (2005). Enhanced store overload-induced Ca2+ release and channel sensitivity to luminal

Ca2+ activation are common defects of RyR2 mutations linked to ventricular tachycardia and sudden death. Circ Res *97*, 1173-1181.

Johenning, F.W., Theis, A.K., Pannasch, U., Ruckl, M., Rudiger, S., and Schmitz, D. (2015). Ryanodine Receptor Activation Induces Long-Term Plasticity of Spine Calcium Dynamics. PLoS Biol *13*, e1002181.

Ka, M., Kook, Y.H., Liao, K., Buch, S., and Kim, W.Y. (2016). Transactivation of TrkB by Sigma-1 receptor mediates cocaine-induced changes in dendritic spine density and morphology in hippocampal and cortical neurons. Cell Death Dis *7*, e2414.

Kang, L., Tian, M.K., Bailey, C.D., and Lambe, E.K. (2015). Dendritic spine density of prefrontal layer 6 pyramidal neurons in relation to apical dendrite sculpting by nicotinic acetylcholine receptors. Front Cell Neurosci *9*, 398.

Kelliher, M., Fastbom, J., Cowburn, R.F., Bonkale, W., Ohm, T.G., Ravid, R., Sorrentino, V., and O'Neill, C. (1999). Alterations in the ryanodine receptor calcium release channel correlate with Alzheimer's disease neurofibrillary and beta-amyloid pathologies. Neuroscience *92*, 499-513.

Kihira, T., Utunomiya, H., and Kondo, T. (2005). Expression of FKBP12 and ryanodine receptors (RyRs) in the spinal cord of MND patients. Amyotroph Lateral Scler Other Motor Neuron Disord *6*, 94-99.

Korkotian, E., and Segal, M. (1999). Release of calcium from stores alters the morphology of dendritic spines in cultured hippocampal neurons. Proc Natl Acad Sci U S A *96*, 12068-12072.

Kouzu, Y., Moriya, T., Takeshima, H., Yoshioka, T., and Shibata, S. (2000). Mutant mice lacking ryanodine receptor type 3 exhibit deficits of contextual fear conditioning and activation of calcium/calmodulin-dependent protein kinase II in the hippocampus. Brain Res Mol Brain Res *76*, 142-150.

Kovalchuk, Y., Eilers, J., Lisman, J., and Konnerth, A. (2000). NMDA receptor-mediated subthreshold Ca(2+) signals in spines of hippocampal neurons. J Neurosci *20*, 1791-1799.

Kurokawa, K., Mizuno, K., Shibasaki, M., Kiyokage, E., Toida, K., and Ohkuma, S. (2011). Cocaine increases ryanodine receptors via dopamine D1 receptors. Synapse *65*, 1106-1112.

Kurokawa, K., Mizuno, K., Shibasaki, M., and Ohkuma, S. (2010). Regulation of ryanodine receptors by dopamine D1 receptors during methamphetamine-induced place conditioning. J Neurochem *115*, 1206-1214.

Kwon, H.B., and Sabatini, B.L. (2011). Glutamate induces de novo growth of functional spines in developing cortex. Nature *474*, 100-104.

Lacampagne, A., Liu, X., Reiken, S., Bussiere, R., Meli, A.C., Lauritzen, I., Teich, A.F., Zalk, R., Saint, N., Arancio, O., et al. (2017). Post-translational remodeling of ryanodine receptor induces calcium leak leading to Alzheimer's disease-like pathologies and cognitive deficits. Acta Neuropathol *134*, 749-767.

Lanner, J.T., Georgiou, D.K., Joshi, A.D., and Hamilton, S.L. (2010). Ryanodine receptors: structure, expression, molecular details, and function in calcium release. Cold Spring Harb Perspect Biol *2*, a003996.

Ledda, F., and Paratcha, G. (2017). Mechanisms regulating dendritic arbor patterning. Cell Mol Life Sci *74*, 4511-4537.

Lee, K.F., Soares, C., Thivierge, J.P., and Beique, J.C. (2016). Correlated Synaptic Inputs Drive Dendritic Calcium Amplification and Cooperative Plasticity during Clustered Synapse Development. Neuron *89*, 784-799.

LeGates, T.A., Kvarta, M.D., Tooley, J.R., Francis, T.C., Lobo, M.K., Creed, M.C., and Thompson, S.M. (2018). Reward behaviour is regulated by the strength of hippocampus-nucleus accumbens synapses. Nature *564*, 258-262.

Lehnart, S.E., Mongillo, M., Bellinger, A., Lindegger, N., Chen, B.X., Hsueh, W., Reiken, S., Wronska, A., Drew, L.J., Ward, C.W., et al. (2008). Leaky Ca2+ release channel/ryanodine receptor 2 causes seizures and sudden cardiac death in mice. J Clin Invest *118*, 2230-2245.

Lerdkrai, C., Asavapanumas, N., Brawek, B., Kovalchuk, Y., Mojtahedi, N., Olmedillas Del Moral, M., and Garaschuk, O. (2018). Intracellular Ca(2+) stores control in vivo neuronal hyperactivity in a mouse model of Alzheimer's disease. Proc Natl Acad Sci U S A *115*, E1279-E1288.

Leybaert, L., and Sanderson, M.J. (2012). Intercellular Ca(2+) waves: mechanisms and function. Physiol Rev *92*, 1359-1392.

Liao, B., Zhang, Y., Sun, H., Ma, B., and Qian, J. (2016). Ryanodine Receptor 2 Plays a Critical Role in Spinal Cord Injury via Induction of Oxidative Stress. Cell Physiol Biochem *38*, 1129-1137.

Lippi, G., Steinert, J.R., Marczylo, E.L., D'Oro, S., Fiore, R., Forsythe, I.D., Schratt, G., Zoli, M., Nicotera, P., and Young, K.W. (2011). Targeting of the Arpc3 actin nucleation factor by miR-29a/b regulates dendritic spine morphology. J Cell Biol *194*, 889-904.

Liu, J., Supnet, C., Sun, S., Zhang, H., Good, L., Popugaeva, E., and Bezprozvanny, I. (2014). The role of ryanodine receptor type 3 in a mouse model of Alzheimer disease. Channels (Austin) *8*, 230-242.

Liu, Q., Chen, B., Yankova, M., Morest, D.K., Maryon, E., Hand, A.R., Nonet, M.L., and Wang, Z.W. (2005). Presynaptic ryanodine receptors are required for normal quantal size at the Caenorhabditis elegans neuromuscular junction. J Neurosci *25*, 6745-6754.

Liu, X., Betzenhauser, M.J., Reiken, S., Meli, A.C., Xie, W., Chen, B.X., Arancio, O., and Marks, A.R. (2012). Role of leaky neuronal ryanodine receptors in stress-induced cognitive dysfunction. Cell *150*, 1055-1067.

Livak, K.J., and Schmittgen, T.D. (2001). Analysis of relative gene expression data using real-time quantitative PCR and the 2(-Delta Delta C(T)) Method. Methods *25*, 402-408.

Lo, Y.J., and Poo, M.M. (1991). Activity-dependent synaptic competition in vitro: heterosynaptic suppression of developing synapses. Science *254*, 1019-1022.

Luscher, C., and Malenka, R.C. (2012). NMDA receptor-dependent long-term potentiation and long-term depression (LTP/LTD). Cold Spring Harb Perspect Biol *4*.

MacLennan, D.H., Duff, C., Zorzato, F., Fujii, J., Phillips, M., Korneluk, R.G., Frodis, W., Britt, B.A., and Worton, R.G. (1990). Ryanodine receptor gene is a candidate for predisposition to malignant hyperthermia. Nature *343*, 559-561.

Maguire, E.A., Gadian, D.G., Johnsrude, I.S., Good, C.D., Ashburner, J., Frackowiak, R.S., and Frith, C.D. (2000). Navigation-related structural change in the hippocampi of taxi drivers. Proc Natl Acad Sci U S A *97*, 4398-4403.

Malenka, R.C., Kauer, J.A., Perkel, D.J., Mauk, M.D., Kelly, P.T., Nicoll, R.A., and Waxham, M.N. (1989). An essential role for postsynaptic calmodulin and protein kinase activity in long-term potentiation. Nature *340*, 554-557.

Martin, E.D., and Buno, W. (2003). Caffeine-mediated presynaptic long-term potentiation in hippocampal CA1 pyramidal neurons. J Neurophysiol *89*, 3029-3038.

Martin, S.J., Grimwood, P.D., and Morris, R.G. (2000). Synaptic plasticity and memory: an evaluation of the hypothesis. Annu Rev Neurosci *23*, 649-711.

Marx, S.O., Reiken, S., Hisamatsu, Y., Jayaraman, T., Burkhoff, D., Rosemblit, N., and Marks, A.R. (2000). PKA phosphorylation dissociates FKBP12.6 from the calcium release channel (ryanodine receptor): defective regulation in failing hearts. Cell *101*, 365-376.

Matsuo, N., Tanda, K., Nakanishi, K., Yamasaki, N., Toyama, K., Takao, K., Takeshima, H., and Miyakawa, T. (2009). Comprehensive behavioral phenotyping of ryanodine receptor type 3 (RyR3) knockout mice: decreased social contact duration in two social interaction tests. Front Behav Neurosci *3*, 3.

Matsuzaki, M., Honkura, N., Ellis-Davies, G.C., and Kasai, H. (2004). Structural basis of long-term potentiation in single dendritic spines. Nature *429*, 761-766.

Mayer, M.L., Westbrook, G.L., and Guthrie, P.B. (1984). Voltage-dependent block by Mg2+ of NMDA responses in spinal cord neurones. Nature *309*, 261-263.

Medeiros-Domingo, A., Bhuiyan, Z.A., Tester, D.J., Hofman, N., Bikker, H., van Tintelen, J.P., Mannens, M.M., Wilde, A.A., and Ackerman, M.J. (2009). The RYR2-encoded

ryanodine receptor/calcium release channel in patients diagnosed previously with either catecholaminergic polymorphic ventricular tachycardia or genotype negative, exercise-induced long QT syndrome: a comprehensive open reading frame mutational analysis. J Am Coll Cardiol *54*, 2065-2074.

Meissner, G. (2017). The structural basis of ryanodine receptor ion channel function. J Gen Physiol *149*, 1065-1089.

More, J.Y., Bruna, B.A., Lobos, P.E., Galaz, J.L., Figueroa, P.L., Namias, S., Sanchez, G.L., Barrientos, G.C., Valdes, J.L., Paula-Lima, A.C., et al. (2018). Calcium Release Mediated by Redox-Sensitive RyR2 Channels Has a Central Role in Hippocampal Structural Plasticity and Spatial Memory. Antioxid Redox Signal *29*, 1125-1146.

Mori, F., Fukaya, M., Abe, H., Wakabayashi, K., and Watanabe, M. (2000). Developmental changes in expression of the three ryanodine receptor mRNAs in the mouse brain. Neurosci Lett *285*, 57-60.

Morris, R.G., and Frey, U. (1997). Hippocampal synaptic plasticity: role in spatial learning or the automatic recording of attended experience? Philos Trans R Soc Lond B Biol Sci *352*, 1489-1503.

Moser, M.B., Trommald, M., and Andersen, P. (1994). An increase in dendritic spine density on hippocampal CA1 pyramidal cells following spatial learning in adult rats suggests the formation of new synapses. Proc Natl Acad Sci U S A *91*, 12673-12675.

Moser, M.B., Trommald, M., Egeland, T., and Andersen, P. (1997). Spatial training in a complex environment and isolation alter the spine distribution differently in rat CA1 pyramidal cells. J Comp Neurol *380*, 373-381.

Nakai, J., Imagawa, T., Hakamat, Y., Shigekawa, M., Takeshima, H., and Numa, S. (1990). Primary structure and functional expression from cDNA of the cardiac ryanodine receptor/calcium release channel. FEBS Lett *271*, 169-177.

Nakamura, T., Barbara, J.G., Nakamura, K., and Ross, W.N. (1999). Synergistic release of Ca2+ from IP3-sensitive stores evoked by synaptic activation of mGluRs paired with backpropagating action potentials. Neuron *24*, 727-737.

Nelson, S.B., Hempel, C., and Sugino, K. (2006). Probing the transcriptome of neuronal cell types. Curr Opin Neurobiol *16*, 571-576.

Neves, G., Cooke, S.F., and Bliss, T.V. (2008). Synaptic plasticity, memory and the hippocampus: a neural network approach to causality. Nat Rev Neurosci *9*, 65-75.

Noguchi, J., Nagaoka, A., Watanabe, S., Ellis-Davies, G.C., Kitamura, K., Kano, M., Matsuzaki, M., and Kasai, H. (2011). In vivo two-photon uncaging of glutamate revealing the structure-function relationships of dendritic spines in the neocortex of adult mice. J Physiol *589*, 2447-2457.

Nusser, Z., Lujan, R., Laube, G., Roberts, J.D., Molnar, E., and Somogyi, P. (1998). Cell type and pathway dependence of synaptic AMPA receptor number and variability in the hippocampus. Neuron *21*, 545-559.

O'Keefe, J. (1976). Place units in the hippocampus of the freely moving rat. Exp Neurol *51*, 78-109.

O'Keefe, J., and Dostrovsky, J. (1971). The hippocampus as a spatial map. Preliminary evidence from unit activity in the freely-moving rat. Brain Res *34*, 171-175.

O'Keefe, J., and Speakman, A. (1987). Single unit activity in the rat hippocampus during a spatial memory task. Exp Brain Res *68*, 1-27.

Obenaus, A., Mody, I., and Baimbridge, K.G. (1989). Dantrolene-Na (Dantrium) blocks induction of long-term potentiation in hippocampal slices. Neurosci Lett *98*, 172-178.

Oh, M.C., and Derkach, V.A. (2005). Dominant role of the GluR2 subunit in regulation of AMPA receptors by CaMKII. Nat Neurosci *8*, 853-854.

Oh, M.C., Derkach, V.A., Guire, E.S., and Soderling, T.R. (2006). Extrasynaptic membrane trafficking regulated by GluR1 serine 845 phosphorylation primes AMPA receptors for long-term potentiation. J Biol Chem *281*, 752-758.

Oh, W.C., Parajuli, L.K., and Zito, K. (2015). Heterosynaptic structural plasticity on local dendritic segments of hippocampal CA1 neurons. Cell Rep *10*, 162-169.

Ohashi, R., Sakata, S., Naito, A., Hirashima, N., and Tanaka, M. (2014). Dendritic differentiation of cerebellar Purkinje cells is promoted by ryanodine receptors expressed by Purkinje and granule cells. Dev Neurobiol *74*, 467-480.

Otmakhov, N., Khibnik, L., Otmakhova, N., Carpenter, S., Riahi, S., Asrican, B., and Lisman, J. (2004). Forskolin-induced LTP in the CA1 hippocampal region is NMDA receptor dependent. J Neurophysiol *91*, 1955-1962.

Oules, B., Del Prete, D., Greco, B., Zhang, X., Lauritzen, I., Sevalle, J., Moreno, S., Paterlini-Brechot, P., Trebak, M., Checler, F., et al. (2012). Ryanodine receptor blockade reduces amyloid-beta load and memory impairments in Tg2576 mouse model of Alzheimer disease. J Neurosci *32*, 11820-11834.

Ozcan, A.S. (2017). Filopodia: A Rapid Structural Plasticity Substrate for Fast Learning. Front Synaptic Neurosci *9*, 12.

Park, J.Y., and Spruston, N. (2012). Synergistic actions of metabotropic acetylcholine and glutamate receptors on the excitability of hippocampal CA1 pyramidal neurons. J Neurosci *32*, 6081-6091.

Pelisch, N., Gomes, C., Nally, J.M., Petruska, J.C., and Stirling, D.P. (2017). Differential expression of ryanodine receptor isoforms after spinal cord injury. Neurosci Lett *660*, 51-56.

Peng, W., Shen, H., Wu, J., Guo, W., Pan, X., Wang, R., Chen, S.R., and Yan, N. (2016). Structural basis for the gating mechanism of the type 2 ryanodine receptor RyR2. Science *354*.

Pfeiffer, T., Poll, S., Bancelin, S., Angibaud, J., Inavalli, V.K., Keppler, K., Mittag, M., Fuhrmann, M., and Nagerl, U.V. (2018). Chronic 2P-STED imaging reveals high turnover of dendritic spines in the hippocampus in vivo. Elife *7*.

Phillips, R.G., and LeDoux, J.E. (1994). Lesions of the dorsal hippocampal formation interfere with background but not foreground contextual fear conditioning. Learn Mem *1*, 34-44.

Porter Moore, C., Zhang, J.Z., and Hamilton, S.L. (1999). A role for cysteine 3635 of RYR1 in redox modulation and calmodulin binding. J Biol Chem *274*, 36831-36834.

Pouille, F., and Scanziani, M. (2001). Enforcement of temporal fidelity in pyramidal cells by somatic feed-forward inhibition. Science *293*, 1159-1163.

Pozo, K., and Goda, Y. (2010). Unraveling mechanisms of homeostatic synaptic plasticity. Neuron *66*, 337-351.

Pritchard, H.A.T., Pires, P.W., Yamasaki, E., Thakore, P., and Earley, S. (2018). Nanoscale remodeling of ryanodine receptor cluster size underlies cerebral microvascular dysfunction in Duchenne muscular dystrophy. Proc Natl Acad Sci U S A *115*, E9745-E9752.

Rizzuto, R., and Pozzan, T. (2006). Microdomains of intracellular Ca2+: molecular determinants and functional consequences. Physiol Rev *86*, 369-408.

Rochefort, N.L., and Konnerth, A. (2012). Dendritic spines: from structure to in vivo function. EMBO Rep *13*, 699-708.

Rodriguez, A., Ehlenberger, D.B., Dickstein, D.L., Hof, P.R., and Wearne, S.L. (2008). Automated three-dimensional detection and shape classification of dendritic spines from fluorescence microscopy images. PLoS One *3*, e1997.

Rusakov, D.A., Davies, H.A., Harrison, E., Diana, G., Richter-Levin, G., Bliss, T.V., and Stewart, M.G. (1997). Ultrastructural synaptic correlates of spatial learning in rat hippocampus. Neuroscience *80*, 69-77.

Sabatini, B.L., Oertner, T.G., and Svoboda, K. (2002). The life cycle of Ca(2+) ions in dendritic spines. Neuron *33*, 439-452.

Sando, R., Bushong, E., Zhu, Y., Huang, M., Considine, C., Phan, S., Ju, S., Uytiepo, M., Ellisman, M., and Maximov, A. (2017). Assembly of Excitatory Synapses in the Absence of Glutamatergic Neurotransmission. Neuron *94*, 312-321 e313.

Santulli, G., Lewis, D., des Georges, A., Marks, A.R., and Frank, J. (2018). Ryanodine Receptor Structure and Function in Health and Disease. Subcell Biochem *87*, 329-352.

Scheff, S.W., and Price, D.A. (1998). Synaptic density in the inner molecular layer of the hippocampal dentate gyrus in Alzheimer disease. J Neuropathol Exp Neurol *57*, 1146-1153.

Scoville, W.B., and Milner, B. (1957). Loss of recent memory after bilateral hippocampal lesions. J Neurol Neurosurg Psychiatry *20*, 11-21.

Segal, M., and Korkotian, E. (2014). Endoplasmic reticulum calcium stores in dendritic spines. Front Neuroanat *8*, 64.

Sharp, A.H., McPherson, P.S., Dawson, T.M., Aoki, C., Campbell, K.P., and Snyder, S.H. (1993). Differential immunohistochemical localization of inositol 1,4,5-trisphosphate- and ryanodine-sensitive Ca2+ release channels in rat brain. J Neurosci *13*, 3051-3063.

Sheng, M., and Hoogenraad, C.C. (2007). The postsynaptic architecture of excitatory synapses: a more quantitative view. Annu Rev Biochem *76*, 823-847.

Shimizu, H., Fukaya, M., Yamasaki, M., Watanabe, M., Manabe, T., and Kamiya, H. (2008). Use-dependent amplification of presynaptic Ca2+ signaling by axonal ryanodine receptors at the hippocampal mossy fiber synapse. Proc Natl Acad Sci U S A *105*, 11998-12003.

Shimuta, M., Yoshikawa, M., Fukaya, M., Watanabe, M., Takeshima, H., and Manabe, T. (2001). Postsynaptic modulation of AMPA receptor-mediated synaptic responses and LTP by the type 3 ryanodine receptor. Mol Cell Neurosci *17*, 921-930.

Shin, L.M., Shin, P.S., Heckers, S., Krangel, T.S., Macklin, M.L., Orr, S.P., Lasko, N., Segal, E., Makris, N., Richert, K., et al. (2004). Hippocampal function in posttraumatic stress disorder. Hippocampus *14*, 292-300.

Shrager, Y., Bayley, P.J., Bontempi, B., Hopkins, R.O., and Squire, L.R. (2007). Spatial memory and the human hippocampus. Proc Natl Acad Sci U S A *104*, 2961-2966.

Sigler, A., Oh, W.C., Imig, C., Altas, B., Kawabe, H., Cooper, B.H., Kwon, H.B., Rhee, J.S., and Brose, N. (2017). Formation and Maintenance of Functional Spines in the Absence of Presynaptic Glutamate Release. Neuron *94*, 304-311 e304.

Siskova, Z., Justus, D., Kaneko, H., Friedrichs, D., Henneberg, N., Beutel, T., Pitsch, J., Schoch, S., Becker, A., von der Kammer, H., et al. (2014). Dendritic structural degeneration is functionally linked to cellular hyperexcitability in a mouse model of Alzheimer's disease. Neuron *84*, 1023-1033.

Smith, J.S., Coronado, R., and Meissner, G. (1986). Single channel measurements of the calcium release channel from skeletal muscle sarcoplasmic reticulum. Activation by Ca2+ and ATP and modulation by Mg2+. J Gen Physiol *88*, 573-588.

Soltesz, I., and Losonczy, A. (2018). CA1 pyramidal cell diversity enabling parallel information processing in the hippocampus. Nat Neurosci *21*, 484-493.

Spacek, J., and Harris, K.M. (1997). Three-dimensional organization of smooth endoplasmic reticulum in hippocampal CA1 dendrites and dendritic spines of the immature and mature rat. J Neurosci *17*, 190-203.

Spruston, N. (2008). Pyramidal neurons: dendritic structure and synaptic integration. Nat Rev Neurosci *9*, 206-221.

Strange, B., and Dolan, R. (1999). Functional segregation within the human hippocampus. Mol Psychiatry *4*, 508-511.

Strange, B.A., Witter, M.P., Lein, E.S., and Moser, E.I. (2014). Functional organization of the hippocampal longitudinal axis. Nat Rev Neurosci *15*, 655-669.

Sudhof, T.C., and Malenka, R.C. (2008). Understanding synapses: past, present, and future. Neuron *60*, 469-476.

Sukhareva, M., Smith, S.V., Maric, D., and Barker, J.L. (2002). Functional properties of ryanodine receptors in hippocampal neurons change during early differentiation in culture. J Neurophysiol *88*, 1077-1087.

Takasago, T., Imagawa, T., Furukawa, K., Ogurusu, T., and Shigekawa, M. (1991). Regulation of the cardiac ryanodine receptor by protein kinase-dependent phosphorylation. J Biochem *109*, 163-170.

Takeshima, H., Iino, M., Takekura, H., Nishi, M., Kuno, J., Minowa, O., Takano, H., and Noda, T. (1994). Excitation-contraction uncoupling and muscular degeneration in mice lacking functional skeletal muscle ryanodine-receptor gene. Nature *369*, 556-559.

Takeshima, H., Ikemoto, T., Nishi, M., Nishiyama, N., Shimuta, M., Sugitani, Y., Kuno, J., Saito, I., Saito, H., Endo, M., et al. (1996). Generation and characterization of mutant mice lacking ryanodine receptor type 3. J Biol Chem *271*, 19649-19652.

Takeshima, H., Komazaki, S., Hirose, K., Nishi, M., Noda, T., and Iino, M. (1998). Embryonic lethality and abnormal cardiac myocytes in mice lacking ryanodine receptor type 2. EMBO J *17*, 3309-3316.

Takeshima, H., Nishimura, S., Matsumoto, T., Ishida, H., Kangawa, K., Minamino, N., Matsuo, H., Ueda, M., Hanaoka, M., Hirose, T., et al. (1989). Primary structure and expression from complementary DNA of skeletal muscle ryanodine receptor. Nature *339*, 439-445.

Tang, Y.P., Shimizu, E., Dube, G.R., Rampon, C., Kerchner, G.A., Zhuo, M., Liu, G., and Tsien, J.Z. (1999). Genetic enhancement of learning and memory in mice. Nature *401*, 63-69.

Torres, R.F., Hidalgo, C., and Kerr, B. (2017). Mecp2 Mediates Experience-Dependent Transcriptional Upregulation of Ryanodine Receptor Type-3. Front Mol Neurosci *10*, 188.

Trommald, M., and Hulleberg, G. (1997). Dimensions and density of dendritic spines from rat dentate granule cells based on reconstructions from serial electron micrographs. J Comp Neurol *377*, 15-28.

Tronche, F., Kellendonk, C., Kretz, O., Gass, P., Anlag, K., Orban, P.C., Bock, R., Klein, R., and Schutz, G. (1999). Disruption of the glucocorticoid receptor gene in the nervous system results in reduced anxiety. Nat Genet *23*, 99-103.

Tsien, J.Z., Chen, D.F., Gerber, D., Tom, C., Mercer, E.H., Anderson, D.J., Mayford, M., Kandel, E.R., and Tonegawa, S. (1996). Subregion- and cell type-restricted gene knockout in mouse brain. Cell *87*, 1317-1326.

Van Petegem, F. (2012). Ryanodine receptors: structure and function. J Biol Chem *287*, 31624-31632.

Van Petegem, F. (2015). Ryanodine receptors: allosteric ion channel giants. J Mol Biol *427*, 31-53.

Vlachos, A., Korkotian, E., Schonfeld, E., Copanaki, E., Deller, T., and Segal, M. (2009). Synaptopodin regulates plasticity of dendritic spines in hippocampal neurons. J Neurosci *29*, 1017-1033.

Walker, M.A., Kohl, T., Lehnart, S.E., Greenstein, J.L., Lederer, W.J., and Winslow, R.L. (2015). On the Adjacency Matrix of RyR2 Cluster Structures. PLoS Comput Biol *11*, e1004521.

Wan, K., Moriya, T., Akiyama, M., Takeshima, H., and Shibata, S. (1999). Involvement of ryanodine receptor type 3 in dopamine release from the striatum: evidence from mutant mice lacking this receptor. Biochem Biophys Res Commun *266*, 588-592.

Wang, J., and Best, P.M. (1992). Inactivation of the sarcoplasmic reticulum calcium channel by protein kinase. Nature *359*, 739-741.

Wearne, S.L., Rodriguez, A., Ehlenberger, D.B., Rocher, A.B., Henderson, S.C., and Hof, P.R. (2005). New techniques for imaging, digitization and analysis of three-dimensional neural morphology on multiple scales. Neuroscience *136*, 661-680.

Wehrens, X.H., Lehnart, S.E., Huang, F., Vest, J.A., Reiken, S.R., Mohler, P.J., Sun, J., Guatimosim, S., Song, L.S., Rosemblit, N., et al. (2003). FKBP12.6 deficiency and defective calcium release channel (ryanodine receptor) function linked to exercise-induced sudden cardiac death. Cell *113*, 829-840.

Welsby, P., Rowan, M., and Anwyl, R. (2006). Nicotinic receptor-mediated enhancement of long-term potentiation involves activation of metabotropic glutamate receptors and ryanodine-sensitive calcium stores in the dentate gyrus. Eur J Neurosci *24*, 3109-3118.

White, N.M., and Carr, G.D. (1985). The conditioned place preference is affected by two independent reinforcement processes. Pharmacol Biochem Behav *23*, 37-42.

Witter, M.P., Griffioen, A.W., Jorritsma-Byham, B., and Krijnen, J.L. (1988). Entorhinal projections to the hippocampal CA1 region in the rat: an underestimated pathway. Neurosci Lett *85*, 193-198.

Wu, Y., Whiteus, C., Xu, C.S., Hayworth, K.J., Weinberg, R.J., Hess, H.F., and De Camilli, P. (2017). Contacts between the endoplasmic reticulum and other membranes in neurons. Proc Natl Acad Sci U S A *114*, E4859-E4867.

Yu, H.M., Wen, J., Wang, R., Shen, W.H., Duan, S., and Yang, H.T. (2008). Critical role of type 2 ryanodine receptor in mediating activity-dependent neurogenesis from embryonic stem cells. Cell Calcium *43*, 417-431.

Yuan, Q., Deng, K.Y., Sun, L., Chi, S., Yang, Z., Wang, J., Xin, H.B., Wang, X., and Ji, G. (2016). Calstabin 2: An important regulator for learning and memory in mice. Sci Rep *6*, 21087.

Yuste, R. (2015). The discovery of dendritic spines by Cajal. Front Neuroanat *9*, 18.

Zhang, Y., Chen, H.S., Khanna, V.K., De Leon, S., Phillips, M.S., Schappert, K., Britt, B.A., Browell, A.K., and MacLennan, D.H. (1993). A mutation in the human ryanodine receptor gene associated with central core disease. Nat Genet *5*, 46-50.

Zhao, W., Meiri, N., Xu, H., Cavallaro, S., Quattrone, A., Zhang, L., and Alkon, D.L. (2000). Spatial learning induced changes in expression of the ryanodine type II receptor in the rat hippocampus. FASEB J *14*, 290-300.

Zhou, H., Lillis, S., Loy, R.E., Ghassemi, F., Rose, M.R., Norwood, F., Mills, K., Al-Sarraj, S., Lane, R.J., Feng, L., et al. (2010). Multi-minicore disease and atypical periodic paralysis associated with novel mutations in the skeletal muscle ryanodine receptor (RYR1) gene. Neuromuscul Disord *20*, 166-173.

Zhu, Y., Romero, M.I., Ghosh, P., Ye, Z., Charnay, P., Rushing, E.J., Marth, J.D., and Parada, L.F. (2001). Ablation of NF1 function in neurons induces abnormal development of cerebral cortex and reactive gliosis in the brain. Genes Dev *15*, 859-876.

Ziviani, E., Lippi, G., Bano, D., Munarriz, E., Guiducci, S., Zoli, M., Young, K.W., and Nicotera, P. (2011). Ryanodine receptor-2 upregulation and nicotine-mediated plasticity. EMBO J *30*, 194-204.

12. Contributions

Mice housing, sacrifice, dissections and genotyping was performed with the help of animal caretakers, Dr. rer. nat. Lena Wischhof, Dr. rer. nat. Miriam Stork, Dr. vet. med. Dagmar Sonntag-Bensch and Christiane Bartling-Kirsch. Experiment in Figure 5.1 has been performed as a part of my SyDAD secondment in the group of Prof. Monica Di Luca, Prof. Fabrizio Gardoni and Dr. Elena Marcello (University of Milan). Experiment in Figure 5.2B has been performed by Dr. rer. nat. Alessandra Fornarelli from the group of Prof. Dr. Pierluigi Nicotera (DZNE). Experiments in Figure 5.3, Figure 5.6, Figure 5.7, Figure 5.8 has been performed in collaboration with Dr. rer. nat. Lena Wishhof from the group of Dr. Daniele Bano (DZNE). Experiments in Figure 5.5 has been performed in collaboration with Dr. rer. nat. Liudmila Sosulina and Dennis Dallügge from the group of Prof. Dr. Stefan Remy (DZNE).

13. Disclosure statement

Hereby, I declare that I prepared the thesis entitled “Ryanodine Receptor 2 (RyR2) underlies maintenance and remodeling of dendritic spines” independently, except where otherwise stated. All sources used have been explicitly quoted and help provided by other people has been stated.

Fabio Bertan

14. Acknowledgment

I am grateful to my supervisor Prof. Pierluigi Nicotera for giving me the opportunity to work at DZNE and for creating the circumstances for being productive and effective. A remark goes also to Dr. Daniele Bano who invested time, effort and faith in my work. Additionally, I thank Prof. Michael Pankratz for agreeing to supervise me, and Prof. Waldemar Kolanus and Prof. Dorothea Bartels for being part of my commission in the PhD examination. I also thank all the collaborators, in particular Prof. Remy, Prof. Fuhrmann, Prof. Di Luca, Prof. Gardoni and Dr. Marcello, who actively supported and helped me to finalize this project. Last but not least, I would like to praise the SyDAD* for the great experience to be part of an excellent Marie Skłodowska-Curie cluster.

Lab-wise, I am very thankful to Lena who actively contributed to the development of my personal expertise, knowledge and, not less, to our project. Moreover, I am indebted with Antonia for the critical comments and corrections on my thesis. My gratitude goes to Christiane, Dagmar and Miriam for all the lab support received over the years. Additionally, I am pleased to thank all the former and current members of the group for the extraordinary atmosphere in the laboratory. It was a tremendous experience to work with such dynamic, brilliant and alcoholic bunch of nerds. Here, my mates in alphabetic order: Anaïs, Antonia, Anna, Clemens, Drazen, Jonas, Joshua, Lena, Natasha, Malkolm and Simona. I have shared with you fantastic moments!

Uppermost, I thank my friends and my family, especially Giulia, for being part of my adventure and supporting me over these rich years of life.

* This project has received funding from the European Union's Horizon 2020 research and innovation programme under the Marie Skłodowska-Curie grant agreement No 676144 (Synaptic Dysfunction in Alzheimer Disease, SyDAD).